An *in vitro* model of oxidative damage in bovine cortical bone to induce bone fragility

by

Cyrus Jean-Baptiste Molavi Fiori

A thesis
presented to the University of Waterloo
in fulfillment of the
thesis requirement for the degree of
Master of Applied Science
in
Chemical Engineering

Waterloo, Ontario, Canada, 2021

Author's Declaration

I hereby declare that I am the sole author of this thesis. This is a true copy of the thesis, including any required final revisions, as accepted by my examiners.

I understand that my thesis may be made electronically available to the public.

Abstract

Increased bone fragility can stem from age-related and chronic bone affecting diseases (such as osteoporosis, diabetes and kidney disease), chemotherapeutic and radiation-based cancer treatments, and/or trauma and results in massive annual cost to the healthcare system and decreased quality of life for patients. In order to ameliorate these problems, an in-depth understanding of the cause of increased bone fragility is necessary. Oxidative stress, also known as inflammation, is hypothesized to be a key mechanism of causing oxidative damage in cortical bone's collagen phase, thereby increasing its fragility; however, this mechanism has not yet been confirmed. Operating under this hypothesis, the present work sought to 1) design an in vitro model of controlled and elevated physiologically-relevant oxidative damage using bovine cortical bone, 2) conduct pore network modelling of the transient reactive diffusion occurring within the bovine cortical bone's porous structure to inform operation of the *in vitro* model, and 3) validate the pore network model experimentally using results from the in vitro model.

A first-of-its-kind technique was developed to create controlled levels of oxidative damage in bovine cortical bone beams *in vitro* using free radicals generated from the decomposition of hydrogen peroxide (H_2O_2) using a Co^{2+} catalyst in aqueous solution. Pore network modelling (PNM) of this system indicated that the decomposition reaction proceeded extremely fast, which caused the greatest concentrations of H_2O_2 to exist at the specimens' surfaces and limited diffusion of H_2O_2 into the bone's porous network. This was also the first ever application of PNM to study reactive transient diffusion in bone and was valuable for informing the operation of the *in vitro* model. A novel fluorescent tissue staining technique for carbonyls, differing from current assay-based approaches, was developed to visualize the oxidative damage gradient within the bone beams, and images generated using this technique qualitatively validated the pore network model. No statistically significant differences or correlations were observed between different treatments or H_2O_2 concentrations and work to fracture, fracture toughness, maximum deflection, and mean pixel intensity. Statistical significance was not assessed for pixel intensity distributions (n = 1). This work provides important contributions to the study of oxidative stress and bone fragility in the form of a novel application of PNM to bone and new techniques for both causing and characterizing oxidative damage in tissues. These techniques may be applied to other biological materials and human tissues to address the paucity of much-needed foundational knowledge for the study of oxidative stress, damage, and tissue fragility in biological systems.

Acknowledgements

The author would like to thank Professors Thomas Willett and Raymond Legge for the opportunity to conduct this research at the University of Waterloo and for their bottomless support, encouragement, patience, and honesty during this time.

The author would also like to thank Professor Jeff Gostick for his immense help with porous media, transport phenomena, OpenPNM, and Python programming. Thanks goes to Professor Evelyn Yim for offering her time on the Oral Examination committee. Thanks also goes to Professor Maud Gorbet for assistance with fluorescence microscopy.

Special thanks must go to Corin Seelemann for his support and expertise in chevron notching, fracture testing, fluorescent imaging, and image analysis. The author also appreciated his incredible willingness to always help, field ideas, and transport samples to faraway regions.

The author would also like to thank Daniel Dapaah for his incredible insight into fracture mechanics, excellent sound-boarding, and extensive knowledge of the literature. Thanks also goes to Jindra Tupy for developing many of the biochemical protocols utilized in this work and answering the author's endless questions. The author would also like to thank Faezeh Iranmanesh for her help in the lab and the Waterloo Composite Biomaterial Systems Lab's members past and present for their help and support.

Thanks goes to Bert Habicher for his limitless knowledge of building *in vitro* chemical processes in the lab and for help with identifying suitable fittings, parts, nuts, and bolts.

The author would like to thank his roommate Narasimman Lakshminarasimman Meanakshi Se for listening to all of his trials and tribulations throughout this time and offering helpful suggestions, sustenance, and support.

Finally, the author would like to thank his Mother for always believing in him, supporting his pursuits from afar, and helping make this dream a reality.

The work encapsulated within this thesis was largely conducted during the COVID-19 pandemic (March 2020 – August 2021). In-person activities were restricted, severely limiting time available for lab work and office usage. Additionally, procurement of chemicals, materials, and equipment was significantly delayed due to pandemic-related supply chain issues.

Table of Contents

Author's Declaration ii
Abstract iii
Acknowledgements iv
List of Figures viii
List of Tables xi
Chapter 1 Introduction **1**
1.1 Introduction 1
1.2 Hypothesis 3
1.3 Objectives 3
Chapter 2 Literature Review **4**
2.1 Introduction to reactive oxygen species (ROS) chemistry in the human body 4
2.2 The role of ROS in the body 6
2.3 ROS regulation *in vivo* 8
2.4 Oxidative stress 9
2.5 Interactions between ROS and proteins 9
2.6 Cortical Bone 10
2.7 Oxidative Damage in cortical bone 11
2.8 Quantifying bone fragility using fracture mechanics 13
2.9 Transient reactive diffusion of ROS in cortical bone 20
2.10 Supercritical carbon dioxide 27
Chapter 3 Materials and Methods **30**
3.1 *In vitro* model process design 30
3.1.1 *In vitro* model conception 30
3.1.2 Process type 30
3.1.3 Oxidative damage simulation 31
3.2 Pore Network Modelling of bovine bone 32
3.3 Harvesting cortical bone beams from bovine tibiae 38
3.4 Reactive oxygen species soak experiment 39
3.5 Negative Controls of oxidative damage 42
3.6 Positive Controls of oxidative damage 42
3.7 Fracture Testing 43

3.8 Biochemical and Fluorescent Sample Characterization 44
3.8.1 Beam portioning 44
3.8.2 Bone slice surface demineralization 45
3.8.3 Fluorescein 5-thiosemicarbazide (FTC) surface staining of slice surfaces for carbonyls 45
3.8.4 Fluorescence microscopy for damage gradient imaging 46
3.8.5 Fluorescent image processing in ImageJ to analyze damage gradient 46
3.9 Statistical Analysis 47
Chapter 4 Results and Discussion 48
4.1 Pore network modelling 48
4.1.1 - 1.2 x 1.2 x 0.30 mm^3 network 48
4.1.1.1 Time to steady state 48
4.1.1.2 Transient diffusion concentration gradient 50
4.1.2 - 2.4 x 2.4 x 0.30 mm^3 network 55
4.1.2.1 Time to steady state 55
4.1.2.2 Transient diffusion concentration gradient 56
4.1.3 Sensitivity Analysis of k 61
4.2 Reactive Oxygen Species Soak Experiment 63
4.2.1 Fracture Testing Results 63
4.2.1.1 Load-deflection curves 63
4.2.1.2 Work to fracture 64
4.2.1.3 Fracture Toughness 66
4.2.1.4 Maximum deflection 68
4.2.1.5 Chevron notch area 70
4.2.2 Fluorescent Imaging 71
4.2.2.1 Raw image analysis 71
4.2.2.2 Image thresholding analysis 73
4.2.2.3 Mean pixel intensity analysis 75
4.2.2.4 Pixel intensity distribution analysis 76
4.3 Limitations 79
4.4 Overall Discussion 81
Chapter 5 Conclusions and Recommendations 82
5.1 Conclusions 82

5.2 Recommendations 84
5.3 Contributions 86
Bibliography **88**
Appendix **103**
Appendix A Supercritical Carbon Dioxide Process Design 103
A.1 Process Design and Assembly 103
A.1.1 Process type 103
A.1.2 Oxidative damage simulation 103
A.1.3 Process Flow Description 104
A.1.4 Process & Instrumentation Description 106
A.1.5 Equipment procurement 107
A.1.5.1 In-house process 107
A.1.5.2 Third-party process 110
A.1.6 Process Drawings and Bill of Materials 113

List of Figures

Figure 1 – The cycle of the generation of free radicals from hydrogen peroxide, their conversion to hydrogen peroxide, and the elimination of hydrogen peroxide from the system. **8**
Figure 2 – Chevron notch geometry. The beam is cut to leave behind the ligament (shown in red) connecting the two halves. **17**
Figure 3 – Block flow schematic for the selected batch process. **31**
Figure 4 – Preliminary 3D lattice of canals step in pore network generation. **33**
Figure 5 – Final rendered geometry visualized in Paraview. Entire domain shown**.** **34**
Figure 6 – Final rendered geometry visualized in Paraview. Cross-section taken halfway through z-domain to show canals within the matrix. **35**
Figure 7 – Conceptual formulation of the path taken by hydrogen peroxide molecules before decomposing into free radicals which react with bone collagen. Goulet et al. figure reprinted by permission from Springer Nature Customer Service Centre GmbH: Springer Nature Annals of Biomedical Engineering (Poroelastic evaluation of fluid movement through the lacunocanalicular system, Goulet, G.C., et al) © Springer Nature 2009. Furmanski, J, and Chakravartula, A., figures reproduced with permission of The Licensor through PLSclear from Furmanski, J., Chakravartula, A. Mechanics of Biomaterials Fundamental Principles for Implant Design © L. A. Pruitt and A. M. Chakravartula 2011. ..... **36**
Figure 8 – Dimensions and orientation of chevron notch cutting. **43**
Figure 9 – Schematic depicting how cortical bone beams were portioned following fracture testing. Abbreviations - Fluoro.: Fluorescent Imaging, Metal.: metallurigal, Frac.: Fracture, HIT: hydrothermal isometric tensile testing, Assays: hydroxyproline and carbonyl assays. **44**
Figure 10 – Normalized surveillance pore hydrogen peroxide concentration over time at each boundary condition with active reactions. **48**
Figure 11 – Normalized surveillance pore hydrogen peroxide concentration over time at each boundary condition without active reactions. **49**
Figure 12 – Hydrogen peroxide concentration in the surveillance pore located near the centre of the volume over time with active reactions. Note that the steady state concentrations are 15 orders of magnitude lower than when reactions are inactive. **50**
Figure 13 – Hydrogen peroxide concentration in the surveillance pore located near the centre of the volume over time without active reactions. **51**
Figure 14 – Transient diffusion of hydrogen peroxide into the RVE with boundary condition = 272 mmol/L. **53**
Figure 15 – Transient reactive diffusion of hydrogen peroxide into the RVE with boundary condition = 272 mmol/L. **54**
Figure 16 – Normalized surveillance pore hydrogen peroxide concentration over time at each boundary condition without active reactions. **55**
Figure 17 – Normalized surveillance pore hydrogen peroxide concentration over time at each boundary condition with active reactions. **56**
Figure 18 – Hydrogen peroxide concentration in the surveillance pore located near the centre of the volume over time without active reactions. **57**

Figure 19 – Hydrogen peroxide concentration in the surveillance pore located near the centre of the volume over time with active reactions. **57**
Figure 20 – Transient diffusion of hydrogen peroxide into the 2.4 x 2.4 x 0.30 mm^3 RVE with boundary condition = 272 mmol/L. **59**
Figure 21 – Transient reactive diffusion of hydrogen peroxide into the 2.4 x 2.4 x 0.30 mm^3 RVE with boundary condition = 272 mmol/L. **60**
Figure 22 – Parametric study of the reaction constant depicting its influence on the surveillance pore concentration in the 2.4 x 2.4 x 0.30 mm^3 RVE. Time interval 0 – 360 s. Boundary condition: 272 mM. **61**
Figure 23 – Parametric study on the reaction constant depicting the influence on the surveillance pore concentration in the 2.4 x 2.4 x 0.30 mm^3 RVE. Time interval 0 – 18 s showcasing the slight differences in concentration at different k values. Boundary condition: 272 mM. **62**
Figure 24 – Load-deflection curves for all specimens at all treatment levels. NC: no-catalyst negative control group; GR: gamma irradiated positive control group. **63**
Figure 25 – Work to fracture for all treatment and control groups. Significance was assigned at the $\alpha = 0.05$ level. Data presented as mean with standard deviation. GR: Gamma irradiated positive control; NC: no catalyst negative control. n = 3 for NC and GR. n = 2 for 0 – 544 mM. **64**
Figure 26 – Linear regression analysis of work to fracture as a function of hydrogen peroxide concentration for treated groups including 0 mM negative control. n = 2. Significance was assigned at the $\alpha = 0.05$ level. **65**
Figure 27 – Fracture toughness for all control and treatment groups. Significance was assigned at the $\alpha = 0.05$ level. Data presented as mean with standard deviation. GR: gamma irradiated positive oxidative damage controls; NC: no-catalyst negative controls. n = 3 for NC and GR. n = 2 for 0 – 544 mM. **66**
Figure 28 – Linear regression analysis of fracture toughness as a function of hydrogen peroxide concentration for treated groups including 0 mM negative control. Significance was assigned at $\alpha = 0.05$ level. n = 2 ..... **67**
Figure 29 – Maximum deflection for all groups. Significance was assigned at the $\alpha = 0.05$ level. Data presented as mean with standard deviation. GR: gamma irradiated controls; NC: no-catalyst controls. n = 3 for NC and GR. n = 2 for 0 – 544 mM. **68**
Figure 30 – Linear regression analysis of maximum deflection as a function of hydrogen peroxide concentration for treated groups including 0 M negative control. Significance was assigned at the $\alpha = 0.05$ level. n = 2. ..... **69**
Figure 31 – Mean chevron notch area for all groups. Significance was assigned at the $\alpha = 0.05$ level. n = 2. Data presented as mean with standard deviation. GR: gamma irradiated controls; NC: no-catalyst controls. n = 3 for NC and GR. n = 2 for 0 – 544 mM. **70**
Figure 32 – Z-projections of stitched raw fluorescent images taken of each sample using a confocal microscope. NC: no-catalyst negative control; GR: gamma irradiated positive control. GR z-stack: 400.1 µm. NC & 0 – 544 mM z-stack: 459.9 µm. Scale bars: 500 µm. **72**
Figure 33 – Stitched confocal microscopy images of FTC-stained bone beam slices after threshold application. Threshold was set according to 0 M (NC) sample fluorescence to remove 99.5% of

pixels. NC: no-catalyst negative control; GR: gamma irradiated positive control. GR z-stack: 400.1 µm. NC & 0 – 544 mM z-stack: 459.9 µm. Scale bars: 500 µm. **74**
Figure 34 – Full slice mean pixel intensity values for all groups. Significance was assigned at the α = 0.05 level. n = 1. Data presented as mean with standard deviation. GR: gamma irradiated controls; NC: no-catalyst controls. **75**
Figure 35 – Central ROI mean pixel intensity values for all groups. Significance was assigned at the α = 0.05 level. n = 1. Data presented as mean with standard deviation. GR: gamma irradiated controls; NC: no-catalyst controls. **76**
Figure 36 – Pixel intensity histograms for each specimen. Saturated pixels were those at the maximum possible pixel intensity value of 255. ..... **77**
Figure 37 – Area under the curve for all groups (n = 1). GR: gamma irradiated controls; NC: no-catalyst controls. **78**
Figure 38 – Three-dimensional rendering of the surface of the stitched confocal image for the gamma irradiated control specimen, illustrating its curved morphology. Z-stack: 400.1 µm. **80**

List of Tables

Table 1 – Properties input for the simulated aqueous hydrogen peroxide mixture. **37**
Table 2 – Boundary conditions applied in all pores on the faces normal to the x and y axes during transient reactive diffusion simulations **37**
Table 3 – Serial dilution table for the preparation of dilute hydrogen peroxide solutions for bone treatment. n = 2 for each treatment group (0.544 mol/L, 0.272 mol/L, and 0.136 mol/L). **41**
Table 4 – Bill of Materials for the designed in-house supercritical carbon dioxide process. **114**

Chapter 1
Introduction

1.1 Introduction

Increased bone fragility can result from age-related and chronic bone affecting diseases (such as osteoporosis, diabetes and kidney disease), endocrine and radiation-based cancer treatments, and/or trauma (1–5). Increased bone fragility increases the likelihood of bones fracturing beyond normal physiological frequencies, which in turn, increases the burden for patients in the form of pain, limited mobility, morbidity, and potentially the inability to live their lives with the dignity and freedom they are normally accustomed to (6). Additionally, treating increased numbers of bone fractures poses a significant burden on healthcare services, ballooning the total cost for treating bone fractures in a given jurisdiction. For example, the associated financial burden to the Canadian healthcare system is expected to increase with Canada's ageing population; the 65 or older demographic is expected to double to approximately 8.7M over the next 25 years (7). Hip fractures alone affect 30,000 Canadians per year and their associated cost is expected to increase to $2.4 billion annually by 2041 (8). Beyond costs to the healthcare system, additional costs to the Canadian economy may be incurred in the form of lost hours from workers with fractures preventing them from working either due to their own fractures or from the care they supply to loved ones with fractured bones.

In order to improve patient quality of life and reduce the associated costs to the healthcare system, it is critical to treat bone fragility at its incipient level, as opposed to merely reacting to the symptoms and consequences. To this end, an in-depth understanding of the mechanisms of bone fragility is ultimately required. This understanding can be achieved through the avenues of bone fracture mechanics and material science, enabling better comprehension of the mechanisms at play, which can ultimately be translated to better treatments, healthcare resource management, and care for patients, thereby reducing suffering and expenditures within the healthcare system.

Oxidative stress may be a key mechanism associated with bone fragility. Oxidative stress, also known as chronic inflammation, is caused by the imbalance between reactive oxygen species (ROS), including oxygen free radicals, and antioxidant defense mechanisms in the body for a prolonged period of time (9). Unregulated, ROS are capable of oxidatively modifying biomolecules, including proteins, lipids, carbohydrates, and DNA, to cause oxidative damage (10). The accumulation of oxidative damage can have detrimental effects on cellular, tissue, and organ-level function (11). With

respect to bone, oxidative damage can occur in the organic phase, which is primarily composed of type I collagen (12). While bone is also composed of a hydroxyapatite mineral phase, collagen has been shown to be the key component in bone which gives it its toughness and resistance to fracture, as measured by experimentally determining bone's fracture toughness parameter (13,14). Furthermore, diseases, such as chronic kidney disease, that cause a chronic state of oxidative stress in the body often coincide with poor bone quality, a measure which describes bone's material, architectural, and mechanical characteristics which contribute to bone strength and differs from bone mineral density (4,15,16). Increased levels of protein oxidative damage also correlate strongly with age, leading to theories that free radicals and ROS play an important role in the aging process (17). These changes with aging also relate to increased bone fragility at advanced age (18,19). Despite the high likelihood and degree of correlation, oxidative damage has not yet been confirmed as a mechanism of bone fragility.

Current studies of bone fragility rely on donated human cadaveric bone specimens. While studying human bone is ideal, donor specimens contain the histories of their donors, notably all of the bone-affecting pathologies or symptoms that may have been accumulated during their life. Additionally, most specimens donated are from donors of an advanced age, increasing the number of comorbidities each sample may have. The presence of these myriad influences can confound the results of study on the mechanisms of bone fragility, requiring the exclusion of many specimens from an already scarce supply.

A solution which could provide clearer insight would be a means of creating controlled levels of oxidative damage in healthy bone samples to allow direct study of the underlying mechanism without the presence of confounding sources of bone fragility. The existence of such a technique would allow the isolation of the link between oxidative damage and bone fragility in a controlled *in vitro* setting, enabling more insightful study. Additionally, this technique would also allow for studies to utilize more commonly available and affordable bone sources, such as bovine bone. While bovine bone may be less representative of human bone in composition, microstructure, mechanical properties, and the ability to undergo stable fracture, the ability to design more experiments that "think around the problem" would be advantageous for the field as a whole and could lead to better research outcomes. The outputs of this research could, in turn, fuel future discoveries in the field regarding the mechanisms of bone fragility and ultimately improve the quality of life for patients and reduce the burden on the Canadian healthcare system.

In the context of this thesis, the specific solution posed is the design of an *in vitro* model of controlled levels of physiologically relevant oxidative stress, a hypothesized mechanism for enhancing bone fragility *in vivo*, to create controlled levels of oxidative damage in bovine cortical bones.

1.2 Hypothesis

Treating bovine bone specimens with controlled and elevated levels of physiologically-relevant ROS will damage bone collagen and significantly reduce the bone's fracture toughness, thereby confirming oxidative damage as a mechanism of bone fragility.

1.3 Objectives

1) Design an *in vitro* model of controlled and elevated physiologically-relevant oxidative damage using bovine cortical bone
2) Conduct pore network modelling of the transient reactive diffusion occurring within the bovine cortical bone's porous structure to inform operation of the *in vitro* model
3) Validate the pore network model experimentally using results from the *in vitro* model

Chapter 2
Literature Review

2.1 Introduction to reactive oxygen species (ROS) chemistry in the human body

Reactive oxygen species (ROS) are highly reactive oxygen derived chemicals. In the context of biological systems, ROS are formed in all cells as products and by-products of mitochondrial and enzymatic activity and in immune cells specifically to combat pathogens (20).

Common ROS *in vivo* include hydrogen peroxide (H_2O_2), superoxide anions (O_2^-), nitric oxide (NO), and hypochlorite ions (ClO^-) (21). The ROS family also includes biologically-derived oxygen free radicals, such as the superoxide anion radical ($^{\cdot}O_2^-$) and the hydroxyl radical ($^{\cdot}OH$), which in addition to their chemically active oxygen atoms also have a characteristically unpaired valence electron which enhances their reactivity (22,23). These radical species are incredibly short-lived and react readily *in vivo* with other molecules in their immediate environment, including each other, making them the most toxic ROS for biological systems. When ROS react with and oxidize biomolecules in the body, they create oxidative damage in the form of altered functional groups which may abnormally alter biomolecular function. Specifically, these modifications, some termed Advanced Glycation Endproducts, have been implicated as biomarkers of increased bone fragility (24,25).

While levels of ROS observed during homeostasis are considered healthy and necessary in presenting pathologies such as chronic granulomatous disease, excessively high levels of ROS in the body are linked with many different pathologies including neurodegenerative diseases, diabetes, cancer, aging, and poor bone quality, a measure of increased bone fragility (4,9,17,26–29). Prolonged elevated levels of ROS is a condition known as oxidative stress or, more colloquially, as inflammation (9,30–33). During periods of oxidative stress, oxidative damage to biomolecules occurs more rapidly and in greater quantities, causing damage to tissues and organs often as a comorbidity to other pathologies. One posited example is the marked decrease in bone quality associated with oxidative stress brought on by chronic kidney disease (4). Bone quality is a measure which describes bone's material, architectural, and mechanical characteristics which contribute to bone strength and differs from bone mineral density (15,16).

While many ROS are generated *in vivo*, the most reactive free radicals are key in creating oxidative damage. $^{\cdot}O_2^-$ and $^{\cdot}$OH can be generated from water and less reactive ROS, notably O_2 and H_2O_2, radiatively using ultraviolet light and γ-irradiation, enzymatically via xanthine oxidase, and catalytically via metal-catalyzed or purely radical-based reaction pathways, including the Fenton and Fenton-like, and Haber-Weiss reaction pathways, respectively (34–37). In all cases, an electron is added to each substrate to generate the radical species. Focusing on the metal ion-catalyzed reaction pathway, the net Haber-Weiss reaction is as follows

$$H_2O_2 + {}^{\cdot}O_2^- \rightarrow {}^{\cdot}OH + OH^- + O_2$$

The Haber-Weiss reaction pathway is initiated catalytically

$$H_2O_2 + M^{n+} \rightarrow {}^{\cdot}OH + OH^- + M^{(n+1)+}.$$

In the event that M^{n+} is Fe^{2+}, then this reaction is known as the Fenton reaction.

$$H_2O_2 + Fe^{2+} \rightarrow {}^{\cdot}OH + OH^- + Fe^{3+}.$$

If M^{n+} is another transition metal ion capable of being oxidized, such as (Cu^+, Co^{2+}, etc.), then this reaction is known as the Fenton-like reaction (38,39).

Once generated, $^{\cdot}OH$ may react with H_2O_2 present to produce $^{\cdot}O_2^-$

$$^{\cdot}OH + H_2O_2 \rightarrow H_2O + {}^{\cdot}O_2^- + H^+$$

which in turn, may then react with any H_2O_2 present to propagate the radicals and produce vapor phase O_2

$$^{\cdot}O_2^- + H^+ + H_2O_2 \rightarrow O_2 + {}^{\cdot}OH + H_2O.$$

$^{\cdot}O_2^-$ is also capable of catalyzing the regeneration of the transition metal ion catalyst

$$M^{(n+1)+1} + {}^{\cdot}O_2^- \rightarrow M^{n+} + O_2.$$

The Haber-Weiss reaction pathway is terminated when the $^{\cdot}OH$ is scavenged by the transition metal ion catalyst

$$M^{2+} + {}^{\cdot}OH + H^+ \rightarrow M^{(n+1)+1} + H_2O.$$

Fe^{2+} and Fe^{3+} ions are widely available in cells and the human body owing to iron's use in common proteins such as the oxygen carrier hemoglobin and frequently used enzymes such as the cytochrome

P450 family (40,41). Other metals have been shown *in vitro* to catalyze H_2O_2's decomposition and it is suspected that those in abundance *in vivo*, including Cu^+, may also act in this manner (42,43).

Owing to the popularity and utility of the Fenton reaction, kinetic parameters have been reported for the iron-catalyzed reaction in laboratory and chemical process settings (44,45). These parameters are still forthcoming for biological systems, enzymatic reaction pathways, and those catalyzed by metals other than iron.

Additional sources of ROS production *in vivo* include pathways catalyzed by myeloperoxidase which, due to the presence of chlorine, utilizes hypochlorous acid ($HOCl$)

$$HOCl + \ {}^{\cdot}O_2^- \rightarrow \ {}^{\cdot}OH + O_2 + Cl^-$$

and in the presence of nitrogen utilizes nitric oxide ($NO^{\cdot}$), which subsequently reacts with the superoxide radical to produce peroxynitrite (46,47)

$$NO^{\cdot} + \ {}^{\cdot}O_2^- \rightarrow ONOO^-.$$

$NO^{\cdot}$ is produced from L-arginine within the mitochondria by the enzyme nitric oxide synthase (47).

Another source of endogenous ROS production is by immune cells in their attempt to kill invading pathogens or due to their own malfunctions, such as during the formation of foreign body giant cells in response to medical implants (27). Neutrophils produce a respiratory burst, which generates superoxide via the enzyme NADPH oxidase, as depicted in the following formula (48)

$$2O_2 + NADPH \rightarrow 2 \ {}^{\cdot}O_2^- + NADP^+ + H^+.$$

In bone tissue, osteoclasts also produce ${}^{\cdot}O_2^-$ during their bone resorption process to degrade the organic bone matrix and are suspected to do so following a similar NADPH oxidase pathway (49,50).

The topics presented above will be explored in more detail in the following sections with a specific focus on the tissue under study in this thesis: cortical bone.

2.2 The role of ROS in the body

ROS have myriad functions within the body during periods of homeostasis. They typically fall into three main categories: immune function, messenger signaling between cells, and homeostatic cell function. While immune function specifically relates to the immune system, the other two categories

are extremely broad in scope. For the sake of this review, only the subject matter most relevant to bone and oxidative stress have been covered from these two topics. Briefly, other ROS functions *in vivo* not discussed here include their roles in hormone regulation, modification of gene expression, vasodilation, spermatogenesis, and many other physiological processes (51–54).

As previously mentioned, ROS are produced by immune cells and used to combat infection by killing microbes and fungi (55). Phagocytes including neutrophils, eosinophils, mononuclear phagocytes, and leukocytes can produce large amounts of ROS specifically for this purpose during a respiratory burst via the NADPH oxidase pathway (56). When this enzyme fails to function, patients can become immunocompromised and experience recurrent infections including chronic granulomatous disease and pneumonia (26). As signaling messengers, ROS have been shown to regulate T-cell activation, apoptosis, and immune responses, notably with elevated ROS levels reducing T-cell responsiveness in the tumour microenvironment (56).

In bone tissue, osteoclasts, which are specialized descendants of hematopoeietic monocyte and macrophage precursor cells, also produce ROS (57). Osteoclasts act as part of the process of bone remodeling to resorb bone tissue. By creating an acid microenvironment (pH approx. 4.5) using HCl_{aq} secreted into a localized region created between the cell's membrane and the bone surface, osteoclasts are able to demineralize the bone and expose the organic matrix, which is largely composed of type I collagen (58). Osteoclasts then degrade the organic matrix using the enzyme cathepsin K and $\cdot O_2^-$ (58). The mechanism by which osteoclasts generate $\cdot O_2^-$ is still debated, however experimental evidence suggests that it could also be via NADPH oxidase, similarly to their immune cell ancestors (49,50). Interestingly, osteoclasts are also stimulated to resorb bone by ROS (59). While these signaling ROS are typically produced by osteoblasts within the bone, periods of oxidative stress may also cultivate the same effect, thereby enhancing osteoclast bone resorption activity to pathological levels, such as is seen in chronic kidney disease (4,60,61).

It has been suggested that ROS play a key role in regulating the aging process. Landmark studies in animal models have shown that at advanced age, test animals have higher levels of mitochondrial H_2O_2 (62). Additionally, levels of biomarkers for oxidative damage in lipids, proteins, and nucleic acids have been shown to correlate strongly with aging across different genera and species (63). The Free Radical Theory of Ageing, initially proposed by Harman, notes these correlations, defining aging as the accumulation of diverse and deleterious changes over time in cells and organisms that increase their chance of disease and death (17). Increased levels of oxidative damage in lipids,

proteins, and nucleic acids, while often a biomarker of oxidative stress and other pathologies, contribute to the disfunction of cells increasing their chance of disease, death, and/or senescence (64).

2.3 ROS regulation *in vivo*

ROS levels are regulated *in vivo* by specific enzymes and antioxidant scavengers (65). The enzyme superoxide dismutase catalyzes the conversion of $^{\cdot}OH$ and $^{\cdot}O_2^-$ into the less reactive H_2O_2 (30). H_2O_2 can then be converted into the relatively harmless and more biologically useful products H_2O and O_2 via the enzymes catalase or glutathione peroxidase (Figure 1) (29,66). Thioredoxin enzymes enable the reduction of oxidized proteins (9). Antioxidant scavengers present *in vivo* include tocopherols (vitamin E's), Retinol (vitamin A's), and ascorbate (vitamin C), cartenoids, uric acid, and polyphenols (9,32,67). These antioxidants scavenge free radicals and vary in abundance regionally throughout the body's tissues, depending on an individual's diet and supplementation (68).

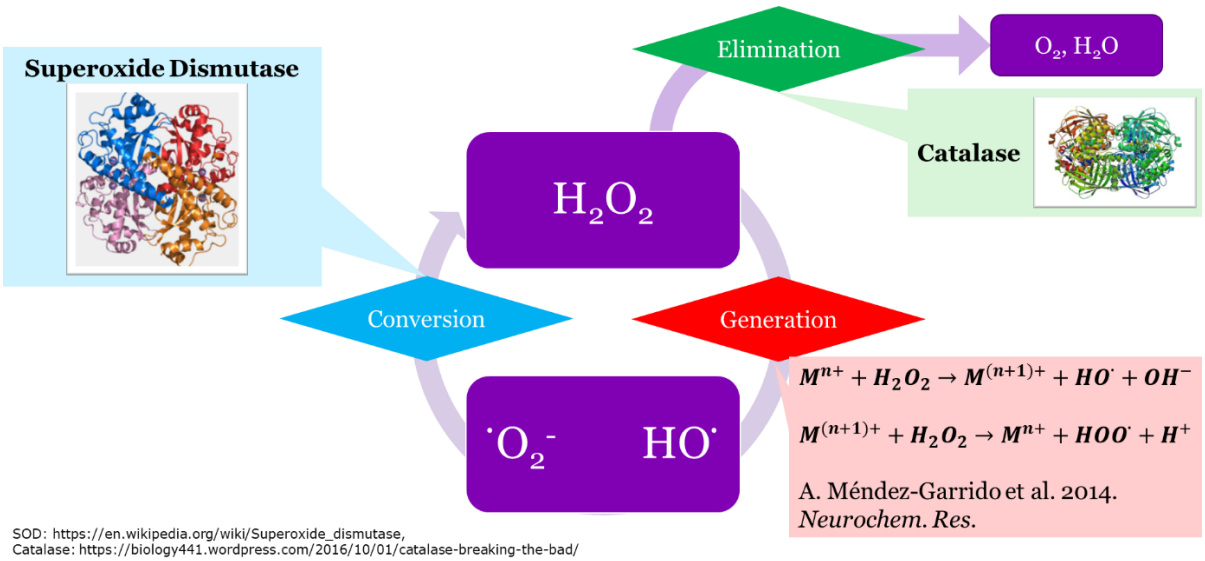

Figure 1 – The cycle of the generation of free radicals from hydrogen peroxide, their conversion to hydrogen peroxide, and the elimination of hydrogen peroxide from the system.

2.4 Oxidative stress

Typically, the body combats high levels of ROS using naturally occurring antioxidants, however, with inhibition or dysfunction of these enzymes or compounds, and/or elevated ROS production, ROS levels in the body can increase beyond desired physiological levels. This imbalance is known as inflammation. If the ROS/antioxidant imbalance persists for prolonged periods of time, it is termed chronic inflammation or oxidative stress (68,69). Oxidative stress can stem from many disease states or medical treatments, notably chronic kidney disease, diabetes, chemotherapy, and aging (11,17,32,69).

Additionally, oxidative stress has been implicated in the causality of many diseases, resulting from the ensuing pathological levels of oxidative damage of biomolecules *in vivo*. ROS may induce modifications in nucleic acids and have been suggested as the culprit of DNA mutations which cause cancer (11). The high levels of ROS can also readily oxidize lipids in cell membranes, compromising their ability to sequester the cytosol (70). Carbohydrates may also be oxidized, fragmenting polysaccharides by breaking glycosidic bonds (71). ROS are also capable of overstimulating cellular dysfunction and apoptosis pathways (72). Finally, ROS can interact with proteins, which will be discussed in more detail in the following section.

2.5 Interactions between ROS and proteins

ROS free radicals are also capable of oxidizing proteins (10). Hydroxyl radicals have been identified as the primary radical species which react with proteins (65). Hydroxyl radicals abstract (take) hydrogens from the alpha-carbon in amino acids and other molecules to form water (73). As radicals they react extremely quickly and these hydrogen atom abstractions often form carbon radicals, which can have severe consequences for the structure of these peptides due to the subsequent chemical reorganization to nullify the carbon radical. Often, these carbon radicals form carbonyls, a standard indicator of oxidative damage, however they may also form Advanced Glycation End-products (AGEs), including increasing the number of crosslinks between molecules in the collagen matrix and/or the number of adducts, such as carboxymethyl-lysine (28,64,74).

The carbon radical can further react with *in situ* oxygen, Fe^{2+} + H^{+}, Cu^{+}, and/or $HO_2^{\cdot}$ to prime the cleavage of the backbone of the peptide (73,75,76). These carbon radicals may also propagate throughout the same or different neighboring peptides as the incipient carbon radical reacts with

them, further propagating the potential backbone lysis or forming protein-protein crosslinks (73). Once primed, the peptide backbone cleavage may occur via the diamide or α-amidation pathways (10,73).

Structural proteins, which bridge the gap between form and function for tissues, can be significantly oxidatively damaged by ROS (77). This damage can accumulate in longer lived structural proteins, such as the collagen present in skin, arteries, and bone tissue and impairing their function by causing them to be more fragile. More detail will be given in the following section on this damage in cortical bone tissue.

2.6 Cortical Bone

Cortical bone, also known as compact bone, is the dense and load bearing bone tissue which makes up the shafts of long bones as well as encapsulates their ends and other bones in the human body in a thin layer (78). The other major type of mature bone in the human body is trabecular (cancellous) bone, which composes the vast majority of the volume of the ends of long bones and is recognizable by its distinctive spongy structure (78).

Cortical bone is an intricate composite of hydroxyapatite and Type I collagen (78). At the nanometer scale, tropocollagen molecules are crosslinked linked together and the gaps between molecules are infilled with inorganic hydroxyapatite crystals (79). Collagen molecules themselves are triple helices of peptide chains, each chain having the regular pattern of glycine-X-Y, where X is often proline and Y is a third amino acid (80). The triple helix structure is referred to as a tropocollagen molecule and is approximately 300 nm in length and 1 nm in diameter (81). Tropocollagen molecules are oriented approximately parallel to one another along their long axes and the spaces between them are infilled with nanohydroxyapatite crystals. These mineralized molecules form a biological fibrous composite material, where the toughness and resistance to fracture is provided by the collagen, while the rigidity is enhanced by the mineral crystals.

At the millimeter scale, mineralized tropocollagen molecules come together to form mineralized collagen fibrils approximately 1 mm in length (82), These fibrils, in turn, combine to form fibril arrays approximately 10 mm in length. Arrays are oriented in fibre patterns, composing lamellae, thin layers of composite material which are wrapped cylindrically about an axis to form osteons, the basic functional unit of cortical bone, at the 100 mm length scale (78,82). Osteons have hollow centres,

known as Haversian canals and are surrounded on the outside of their lamellae by layers of pure mineral phase known as cement lines which prevent the diffusion of nutrients outside of the osteon (78). In long bones, osteons are oriented along the long axis of each bone's shaft. Haversian canals allow blood vessels and interstitial fluid to pass through the solid bone tissue and provide nutrients to the osteoblasts living within. Haversian canals are connected transversely by Volkmann's canals, which provide space in the bone for anastomosing vessels to connect with Haversian canal blood vessels (79). In bovine cortical bone, these canals are approximately 30 μm in diameter and are spaced approximately 300 μm apart (83–85).

Cortical bone's basic constituents give it its necessary structural properties (82). Hydroxyapatite functions to provide resistance to compressive loads while collagen serves to resist tensile loads (78). The overall composite functions much akin to reinforced concrete, where the concrete is analogous to the mineral matrix while the steel rebar functions similarly to the collagen. Physiologically, bones are frequently subjected to compressive loads and bending moments, in which both tensile and compressive forces are present, and therefore must be tough in order to avoid unwanted failure. Increased bone fragility increases the likelihood that these bending moment applications will result in a fracture.

The hierarchical structure of cortical bone, in turn, results in a hierarchically porous material. At the sub-micron scale, the pores within the matrix exist between neighboring hydroxyapatite crystals and tropocollagen molecules. At larger length scales, porous structures serve salient physiological functions. Lacunae (approx. 4 – 7 μm in diameter) house osteocytes which maintain and remodel the bone matrix by signaling osteoblasts to produce mineral and organic bone matrix and osteoclasts to disintegrate it (83,84,86,87). Lacunae are connected by canals known as canaliculi (approx. 1 μm in diameter) which house the osteocyte processes (87). These canals allow the osteocytes to interlink into a communication network, much like neurons. *In vivo*, both lacunae and canaliculi are also filled with extracellular fluid, which acts as a conduit for nutrients and wastes entering and leaving the cells.

2.7 Oxidative Damage in cortical bone

Oxidative damage in cortical bone largely only affects the organic matrix which is much more chemically vulnerable to oxidative modifications than the mineral phase. During oxidative stress,

ROS produced either *in situ* within the tissue by osteoclasts, osteoblasts, or immune cells or nearby diffuse through the void spaces created by cortical bone's hierarchical structure. This porosity also provides a high surface area for reaction of ROS with the bone matrix. ROS less than 300 Da in size are able to readily diffuse through the inorganic bone matrix (88–91). While diffusing through the bone, these ROS may react with the collagen molecules present and cause oxidative damage. It has been established in the literature that oxidative damage of bone collagen by extreme methods, particularly gamma irradiation, results in decreased fracture toughness (12). It is likely that increase in fragility will be observed if chronic oxidative damage is instead caused by physiologically-relevant ROS.

In collagenous connective tissues, reactive carbonyls produced by oxidative damage can bind to lysine or arginine residues in collagen molecules produce advanced glycation end-products (AGEs) (92). AGEs are non-enzymatic post-translational modifications of collagen fibrils. While enzymatic crosslinks between collagen fibrils are essential during normal development of the collagen matrix and play a major role in physiological bone strength, additional non-enzymatic crosslinks can cause the collagen network to become overly connected and the bone to become more brittle (93). Naturally occurring crosslinks formed by the enzyme lysyl oxidase include dihydroxyllysinonorleucine (DHLNL), hydroxylysinonorleucine (HLNL), lysinonorleucine (LNL), pyridinoline (PYD), and deoxypyridinoline (94). The most well-known AGE crosslink is pentosidine due to its relative ease of measurement stemming from its hydrolytically stable chemical structure (95). AGEs also include adducts, which are post-translational modifications of proteins that result in the insertion of a functional group onto the reacted molecule rather than the formation of a crosslink. Notable adducts in bone biochemical research include N^{ϵ}-(carboxymethyl)lysine (CML) and N^{ϵ}-(carboxyethyl)lysine (CEL) (94,96). CML in particular has garnered recent research interest AGEs have been shown to correlate with bone fragility and are a popular topic of study in the field (24,28,97). Despite their correlation with bone fragility, AGEs are unable to completely explain the mechanistic changes in collagen network connectivity and increased fragility in cortical bone, leading some researchers to hypothesize that the collagen is modified in other ways, for example, that collagen molecular backbones are cleaved by ROS during periods of oxidative stress and that this contributes significantly to decreased collagen network connectivity and increased bone fragility (12,98).

Increased bone fragility may also be a result of increased porosity, as is the case of poor bone quality resulting from osteoporosis (99). The overall porosity of healthy human cortical bone is

approximately 8% (100). For bovine cortical bone it ranges from 5 – 8% for older and younger animals, respectively (84,101). While the loss of bone tissue relates well to changes in bone's ability to resist fracture as a structure, it is hypothesized that changes in collagen network integrity supply a larger contribution to increased fragility. Historically, bone mineral density (BMD) was developed as a metric for assessing increased porosity stemming from osteoporosis and was used to diagnose increased bone fragility, and this practice continues to this day. BMD is measured by analyzing patient X-ray images (102). The disadvantage of using X-rays is that they can only return images of the mineral phase of bone, making them unable to image the organic matrix. As a result, BMD does not take into account important changes in collagen network connectivity which are highly posited to contribute significantly to increased bone fragility (93).

As the major consequence of increased bone fragility is bone fractures, tools for assessing a material's resistance to fracture are well suited to this analysis. The field of fracture mechanics seeks to describe how materials fracture, including the energy and forces required for stable and unstable fracture. Fracture mechanics also examines intrinsic and extrinsic fracture resistance mechanisms and their contributions to a material's fracture resistance. Fracture mechanics and its applications in quantifying bone fragility will be discussed in more detail in the following section.

2.8 Quantifying bone fragility using fracture mechanics

Understanding the mechanistic causes of bone fragility can be tackled by understanding the behaviour of energy within the cortical bone system. Although bone is known to not follow Linear Elastic Fracture Mechanics (LEFM), considering the LEFM perspective helps to establish the thermodynamic basis of its fracture (103).

Examining the energy balance of a crack in a material and taking the derivative with respect to time we see that

$$\dot{U}_e = \dot{U}_d + \dot{U}_s + \dot{U}_k + BR\dot{a} \quad (1)$$

Where $\dot{U}_e$ is the rate of external work performed, $\dot{U}_d$ is the rate of energy dissipation (due to mechanisms away from the crack), $\dot{U}_s$ is the rate of release of stored elastic energy, $\dot{U}_k$ is the rate of release of the kinetic energy of the crack, B is the material thickness, R is the crack resistance (ie. due to intrinsic and extrinsic toughening mechanisms in the material), and $\dot{a}$ is the speed of the crack tip

as it advances through the material (103). Assuming that all of the energy is dissipated is due to crack resistance, it can be said that $\dot{U}_d = 0$. Additionally, it is assumed that no kinetic energy is gained by the material during fracture, therefore $\dot{U}_k = 0$.

At the point where fracture initiates, $R = G$, where G is the energy release rate and can be defined as follows according to LEFM

$$G = \frac{1}{B}\left(\frac{dU_e}{da} - \frac{dU_s}{da}\right) \tag{2}$$

G represents the energy applied to create the new fracture surfaces, which is naturally an energetically unfavorable process (104). G includes, energy externally applied to the crack, U_e, in any of the three modes of loading via external stresses. It also includes stored elastic energy, U_s, released from the material itself as the local deformations caused by a crack and its associated loading cause adjacent volumes of the material to relax elastically (105). Essentially, the energy added to the system by the external work performed on it causes cracks in the material to grow and these cracks release energy as they create new surfaces in the material.

R is the opposing force to G, and encapsulates the material's fracture resistance mechanisms based on its composition and bonding (103). These mechanisms each serve as energy sinks to dissipate the applied energy and avoid fracture. On an energy basis, the energy absorbed from each dissipative mechanism can be summed to calculate the total value of R. When $G > R$, the crack length will grow (103).

During stable crack growth

$$\frac{dG}{da} \leq \frac{dR}{da} \tag{3}$$

and the crack does not grow unbounded. The crack grows gradually over time until the material fractures. This is distinct from unstable crack growth, where the material fractures immediately upon the following relation being true:

$$\frac{dG}{da} > \frac{dR}{da}. \tag{4}$$

Stable crack growth occurs according to Equation (3). During initial material loading prior to crack formation, the relation between G and a is linear. After reaching a critical value, G_c, the crack begins to grow and the relation between G and a becomes nonlinear as the resistance mechanisms of the

material undergoing fracture activate to combat this crack growth. This leads to the formation of a characteristic R curve (R vs a), which, as its response is due to characteristics of the material alone, can be viewed as an intrinsic material property (106). For brittle materials, such as ceramics, there are no significant resistance mechanisms, and as such, unbounded fracture occurs immediately at G_c. Materials with significant toughening mechanisms will develop a nonlinear R curve after G_c as their resistance mechanisms come into effect. The clearest example is in ductile metals, where such salient mechanisms as large-scale plastic deformation attempt to dissipate the energy supplied for crack growth.

A material's R curve can be leveraged to determine measures of its resistance to fracture (toughness). For more brittle materials, the stress intensity factor K is used for this purpose (107). At the crack tip, the stress experienced by the material is theoretically infinite, due to the finite applied force and the infinitely small crack tip area. K specifies the relative strength of this stress singularity outside the material breakdown region surrounding the crack tip, thereby describing the severity of the stress near the crack tip. The severity of this stress describes the likelihood of fracture in the material, with higher severity increasing the likelihood of fracture. K is given by

$$K = F\left(\frac{a}{W}\right)\left(\frac{P}{B * \sqrt{W}}\right) \tag{5}$$

where P is the applied load, B is the specimen thickness, W is the effective specimen length, and the function $F\left(\frac{a}{W}\right)$ is functions as a geometric factor and is tabulated for specific specimen geometry. K_c is defined as the critical stress intensity factor. When $K = K_c$, the material will undergo unstable fracture, and is therefore used as a measure of fracture strength (108).

An analogous metric is peak load experienced by the sample during fracture testing, P_{max}, normalized to fracture surface area, also known as ligament area, A_{frac}. This metric functions on the basis that the maximum load before fracture indicates fracture strength for a material, functioning on a slightly simpler principle than K. Peak load normalized to fracture surface area is defined as

$$Normalized\ Peak\ Load = \frac{P_{max}}{A_{frac}}. \tag{6}$$

Similar to P_{max}, maximum deflection, d_{max}, is also used as a simple indicator of resistance to fracture. Materials with a higher d_{max} often undergo more stable fracture, indicating a greater

fracture toughness, however this is not always the case. d_{max} is simply obtained as the maximum deflection of the sample during testing at the point of specimen rupture.

For less brittle materials, the intensely stressed area surrounding the crack tip can no longer be assumed to be small and a constant K_c value does not exist. More sophisticated methods must be used to quantify resistance to fracture in these materials. Elastic-plastic fracture mechanics takes into account the region surrounding the crack tip by using the J contour integral (J-integral for short) to capture the nonlinear energy release rate (107).

The J-integral is given as

$$J = \oint_{\Gamma} \left(w dy - T_i \left(\frac{\partial u_i}{\partial x} \right) ds \right) \tag{7}$$

where Γ the closed curve with arc length ds upon which the contour integral operates, w is the strain energy density, T_i are the components of the traction vector with the stress incident on a plane with unit normal vector normal to Γ, and u_I are the components of the displacement vector describing the movement of the crack front.

Strain energy density is defined as

$$w = \int_0^{\epsilon_{ij}} \sigma_{ij} d\epsilon_{ij} \tag{8}$$

where $\sigma_{ij}$is a component from the stress tensor and $\epsilon_{ij}$is a component from the strain tensor.

T_i is defined as

$$T_i = \sigma_{ij} n_j \tag{9}$$

where n_j is the j^{th} component of the plane's normal unit vector. When studying the fracture resistance of human cortical bone, a material that is considerably more resistant to fracture than bovine bone, the J-integral is more commonly used. One key advantage of this approach is while mechanical properties of bone obtained during compressive or tensile loading that fall in the linear region of stress-strain response, such as elastic modulus, are largely unaffected by oxidative damage, however the nonlinear post-yield behaviour is. The J-integral readily captures this nonlinearity, thereby painting a much more accurate picture of the bone's actual fracture toughness.

One relative measure of material toughness is work-to-fracture (12,19). Work-to-fracture measures the total energy required to fracture a specimen and is defined as the area under the load-deflection curve generated during fracture testing divided by the ligament area. The area under the curve can be computed practically using the trapezoid rule:

$$W_f = \frac{1}{A_{frac}} \int_{i=1}^{n} P dx = \frac{1}{A_{frac}} \sum_{i=1}^{n} \left(\frac{(P_i + P_{i-1})}{2} \right) \left((x_i - x_{i-x}) \right) \quad . \tag{10}$$

In practice, fracture testing of bone specimens is done following standard material fracture testing practice for ceramics as outlined by the ASTM International, formerly the American Society for Testing and Materials. The specific standard ASTM C1421 − 18: Standard Test Methods for Determination of Fracture Toughness of Advanced Ceramics at Ambient Temperature, details testing machine configurations as well as specimen notching requirements (109). The practical aspects of fracture testing will be discussed in more detail in the relevant Materials and Methods, but general concepts will be briefly summarized here.

Rectangular prism beams of material are subjected to bending loads in either 3-point or 4-point bending configurations. 4-point bending adds an extra crosshead contact point with the beam, allowing the bending load to be distributed more evenly along its length. Beams are notched to create an artificial stress concentration with the intent of controlling the direction of fracture. Two main types of notching are the single edge bending notch (SENB) and the chevron notch approach. SENB notching requires cutting a straight groove into the beam and sharpening it with a razor blade to create the desired stress concentration. They have the advantage of allowing visualization of the crack's progression during fracture

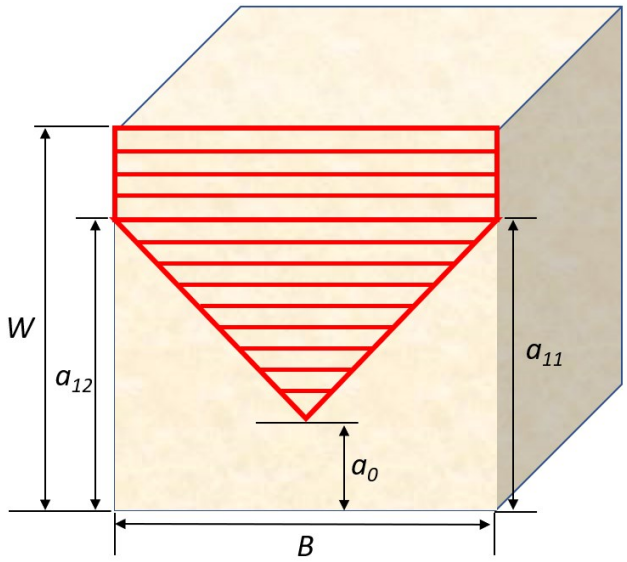

Figure 2 – Chevron notch geometry. The beam is cut to leave behind the ligament (shown in red) connecting the two halves.

testing on the surface of the material. Chevron notches are a standard material fracture testing practice as outlined in ASTM C1421, whereby the notch is cut such that the remaining material presents a stress concentration located at the tip of a chevron-shaped ligament as shown in Figure 2 (109). As the stress concentration, the tip of the chevron, is embedded deep within the beam's cross-section, visualization of the crack's progression is less feasible. As a result, W_f is often determined from fracture testing data generated using a chevron notch, as the crack length at each timepoint is not needed for calculation (19).

ASTM C1421 also proposes a method to calculate fracture toughness for chevron notched specimens tested under 3- or 4-point bending (109)

$$\mathrm{K_{Ivb}} = Y^*_{\min} \left[\frac{P_{\max} \ [S_o - S_i]10^{-6}}{BW^{\frac{3}{2}}}\right] \tag{11}$$

where $\mathrm{K_{Ivb}}$ is the fracture toughness in MPA $\sqrt{\mathrm{m}}$, $Y^*_{\min}$ is the minimum stress intensity factor as determined based on specimen geometries and is dimensionless, $P_{\max}$ is the maximum load experience by the sample during stable fracture, S_o is the outer span of the tested beam in m, S_i is the inner span of the tested beam in m, B is the side-to-side dimension of the test specimen perpendicular to the crack length (depth) in m, and W is the top-to-bottom dimension of the test specimen parallel to the crack length (depth) in m.

$Y^*_{\min}$ is defined in ASTM C1421 for 3- and 4-point bending test configurations assuming crack propagation behaviour and subsequent curve fit between W and the chevron notch dimensions a_0 and a_1. a_0 is the distance measured from the chevron notch tip to the opposite edge of the sample cross-section while a_1 is the average height of the notch, calculated as the average of the notch height measured from the opposite edge to the point on each side of the notch tip where the notch edges meet the sides of the sample cross-section.

In the context of bone fracture testing, applying the straight-through crack assumption and particular curve fit of $Y^*_{\min}$ to $\frac{a_0}{W}$ and $\frac{a_1}{W}$ for geometry D in ASTM C1421, the minimum stress intensity factor is defined as follows

$$Y^*_{\min}\quad\left(\frac{a_0}{W},\frac{a_1}{W}\right)$$
$$=\frac{0.5256-3.4872\left(\frac{a_0}{W}\right)+3.9861\left(\frac{a_1}{W}\right)-2.0038\left(\frac{a_1}{W}\right)^2+0.5489\left(\frac{a_1}{W}\right)^3}{1.0000-2.9050\left(\frac{a_0}{W}\right)+2.7174\left(\frac{a_0}{W}\right)^2-0.8963\left(\frac{a_0}{W}\right)^3+0.0361\left(\frac{a_1}{W}\right)} \tag{12}$$

for $0.322 \leq \frac{a_0}{W} 0.380$ and $0.950 \leq \frac{a_1}{W} \leq 1.000$ and a maximum error of 1%.

The embedded straight-through crack assumption assumes that stress intensity K in a crack produced using a chevron notch is related to minimum stress intensity function Y at any load P by the following relation (110)

$$K = \frac{P}{B\sqrt{W}}Y. \tag{13}$$

The definition of K_{Ivb} more closely resembles that of the stress intensity factor K as opposed to the fracture toughness measured using the J-integral. This is due to the assumptions made to develop the relations in ASTM C1421, which is a standard for testing brittle ceramic materials. In the context of cortical bone fracture mechanics, K_{Ivb} would be more suited to bones with more brittle behaviour, such as bovine cortical bone, as opposed to human bone.

As described by (111), intrinsic and extrinsic fracture toughening mechanisms exist in materials and serve to dissipate energy added to the material by loading and energy released by the creation of fracture surfaces as the crack progresses to avoid fracture. Intrinsic mechanisms refer to those which occur at the micro and smaller scales ahead of the crack tip while extrinsic mechanisms occur at the macro scale behind the crack tip. Intrinsic toughening mechanisms can contribute to extrinsic mechanisms, and vice versa. In the context of cortical bone, extrinsic fracture resistance mechanisms include crack bridging by uncracked ligaments, crack bridging by intact collagen fibrils, macroscopic crack deflection, and microcracking (14,112–114). Intrinsic mechanisms include hidden length (sacrificial bonds), smaller scale microcracking and fibrillar sliding (115–117). These mechanisms, made possible by the presence of the organic collagen matrix, provide bone with its fracture toughness.

While bone's resistance to fracture can be measured, its mechanisms can be posited, and decreases in fracture toughness have been observed due to oxidative damage of the collagen matrix, confirmation

of this same mechanism *in vivo* due to physiologically-relevant ROS has yet to be achieved. In order for ROS to oxidatively damage bone collagen, they must come into contact with it. Thus, having established the fracture mechanics for quantifying changes in fracture resistance, it is equally important to examine the transport of ROS through the bone's porous network and the underlying transport phenomena theory, as will be discussed in the following section.

2.9 Transient reactive diffusion of ROS in cortical bone

The field of transport phenomena seeks to describe the movement of mass, momentum, and energy through space and over time (118). Mass transport generally encompasses the movement of molecules, atoms, and particles through media, while momentum transport focuses on the flow and convective movement of these media particles. Energy transport is commonly defined as heat transport, where the flow of energy from one spatial location to another is studied. As an illustrative example, consider a control volume of water in the ocean. Within this control volume, there can be fluid flow (momentum transport), diffusion of solutes and chemicals (mass transport) and conduction of heat between the various layers in the water column (energy transport). Additionally, transport phenomena can also encompass the movement of electrons in a control volume (i.e., in a wire), however electron transport will not be discussed further as it is less relevant to the nature of this literature review.

The key driving force behind all transport phenomena are spatial gradients. All quantities travel from regions of high concentration or temperature to regions with lower densities of these quantities. Mass transport is driven by concentration gradients, momentum transport by pressure gradients, and energy transport by temperature gradients.

Transport phenomena rarely occur in isolation of one another, and these combined effects are more representative of real-world systems. The various density gradients may all be superimposed on one another, resulting in the interactions of different transport phenomena with each other. For example, convection may describe the combination of fluid flow (momentum transport) with diffusion (mass transport) and/or heat flow (energy transport). Returning to the ocean water example to illustrate this effect, warmer water will naturally rise within the water column via natural convection. This water will carry solutes and thermal energy with it, moving them to a location higher in the water column

and thereby altering the mass, momentum, and temperature gradients within the system and, in turn, subsequent transport.

A sub-field within transport phenomena is the study of transport within porous materials (118). Porous media are composed of two phases: a void phase composed of pores and a solid phase composed of the material itself. Pores are defined as small volumes of void space interconnected throughout the material, although not all pores are likely connected to one another in reality. To be classified as porous media, the pores within the material must typically be smaller than 1 mm in diameter. Below this threshold, capillary forces become non-negligible, the Reynolds number decreases, and assumptions and correlations specifically designed for porous media become more relevant. At the nanometer scale, all materials are porous due to the spaces between their atoms. Examples of artificial porous materials include filters, zeolite catalysts, membranes, electrodes, and clothes. Examples of naturally occurring porous materials include cellulose, sand packs, soil, snow, and biological tissues, notably bone.

The flow regime of a fluid is governed by the Reynolds number, Re , which is a dimensionless group that expresses the ratio of momentum to viscous forces in a flowing fluid. Reynolds number is given as

$$Re = \frac{\rho v L}{\mu} \tag{14}$$

where ρ is the fluid's mass density, v is the bulk fluid velocity, L is the characteristic length scale of the geometry through which the fluid is flowing, and μ is the dynamic viscosity of the fluid all in SI units. In the context of porous media, the characteristic length scale is the pore diameter. For pores on the other of tens of microns, as we see in cortical bone, and assuming fluid flow within them is akin to flow in a cylindrical pipe, Re becomes quite small, resulting in a value below the threshold between laminar and transition flow in a pipe of 2000. This means that if fluid flow exists in cortical bone, it is likely to be in the laminar flow regime.

Capillary forces present in porous media is measured as capillary pressure. When a fluid enters a given pore (the invading fluid), it must overcome that pore's capillary pressure in order to gain entry. The fluid already present in the pore (the defending fluid) must be displaced. Capillary pressure indicates the pressure required in the invading fluid to successfully displace the defending fluid and enter a given pore. Capillary pressure P_C is a function of the surface tension σ at the interface between the invading and defending fluid, the contact angle θ between the invading fluid and the solid

measured through the fluid phase, and r the radius of the capillary or pore into which the fluid is invading. Capillary pressure is determined using the Washburn equation:

$$P_C = \frac{-2\sigma \cos(\theta)}{r}. \tag{15}$$

As is evident from the Washburn equation, a perfectly wetting fluid ($\theta = 0$) would cancel out the cosine term while an imperfectly wetting fluid with $\theta > 0$ and be factored into the analysis. Additionally, a pore's capillary pressure is inversely proportional to its radius. As the radius decreases, the capillary pressure increases, meaning that the smaller the pore, the higher the applied pressure required for fluid to flow into it. As a result, pores on the order of tens of microns may have very high capillary pressures, inhibiting fluid flow into the porous medium if applied pressures are below the threshold. In the context of cortical bone pores, Haversian/Volkmann's canals and lacunae are approximately 30 μm and 4 μm in diameter, respectively, suggesting that very high pressures will be required to force fluid to flow into the medium.

Transport of small molecules like ROS in porous media is based on momentum and mass transport, both of which follow the general conservation equation, as do all transport phenomena, derived from mass flux through a control volume. Within the control volume, the driving force for momentum transport is a gradient in pressure, while the driving force for mass transport is a gradient in concentration. Assuming temperature to be constant, the equation describing momentum transport in a continuum is

$$\begin{aligned}[rate\ of\ increase\ of\ momentum] \\ = [rate\ of\ momentum\ in] - [rate\ of\ momentum\ out] \\ + [external\ force\ on\ the\ fluid]\end{aligned}$$

and written mathematically

$$\frac{\partial}{\partial t}\rho \boldsymbol{v} = -[\boldsymbol{\nabla} \cdot \rho \mathbf{v}\mathbf{v}] - \nabla \mathrm{p} - [\boldsymbol{\nabla} \cdot \boldsymbol{\tau}] + \rho \mathbf{g} \tag{16}$$

where ρ is the mass concentration, $\boldsymbol{v}$ is the velocity vector, p is the pressure field, $\boldsymbol{\tau}$ is the viscous momentum flux tensor which captures viscous effects in fluid flow when they become significant, and $\mathbf{g}$ is a vector which captures the acceleration due to gravity. At the scale of pores in cortical bone, the gravitational term may be omitted.

$$\frac{\partial}{\partial t}p\boldsymbol{v} = -[\boldsymbol{\nabla} \cdot \rho\mathbf{v}\mathbf{v}] - \nabla \mathrm{p} - [\boldsymbol{\nabla} \cdot \boldsymbol{\tau}] \tag{17}$$

As previously noted, within the porous cortical bone system, it is challenging to flow or diffuse these solutions into bones, as the high capillary pressures required for flow into the small pores are often prohibitive. Assuming the capillary pressure P_C is much greater than the external pressure field as stated earlier, the fluid will not flow into the bone's pores and the velocity vector into the control volume will be zero. As a result, of the lack of flow into, out of, or within the bone, the pressure gradient will also become zero, as will the viscous momentum flux tensor. Equation (12) thus simplifies to

$$\frac{\partial}{\partial t}p\boldsymbol{v} = 0 \tag{18}$$

communicating that there will be no momentum transport within the porous bone matrix according to the stated assumptions.

Similarly for mass transport in the same continuum control volume, sparing the derivation and assuming binary Fickian diffusion of species A in species B, we arrive at the well-known Fick's Law

$$\boldsymbol{j}_A = -\rho\mathcal{D}_{AB}\boldsymbol{\nabla}\omega_{\mathrm{A}} \tag{19}$$

where $\boldsymbol{j}_A$ is the molar flux of species A, ρ is the mass density within the control volume, $\mathcal{D}_{AB}$ is the diffusivity of species A in species B, ω_{A} is the mass fraction of species A within the control volume and the average velocity within the control volume is zero, in other words

$$\boldsymbol{v}_A + \boldsymbol{v}_B = 0 \tag{20}$$

due to the equimolar counter-current diffusion assumption. Additionally, the diffusivity of A in B is the same as B in A

$$\mathcal{D}_{AB} = \mathcal{D}_{BA} \tag{21}$$

allowing diffusion within the system to be described purely in terms of species A.

As species may diffuse into pores unimpeded, provided the molecules are smaller than the pore diameter, this diffusion may be said to take place within the porous bone control volume. In this particular case, it is assumed that the ROS particles are much smaller than the size of the pores,

allowing the continued use of Fickian diffusion without having to utilize Knudsen diffusion, as may typically happen when modelling mass transport in porous media.

As the ROS will react within the bone's porous matrix with any biomolecules present, it is pertinent to include a reaction term in this mass balance to account for their generation and/or consumption

$$\boldsymbol{j}_A = -\rho \mathcal{D}_{AB} \boldsymbol{\nabla} \omega_{\mathrm{A}} + \boldsymbol{r}_A \tag{22}$$

where

$$\boldsymbol{r}_A = \nu k \boldsymbol{C}_A \tag{23}$$

within which ν is the stoichiometric coefficient of A, k is the reaction rate constant, and $\boldsymbol{C}_A$ is the distribution of the concentration of A in the control volume.

For a porous medium, porosity and tortuosity must also be considered. Porosity ϵ is defined as the volume fraction of void space to solid space within a porous medium

$$\epsilon = \frac{\mathrm{V_{void}}}{\mathrm{V_{solid}}}. \tag{24}$$

Tortuosity τ captures geometrical transport limitations within the medium due to narrow and winding pores. τ can be back-calculated from experiments that measure the effective diffusivity of the medium but is often selected using correlations that are functions of porosity, such as those developed by Bruggemann (119)

$$\mathrm{T} = \epsilon^{-0.5} \text{ for spheres} \tag{25}$$

$$\mathrm{T} = \epsilon^{-1.0} \text{ for cylinders.} \tag{26}$$

In order to account for these geometric factors in Fick's law, an effective diffusivity $\mathcal{D}_{eff}$ must be used where

$$\frac{\mathrm{D_{eff}}}{\mathrm{D_{AB}}} = \frac{\epsilon}{\tau}. \tag{27}$$

Incorporating ϵ and τ into derivations of Fick's law arrive at the same result.

$$\boldsymbol{j}_A = -\rho \mathcal{D}_{AB} \left(\frac{\epsilon}{\tau}\right) \nabla \boldsymbol{\omega}_{\mathrm{A}} + \boldsymbol{r}_A. \tag{28}$$

Therefore, for transient reactive diffusion in a porous medium, the mass flux through the domain may be expressed as follows

$$\boldsymbol{j}_A = -\rho \mathcal{D}_{eff} \nabla \boldsymbol{\omega}_{\mathrm{A}} + \boldsymbol{r}_A. \tag{29}$$

The equations presented above for describing the specified system assume properties and concentrations are present on a continuum basis. Practically, that means that these calculations would need to be carried out by conducting a mass balance on each voxel of our domain, a time-consuming process for even powerful computational resources.

A more efficient approach is to utilize pore network modelling (120–122). In this approach, image processing is used to identify void spaces within the porous domain. Pores are determined as the largest diameter spheres which may fit within such a void. Pores are connected in a network by throats, which are designated as void spaces between pores, approximated as cylinders with diameters smaller than the smallest diameter pore they are connected to. The diffusion of species in the network is therefore limited not only by the size of the throats, which will always be smaller than that of the pores, but also by the throats themselves as they bottleneck diffusion into each pore. Network bulk properties, including ϵ and ϵ are set to match those of the relevant continuum. Key assumptions include that each pore is well mixed and at constant property and concentration values. Each pore is then used as a node for calculation, greatly reducing the number of computations required, while producing a result that is similar to the ultra-refined continuum approach (123).

The purely diffusive transient single component mass balance for a given pore i in a pore network surrounded by pores j - n is

$$\frac{dC_{A,i}}{dt} = \sum_{j}^{n} g_{ij}\left(C_{A,j} - C_{A,i}\right) \tag{30}$$

where $C_{A,i}$ is the concentration of component A in pore i, $\frac{dC_{A,i}}{dt}$ is the rate of change of concentration of component A in pore i with respect to time, and g_{ij} is the diffusive conductance between pore i and the j^{th} pore.

g_{ij} describes the conductance of a conduit through which mass diffuses between pores in the pore network including ½ of pore i, ½ of pore j, and the cylindrical throat that connects them. As such, g_{ij} contains the sum of the conductances in each of these regions and can be expressed by the following relation by summing conductances in series

$$\frac{1}{g_{ij}} = \frac{1}{g_{pi}} + \frac{1}{g_{T_{i-j}}} + \frac{1}{g_{pj}} \tag{31}$$

where g_{pi} is the conductance in the ½ of pore i, g_{pj} is the conductance in the ½ of pore j, and $g_{T_{i-j}}$ is the conductance in the cylindrical throat that connects them.

Generally, diffusive conductance is defined as

$$g_i = \frac{\mathcal{D}_{AB} A_i}{L_i} \tag{32}$$

where A_I is the cross-sectional area through which component A diffuses and L_i is the length of the segment through which it diffuses. For pores, A_I is the cross-sectional area of the sphere, for throats it is the cross-sectional area of the cylinder. Similarly, for pores L_i is equal to the radius of the sphere while for throats it is equal to the length of the cylinder.

Returning to the overall mass balance around pore i, in the presence of reactions the expression becomes

$$\frac{dC_{A,i}}{dt} = \sum_{j}^{n} g_{ij}\left(C_{A,j} - C_{A,i}\right) + r_{A,i} \tag{33}$$

where $r_{A,i}$ is the rate of reaction of component A in pore i which is expressed similarly to before as

$$r_{A,i} = \nu k C_{A,i} \tag{34}$$

and can represent generation or consumption of species A.

In the context of ROS diffusing into cortical bone and reacting with the collagen matrix to cause oxidative damage, the above expressions describe their diffusion through the porous network and consumption in each pore as they react with the organic phase. Diffusive limitations in the cortical bone porous network would be related to the definition of conductance, meaning that the diffusion of ROS would be limited by diffusivity of ROS in the fluid present in the cortical bone and the size of the bone's pores and throats.

As discussed previously, the capillary pressures expected in cortical bone pores prohibit fluid flow into the tissue, but they do not limit diffusion. For many applications regarding cortical bone, the desire exists to increase mass transfer into the porous network by enhancing this flow and causing convection. In order to do this, many researchers have turned to using solvents with high diffusivity, low viscosity, and high density to accomplish this task. One such fluid, supercritical carbon dioxide, will be discussed in the following section.

2.10 Supercritical carbon dioxide

Matter is typically found in three main phases: solid, liquid, and vapour. The transition between these phases for a given chemical is governed by changes in the thermodynamic properties temperature, pressure, and mass/mole fraction in a given system of study (124). As such, boundaries between phases of matter can be expressed using these properties. The behaviour of a chemical or mixture is represented using equations of state, which relate temperature, pressure, and composition to one another in an effort to define unknown properties of the system. Multiple phases may exist in equilibrium in a given system, each with different compositions at a given temperature and pressure. Once all properties are known, the phase or phases of a system are often confirmed using experimental data found in standard resources including DECHEMA's Chemistry Data Series, Perry's Chemical Engineers Handbook, the CRC Handbook of Chemistry and Physics, National Institute of Standards and Technology (NIST) Chemistry WebBook or other literature sources (125–127).

One key thermodynamic parameter is the critical point, defined as a critical temperature T_c and pressure P_c for a given chemical or mixture. The critical point delineates the limit where liquid and vapour phases are still distinguishable. At the critical point, the specific volume, defined as volume per unit mass or moles for a given species, for the liquid and vapour phases become equal and the two phases become indistinguishable from one another (124). As temperature and pressure are elevated above the critical point, the mixture will become cloudy and then clear again, forming a single supercritical phase. This phase is known as a supercritical fluid.

Supercritical fluids behave differently from other fluids. They possess a unique combination of properties, notably diffusivity and viscosity similar to their corresponding vapour phase and density similar to their corresponding liquid phase. As a result, supercritical fluids flow like vapours but

retain the solvent carrying capacity of liquids, making them exceptional solvents for use in extracting components from deep within porous materials.

A key limit for the application of supercritical fluids is their often prohibitively high critical points. Many chemicals require extremely high pressures and temperatures to surpass their critical points, making containment and safety during their use costly. Carbon dioxide (CO_2) is one chemical which possesses a relatively low critical point ($T_c = 31.1°C, P_c = 73.8\ bar$) making it well suited for industrial applications (128,129). Supercritical CO_2 ($SCCO_2$) is used extensively in industry as an inert green solvent for extraction unit operations including the decaffeination of coffee and lipid extraction, and studied in oil reservoirs and biomedical applications (130–135).

Recent biomedical work with $SCCO_2$ has centred around tissue sterilization processes with specific applications including the destruction of microbes and their spores (136). In the specific context of bone tissue, $SCCO_2$ has been studied as a solvent for virus inactivation, bone delipidation, immunogenicity removal, and tissue sterilization, often with the aim of preparing allografts for implantation in patients and with great success (137–139). This approach has the advantage of avoiding harsh chemicals and radiative treatments, such as nitrogen dioxide or gamma irradiation, which may leave toxic residue or have been shown to reduce bone mechanical properties and fracture toughness, and can lead to poor clinical outcomes (12,140).

Focusing on sterilization in bone tissue, research in this area has sought to determine if $SCCO_2$ treatment has any impact on bone mechanical properties (141). While mechanical characterization in this area has failed to consider fracture mechanics perspectives, which ultimately would have provided insight into the clinical utility of treated allografts, current research using animal specimens has determined that $SCCO_2$ does not have a significant impact on cortical bone mechanical properties (142). Studies of human cancellous bone allografts have generated similar conclusions (143). Industrial equipment exists for $SCCO_2$ tissue sterilization and some tissue banks have adopted this sterilization method, however, concerns over damage caused to soft tissues during the depressurization process have potentially limited the uptake of this technology.

$SCCO_2$ sterilization techniques leverage the vapour-like high diffusivity and low viscosity in combination with liquid-like density of $SCCO_2$ to overcome transport limitations present in tissues and deliver sterilant, typically ROS including H_2O_2 and peracetic acid, deep within their porous structures. This approach also increases the likelihood that sterilant ROS molecules will be distributed

uniformly throughout the tissue's volume as the $SCCO_2$ solvent fills the porous void volume. Despite the utility of this technique for delivering ROS deep within tissues, such as cortical bone, oxidative damage studies in tissue have not been reported in the literature.

Chapter 3
Materials and Methods

This section details the methods and materials used in the process design, pore network modelling, and experimental techniques in the pursuit of designing an *in vitro* model of oxidative damage in cortical bone.

3.1 *In vitro* model process design

3.1.1 *In vitro* model conception

As outlined in the Introduction and Literature Review sections of this thesis, there is a need for the development of an *in vitro* model of oxidative damage. To briefly reiterate, the key objective of this model is to deliver enough reactive oxygen species (ROS) deep into the porous structure of the material such that it can create a uniform oxidative damage profile throughout the volume. This would lead to the elimination of a damage gradient in the domain and, in the case of bone, would more closely mimic *in vivo* processes where cells present in the tissue, notably osteoclasts, osteocytes, and immune cells, are thought to produce damaging ROS *in situ* within the tissue (55,144,145).

Several key design decisions were made in order to attain this goal and are documented in the following sub-sections.

3.1.2 Process type

A batch process was selected by considering available equipment, limited resources, and the size of the specimens to be treated. With regards to specimen size, this thesis focused on cortical bone beams with dimensions 4 x 4 x 50 mm to align with relevant ASTM standards for 3- and 4-point bending fracture testing, however other specimen sizes and geometries could be used (109). The number of specimens that can be treated at a given time depends on the size of both the specimens and the reactor. The chosen batch process is outlined in Figure 3.

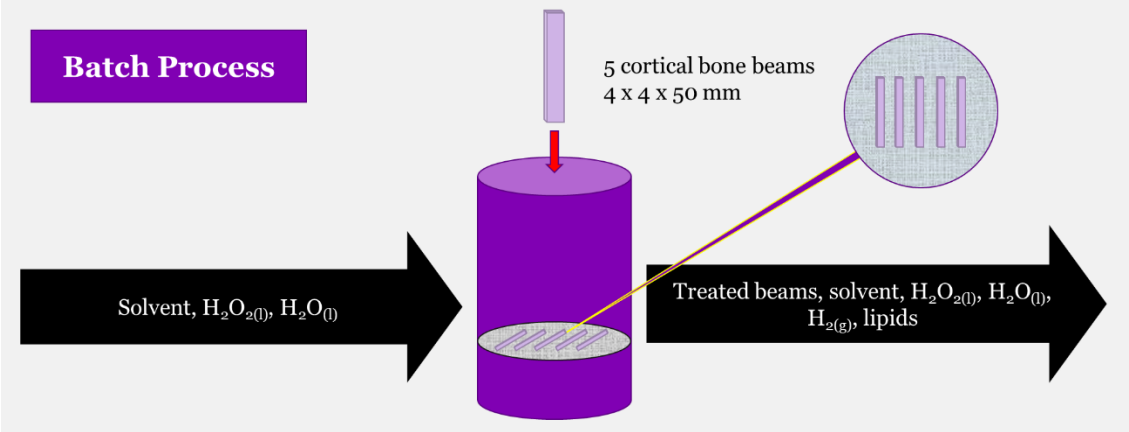

Figure 3 – Block flow schematic for the selected batch process.

While continuous flow processes were considered, issues related to their operation and specimen geometry prevented them from being selected. Specifically, a continuous process was proposed which would utilize a high-pressure liquid chromatography (HPLC) filter tube to house cylindrical bone specimens 2 – 3 mm in diameter. Treatment or control solutions would then be flowed through the bone using a high-pressure HPLC pump. The operation of this process posed a challenge via the high backpressure expected from the bone samples. The dense nature of cortical bone would pose difficulty for fluid flow through its porous network as its small pores, and correspondingly high capillary pressures, would require immense applied pressures to drive fluid flow. Additionally, manufacturing cylindrical cortical bone specimens, while novel, represented another challenge. In order to manufacture such geometries, surgical bone drills suited to this task would have to be utilized to harvest specimens from bovine bones. The rapid rotation of the bore's drill bit and related impact on the bone could induce microcracking, reducing the toughness of the bone artificially. Additional testing would have to be completed using standard rectangular bone beams to determine if this effect existed and was significant. It was therefore deemed simpler to utilize the batch process, which did not have either of these issues and was capable of using bone beams prepared using established harvesting techniques that were potentially less likely to create artificial damage.

3.1.3 Oxidative damage simulation

The selected reactive oxygen species to simulate oxidative stress was hydrogen peroxide (H_2O_2), an ROS present abundantly in the body and capable of being decomposed into toxic free radicals by

physiologically-relevant catalysts, including enzymes such as superoxide dismutase, and metal ions, such as Fe^{2+} and Fe^{3+} (23,37). The selected catalyst was cobalt (II) chloride ($CoCl_2$) for its ability to catalyze the Fenton-like decomposition of H_2O_2 into the toxic hydroxyl radical ($\dot{}OH$) and oxygen (O_2) (35).

1X phosphate buffered saline (PBS) with 1 mM $CaCl_2$ in distilled water was selected as the solvent. PBS provides a pH of 7.4, which is close to the physiological pH within the body that tissues are typically exposed to. This, in tandem with the distilled water, prevents tissues from becoming damaged due to dehydration and excessively low or high pH values. The addition of $CaCl_2$ was done to prevent Ca^{2+} from leaching out of the bone's mineral phase, where it is typically sequestered as part of the hydroxyapatite. The catalyst $CoCl_2$ was also highly soluble in aqueous solutions.

3.2 Pore Network Modelling of bovine bone

In order to inform the amount of time bovine cortical bone specimens should be exposed to controlled levels of ROS to incur oxidative damage uniformly throughout their volume, the very first pore network model of bovine cortical bone was developed using OpenPNM, a Python-based open source software for the analysis of porous media (123). A 1.2 x 1.2 x 0.30 mm representative volume element (RVE) of bovine cortical bone was developed to model a control volume in the centre of the bone beams used in the ROS soak experiment. The placement of this control volume at the centre of the beams was done to mitigate end effects from ROS diffusing into the porous bone on the ends of the beams. The size of the domain was deliberately selected to be less than experimental specimens (4 x 4 x 50 mm) to reduce computational effort and take advantage of geometric symmetry along the axes of the simulated beam. The RVE's dimensions were also selected such that its width and thickness (1.2 mm x 1.2 mm) were at least 100 times the dimensions of the largest geometrical features; the canals' diameter.

The pore network was created to mimic bovine cortical bone, employing Haversian and Volksmann's canals, lacunae, and the solid bone matrix. The canals intersected each other transversely, the Haversian canals oriented axially and the Volksmann's transversely. Canal diameter was set as 28 μm and they were spaced 300 μm apart in a regular lattice structure. Lacunae diameter was set as 7 μm and their diffusive conductance was assumed to be 10 times higher than that of the solid matrix.

Diameters and spacing were reported as the average of three values measured using ImageJ to analyze the images in the cited literature (83,84,101).

The overall network porosity was set to 10%. The solid matrix was modelled as a continuum using the uniformly sized smallest diameter pores with an assigned tortuosity of 5.0 to reduce their diffusive conductance by 50x when compared to the void space in the porous network. Tortuosity of 5.0 was arbitrarily assigned due to the scarcity of tortuosity values and correlations in the literature for bovine cortical bone and similar materials. Diameter and porosity values were selected in line with literature on bovine cortical bone morphology, although it should be noted that the overall porosity was selected to be slightly larger than literature values (83,84,101). Due to the scarcity of information available for bovine cortical bone, tortuosity was arbitrarily set to 5.0 based on typical settings for similar porous materials.

Network generation was accomplished in a Python script by first creating two two-dimensional images of the canals in the x and y axes. These two images were then overlayed on top of each other to create a lattice of perpendicular Volkmann's canals in the x- and y-directions. Haversian canals were then added in the z-axis to create a 3D image (Figure 4). Each voxel was set to 4 μm^3.

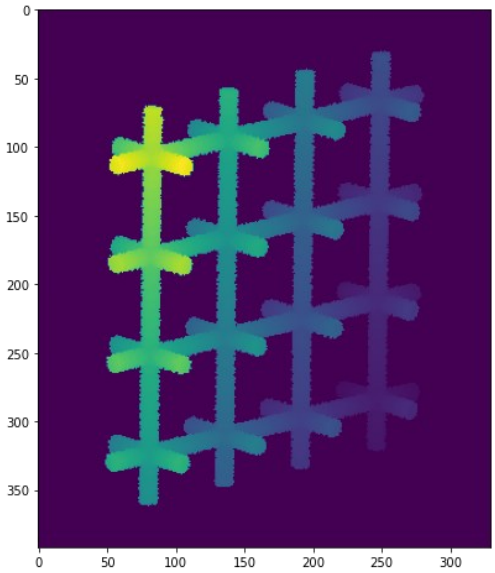

Figure 4 – Preliminary 3D lattice of canals step in pore network generation.

Using OpenPNM's porous network generation algorithms, spherical pores 28 μm in diameter were inserted with overlap along each of the canals with overlap to create these cylindrical features. Following canal creation, OpenPNM's snow_hybrid algorithm was used to insert pores 7 μm in diameter into the void space between the canals to make the solid matrix. Among these pores, lacunae were defined based on their differing conductance values to reach a lacunae volume fraction of 0.003. The final geometry was saved as a .pkl file to retain that particular geometry to run all simulations on. The final geometry rendered in Paraview is shown in Figure 5 and Figure 6.

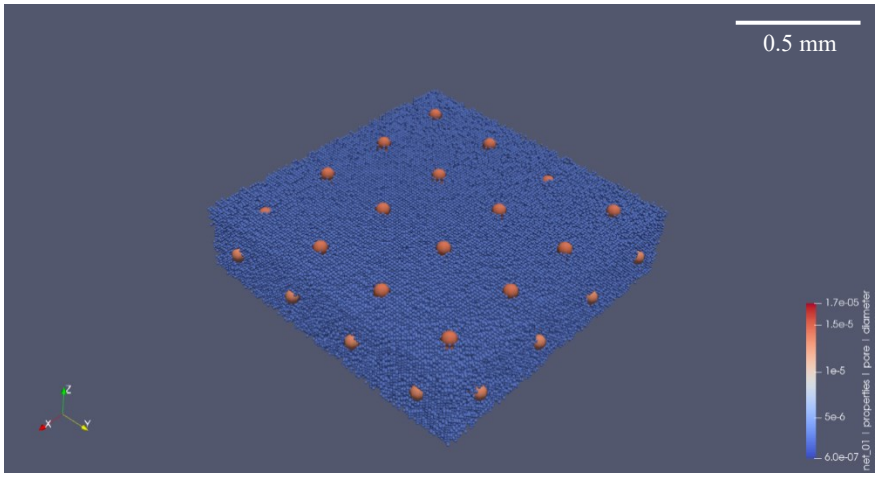

Figure 5 – Final rendered geometry visualized in Paraview. Entire domain shown.

The transient reactive diffusion simulations in this porous network were run using the generated network in a separate Python script. Key underlying assumptions in this model include Fickian equimolar counter-diffusion, dilute solutions, no fluid flow within the porous media due to an insignificant pressure gradient across the sample thickness and prohibitively high capillary pressures, the presence of solution throughout the medium initially, only H_2O_2 diffuses into the specimen, and the diffusivity of H_2O_2 in the medium is more influential on diffusion than pore size. Additionally, it was assumed that the system was single-phase liquid, which ignored the impedances to diffusion and reaction caused by gas formation within the network. This was done to simplify the calculations in OpenPNM. $H_2O_{(l)}$ was selected as the solvent for this system to match the aqueous bone soak experiment taking place in the laboratory.

The reaction of the $^{\cdot}OH$ and other free radicals with the bone matrix or organic phase, should it indeed occur, was reported to occur extremely quickly ($k = 10^5 - 10^{10}\ M^{-1}s^{-1}$) making it impractical to capture this using the pore network modelling simulation due to the extremely small timescales (45). The rate-limiting step of the Haber-Weiss reaction pathway, the free radical generation step, the decomposition of H_2O_2 catalyzed by transition metal ions, was selected instead

$$H_2O_2 + M^{n+} \rightarrow {}^{\cdot}OH + OH^- + M^{(n+1)+}$$

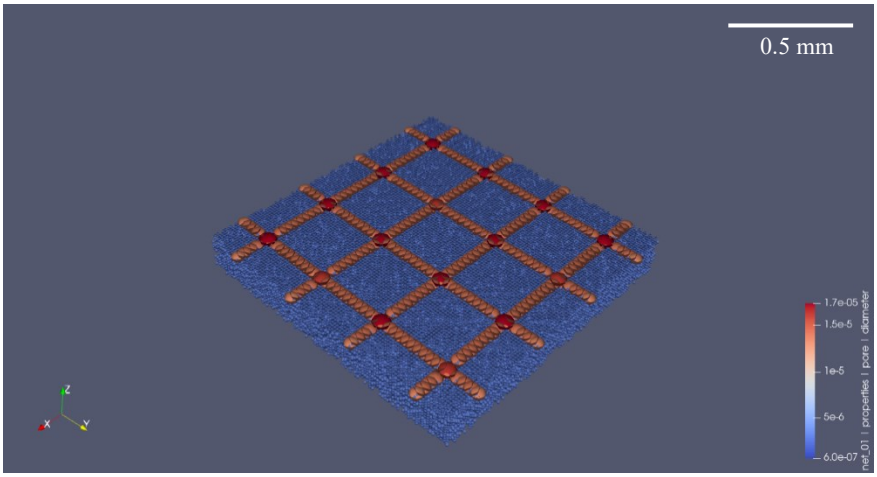

Figure 6 – Final rendered geometry visualized in Paraview. Cross-section taken halfway through z-domain to show canals within the matrix.

where the presence of M^{n+} in solution was assumed to have no effect on the diffusion of H_2O_2 and was assumed to be in excess of reactants. The reaction was assumed to occur solely within the solid matrix. As the conductance in the void space was set to be 50x higher in magnitude than in the mineralized bone matrix, it was also assumed that there was no radial concentration gradient within the canals. The entered chemical kinetics were for a second order reaction to capture the rate-limiting step within the Haber-Weiss pathway with $k = 0.13\ M^{-1}s^{-1}$ (44). Simply

$$r_A = -k[H_2O_2]^2. \tag{35}$$

The reaction constant was studied parametrically by first decreasing it initially by several orders of magnitude to match the reaction and diffusion timescales, and then decreased by 1 – 10 orders of magnitude to study the behaviour of the system as k varied.

Conceptually, the model was formulated based on the path of a H_2O_2 may take from the outside of the bone's porous network to where it reaches the collagen, decomposes into free radicals, and reacts with collagen molecules, as outlined in Figure 7. Initially, the H_2O_2 molecule would diffuse through the void space of the porous network, starting with the larger Haversian and Volkmann's canals. Following the canals, the H_2O_2 would diffuse through the smaller void pores, specifically the lacunae and canaliculi. Next, the H_2O_2 would diffuse through the solid bone matrix, passing through the extremely small spaces between the mineralized collagen fibers. Finally, upon arriving at the collagen

molecules, the H_2O_2 would decompose into $^{\cdot}OH$, which is capable of in turn reacting and producing $^{\cdot}O_2^-$, which would both react with the collagen molecules. The reason this decomposition must take place at the collagen molecules is due to the free radicals' extremely high reactivity, making these species extremely short lived and likely to only react with other molecules in their immediate vicinity.

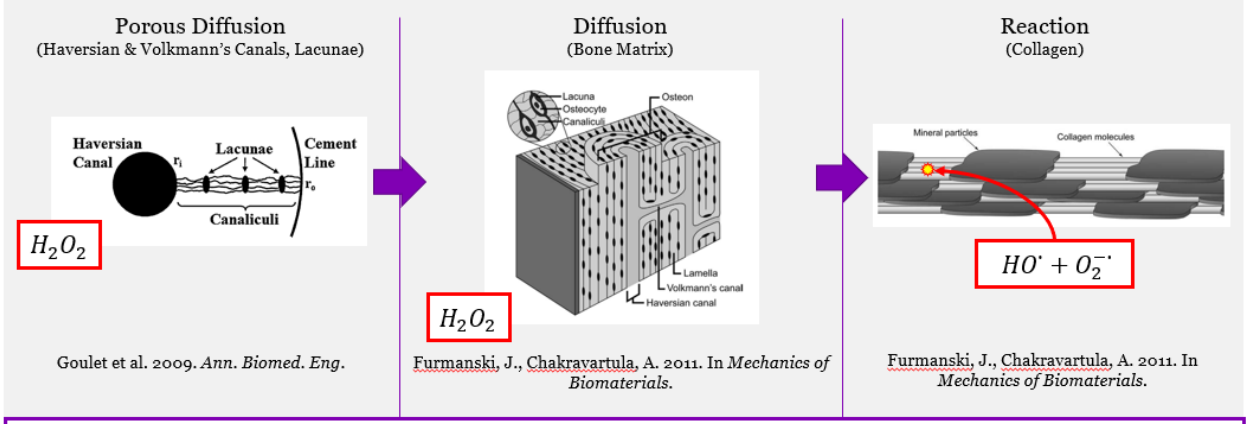

Figure 7 – Conceptual formulation of the path taken by hydrogen peroxide molecules before decomposing into free radicals which react with bone collagen. Goulet et al. figure reprinted by permission from Springer Nature Customer Service Centre GmbH: Springer Nature Annals of Biomedical Engineering (Poroelastic evaluation of fluid movement through the lacunocanalicular system, Goulet, G.C., et al) © Springer Nature 2009. Furmanski, J, and Chakravartula, A., figures reproduced with permission of The Licensor through PLSclear from Furmanski, J., Chakravartula, A. Mechanics of Biomaterials Fundamental Principles for Implant Design © L. A. Pruitt and A. M. Chakravartula 2011.

Temperature was fixed at 25°C for the system. Other input properties for the two-component $H_2O_2 - H_2O$ system are summarized in Table 1. It should be noted that due to the scarcity of data available for varying concentrations of H_2O_2 in aqueous solutions, 30% (w/w) was selected for gathering information.

Boundary conditions, as per the placement of the control volume within the full bone beam, were applied to all of the pores connected to the faces normal to the x and y axes. Boundary concentrations varied from 0.544 – 0.136 $\frac{mol}{L}$ and values can be found in Table 2. These conditions were selected to match those utilized in the ROS soak experiment, which were created by serial dilution. All faces without explicit boundary conditions had no-flux boundary conditions implicitly imposed.

In order to relate this analysis more closely to the experimental specimen, two simulations were undertaken, the first with boundary conditions applied on all four edges of the 1.2 x 1.2 x 0.30 mm RVE and the second with boundary conditions only applied on two of the network's edges. Using the RVE's symmetry, this second simulation was used to mimic a quarter of a 2.4 x 2.4 x 0.30 mm RVE, effectively scaling up the simulated network four-fold.

Table 1 – Properties input for the simulated aqueous hydrogen peroxide mixture.

Property	**Value**	**Source**
Boiling point for 30% (w/w) $H_2O_{2(aq)}$	379.5019348 K	(146) linear interpolation in Table 19 (pg. 230)
Critical temperature for 30% (w/w) $H_2O_{2(aq)}$	730.15 K	(147)
Critical pressure for 30% (w/w) $H_2O_{2(aq)}$	$20.99 * 10^6$ Pa	(147)
Diffusivity of $H_2O_{2(l)}$ in $H_2O_{(l)}$ at 25°C	$1.19212963 * 10^{-9} m^2 s^{-1}$	(146) from Table 13 (pg. 209)
Molecular weight H_2O_2	$34.0147 * 10^{-3}\ kg\ mol^{-1}$	(147)

Table 2 – Boundary conditions applied in all pores on the faces normal to the x and y axes during transient reactive diffusion simulations

Boundary Condition	**Concentration of H_2O_2 % (w/w)**	**Concentration of H_2O_2 (mol/L)**
BC1	1.667	0.544
BC2	0.833	0.272
BC3	0.417	0.136

Initial conditions specified the presence of the boundary conditions on the four RVE edge faces and the complete absence of H_2O_2 everywhere else within the control volume and on the remaining two RVE faces ($[H_2O_2] = 0\,\frac{mol}{L}$).

In order to monitor concentration quantitatively within the porous network over time, a surveillance pore was selected in the matrix phase near the centre of the domain which was located approximately equidistantly from all nearby canals. The concentration in this pore was reported over time for all simulations. In the 1.2 x 1.2 x 0.30 mm^3 network, the surveillance pore was located in the approximate centre of the slice. In the 2.4 x 2.4 x 0.30 mm^3 network, this surveillance pore was located near the RVE's corner at $(x,y) = (1.2\ mm, 1.2\ mm)$, which would be the centre of a slice 2.4 x 2.4 x 0.30 mm^3 in size. Time to steady state was determined as the time when the surveillance pore concentration reached 95% of its final value. Simulation results were also visualized in Paraview to capture the H_2O_2 concentration gradient spatially throughout the domain.

3.3 Harvesting cortical bone beams from bovine tibiae

Bovine cortical bone beams were harvested from four bovine tibiae obtained from local abattoirs in the Kitchener-Waterloo area. Due to variations in geometry and size of tibiae, 3 usable beams were harvested from the first tibia, 6 from the second, 9 from the third, and 6 from the fourth. Steers were between 18 – 24 months old. Tibiae were received frozen, and any remaining flesh was removed while they defrosted. Diaphyses were isolated using a 14-inch woodworking band saw (Craftex CX104, Busy Bee Tools, Concord, ON) to remove the ends of each long bone. Diaphyses were then sliced in half in the frontal (coronal) plane to separate the anterior and posterior sections. Both diaphysis sections were frozen at $-20°C$ until beam cutting.

After defrosting each diaphysis for 1 hour at room temperature, bone marrow was removed from both portions and discarded as biowaste. All bone beams were harvested from the posterior diaphysis portion. The curved edges of the posterior diaphysis were removed using a pathology band saw with distilled water-cooled diamond abrasion blade (IMEB, San Marcos, CA). The remaining posterior diaphysis was further flattened using a CNC Mini Mill (Sherline, Vista, CA) in combination with a ShopVac to collect bone dust created due to the dry cutting. Once both the endosteal and periosteal sides were flattened and the thickness of this section was less than 6 mm thick, the diaphysis portion was taken back to the pathology band saw and beams 4.5 x 4.5 x 50 mm were cut. Each beam was

labelled using the notation BT-PX-YY in permanent marker, where X represented the order it was cut from the diaphysis and YY indicated the particular bovine tibia they were harvested from. These beams were frozen again at $-20°C$. Throughout the bone cutting process, the endosteum was marked.

To achieve the final desired beam dimensions of ($4\ x\ 4\ x\ 50 \pm\ 0.1\ mm$) to be in line with ASTM standards for fracture testing materials in 4- or 3-point bending, beams were ground and polished using sandpaper. Prior to polishing, beams were defrosted for 1 hour at room temperature. Initial dimensions of each beam were measured and recorded. Starting with the width dimension, beams were polished to $4 \pm 0.1\ mm$ using 45 μm grit. The rougher of the two faces was polished first. Beams were held down on the sandpaper with a moderate amount of pressure and rotated in a circular motion in multiples of 25. The opposite face was polished as needed to remove any surface irregularities and ensure smooth flat faces with constant width along the beam's length. Once a width of approximately 4.30 mm was reached, the beam was then polished using 15 μm sandpaper, repeating the above procedure. Similarly, once approximately 4.15 mm in width was reached, the 9 μm sandpaper was used, and the above method was repeated until the width is $4.0 \pm 0.1\ mm$. Both faces were polished with the 9 μm sandpaper to ensure constant surface roughness for the entire bone beam specimen, which may be important for diffusion effects during the beam soaking experiment, however some modelling results indicate that this surface roughness does not impact transport-related diffusion based on concentration gradients (148). The above procedure was repeated for the thickness and length dimensions with the same tolerances. Beam cross sections were kept as square as possible and the endosteum was tracked throughout the polishing process. Once polished and acceptable dimensions were reached beams were wrapped in gauze soaked in 1X PBS with 1 $mM\ CaCl_2$ in a 15 mL Falcon tube and refrozen at -20$°C$.

3.4 Reactive oxygen species soak experiment

This technique was developed as a first-of-its-kind method for damaging bone tissues using controlled levels of physiologically-relevant ROS generated *in situ*.

Prior to the start of the experiment, specimens were randomly distributed between all treatment and control groups ensuring that specimens from each bovine tibia were matched, meaning each tibia would have specimens in all experimental groups.

Previously harvested and frozen cortical bone beams were defrosted at room temperature in 1X phosphate buffered saline (PBS) with 1 mM $CaCl_2$ for 4 hours. Thawing was done to remove any patches of ice or areas of low temperature that may impede diffusion of catalyst in the sample.

Once fully rehydrated, all but one of the bone specimens in a given batch were immersed in 10 mL of 0.1 M cobalt (II) chloride ($CoCl_2$) dissolved in 1X PBS with 1 mM $CaCl_2$ (Ca^{2+}) in a 15 mL Falcon tube for 24 hours (38). The amount of $CoCl_2 * 6H_2O$ added for a 0.1 M solution of 10 mL was 0.238 g. If instead anhydrous $CoCl_2$ was used, the amount added was 0.130 g. Both compounds were highly soluble in the aqueous solution. The remaining single bone specimen was soaked in 10 mL of pure 1X PBS with 1 mM $CaCl_2$ as a no catalyst control.

Each solution was required to have a pH of 7.40 ± 0.10 to avoid accidentally demineralizing the bone (acidic) or demineralizing the bone and damaging the organic matrix (basic). In the acidic case, an unidentified white precipitate forms during the catalyst perfusion step. For the no catalyst control, 1X PBS with 1 mM $CaCl_2$ was naturally near that value. For the other solutions, 2.0 M aqueous $NaOH$ was added one drop at a time to increase the pH to 7.40 ± 0.10. For an approx. pH 5.30 solution of $CoCl_2$ in 1X PBS with 0.1 mM $CaCl_2$, this was approximately 6 drops. The $Co^{2+}_{(aq)}$ will catalyze the decomposition of H_2O_2 into hydroxyl radicals and ions via the Haber-Weiss reaction, which was expected to subsequently react with the bone's collagen, thereby inducing oxidative damage (38).

The $CoCl_2$ reaction with H_2O_2 has been observed to be quite vigorous at similar concentrations used in other experiments by our collaborators, therefore it was important to first perfuse the bone sample with $Co^{2+}_{(aq)}$ so that the catalyst was evenly distributed within its matrix and the rate of reaction during the subsequent soak in H_2O_2 solution could be slowed. This also matches our pore network modelling assumption regarding initial catalyst distribution.

Approximately 1 hour before the 24h catalyst perfusion phase was complete, the dilute H_2O_2 treatment solutions were prepared for beam soaking via the serial dilution of a 30% w/w stock aqueous H_2O_2 solution and 1X PBS with 1 mM $CaCl_2$ (Ca^{2+}). Serial dilutions were conducted in 50 mL Falcon tubes in a fume hood and are presented in Table 3. The utilized dilute concentrations of H_2O_2 were based on those seen in existing commercial tissue sterilization protocols, which were the only available references, and then increased further to be more conducive to causing oxidative damage (141). 10 mL of each solution was transferred to a 15 mL Falcon tube. 10 mL of 1X PBS

with 1 mM $CaCl_2$ were utilized as the negative controls (one for catalyst and one for H_2O_2). Bone beams were removed from the catalyst perfusion solution and gently dried using Kimwipes to prevent any excess catalyst carryover into the reaction solutions. Once bone beams were placed in solution, the Falcon tubes were left in the fume hood on a tube rack, lids removed, and their openings were covered by excised nitrile glove fingers with the tips clipped to allow venting of evolved O_2 gas.

Table 3 – Serial dilution table for the preparation of dilute hydrogen peroxide solutions for bone treatment. n = 2 for each treatment group (0.544 mol/L, 0.272 mol/L, and 0.136 mol/L).

Starting H_2O_2 Solution	**Volume of starting H_2O_2 solution (mL)**	**Volume of PBS (mL)**	**Final volume of dilution (mL)**	**Concentration of dilution % (w/w)**	**Concentration of dilution (mol/L)**	**Name of dilution**
Stock	2.00	18.0	20.0	3.333	1.088	**S-1**
S-1	10.0	10.0	20.0	1.667	0.544	**S1**
S1	10.0	10.0	20.0	0.833	0.272	**S2**
S2	10.0	10.0	20.0	0.417	0.136	**S3**

Bones were left to soak for 96 hours (4 days) total. The H_2O_2 or PBS solutions were changed for all specimens when gas evolution ceased in the highest concentration (S1) treatment group. This was done to ensure that the reaction continued for the entire treatment period, as it was noted that the highest concentration treatment group ceased gas evolution last. A constant supply of H_2O_2 throughout the treatment period was required to match the pore network model, which assumed an infinite supply of H_2O_2 throughout all simulations.

Evolved gas was oxygen produced via the Fenton-like decomposition of H_2O_2 as it reacted with Co^{2+} and offered a visible indicator of when all H_2O_2 in the solution had been consumed. Fresh solution was prepared in clean 15 mL Falcon tubes no earlier than 1 hour before their use. Bone beams were

gently dried with Kimwipes before being transferred from exhausted to fresh reaction solution to avoid any liquid carryover that may impact species concentrations in the fresh solution. This also ensured that the only catalyst present within each reaction solution was that which had been perfused into the bone's porous matrix during the earlier catalyst perfusion step. The fume hood light was left off during the experiment unless visually inspecting the tubes as a means to save electricity in the laboratory and is noted here for completeness. All steps of the experiment occurred at ambient laboratory temperature (22 – 28°C).

After the 96 hours elapsed, bone beams were removed from their treatment/control solutions and placed into labelled 15 mL Falcon Tubes with 10 mL of pure PBS with 1 mM $CaCl_2$ and stored at $4°C$.

3.5 Negative Controls of oxidative damage

Two negative controls were run. The negative control for oxidative damage was a run of the ROS soak experiment in the absence of H_2O_2 ($[H_2O_2]$ = 0 M). Bone beams (n = 2) were perfused with 0.1 M cobalt (II) chloride ($CoCl_2$) and soaked for the same amount of time as treated beams, but the soaking experiment took place in pure 1X PBS with 1 mM $CaCl_2$ (Ca^{2+}). The negative control for any catalyst effects on the bone beams were run in the absence of catalyst ($[CoCl_2 = 0\ M]$ in the perfusion step and the absence of H_2O_2 ($[H_2O_2] = 0\ M$) in the soak step (n = 3). Specimens were matched with those from other treatment groups to ensure that specimens from each bovine tibia were present in all treatment groups.

3.6 Positive Controls of oxidative damage

The primary positive control of oxidative damage (n = 3) was 25 kGy of gamma radiation, a standard radiation dose bone tissues may be exposed to during sterilization prior to implantation into the body and for which bone fragility effects have been characterized (12). This was performed over 5 days by Dr. Cheol Jeong at the University of Toronto's Southern Ontario Centre for Atmospheric Aerosol Research. Specimens were matched with those from other treatment groups to ensure that specimens from each bovine tibia were present in all treatment groups.

3.7 Fracture Testing

Prior to fracture testing, bones were defrosted for 4 hours in 1X PBS with 1 mM $CaCl_2$ at room temperature. Once defrosted, bones were chevron notched using a custom jig attached to a Buehler Isomet Metallurgical Saw. Notches 0.30 mm thick were cut to a depth of 1.9 mm, as shown in Figure 8, and oriented according to the endosteum to produce circumferential fracture. Chevron notching was done to encourage stable tearing of the tissue, specifically the embedded collagen matrix, during beam fracture. Due to the 4 x 4 mm beam cross-section, the chevron notching did not strictly conform to the ASTM C1421-18 standard.

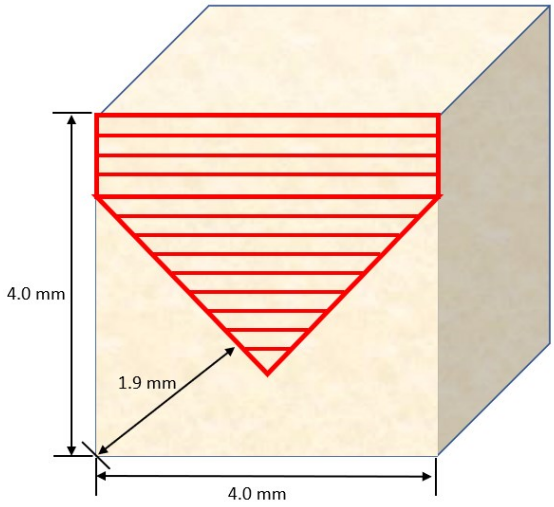

Figure 8 – Dimensions and orientation of chevron notch cutting.

Fracture testing was done in 4-point bending on a Psylotech μTS mechanical testing machine (Psylotech, Evanston, IL). 4-point bending was done to remain in line with ASTM C1421-18 (109). The inner and outer span were 26 mm and 40 mm, respectively. The 4-point bending test configuration was selected over 3-point bending due to its additional advantage of a constant bending moment over the inner span of the specimen, which may better support straight crack growth and stable tearing already encouraged by the chevron notch.

Force, displacement, and time data were gathered from each beam's test. Peak load, P_{max} , was taken as the maximum load reached during testing and normalized to specimen fracture surface area. Work-to-fracture, W_f , was taken as the area under the curve in each beam's force-displacement plot calculated using the trapezoid rule and normalized to specimen fracture surface area. Fracture toughness K_{Ivb} was determined using P_{max} and geometrical data for the chevron notch and sample cross-section according to the procedure for geometry D subjected to 4-point bending outlined in ASTM C1421-18 (109). As an additional criterion from this standard, only specimens that exhibited stable tearing were used for this calculation.

All beam fracture surfaces were imaged using a USB digital microscope (40 to 1000x Magnification Endoscope 8 LED USB 2.0, Jiusion, Amazon) and a transparent millimetre-marked ruler for scale. Chevron notch areas and dimensions were measured in ImageJ.

3.8 Biochemical and Fluorescent Sample Characterization

3.8.1 Beam portioning

Beams were portioned using a low-speed metallurgical saw (Buehler, Lake Bluff, IL) following fracture testing according to Figure 9. Specifics on what each portion was used for are described in the coming characterization sections. HIT and fracture surfaces were preserved for future analysis outside of the scope of this thesis. All portions were stored in micro-centrifuge and Falcon tubes in 1X PBS with 1 $mM\ CaCl_2$ at 4°C.

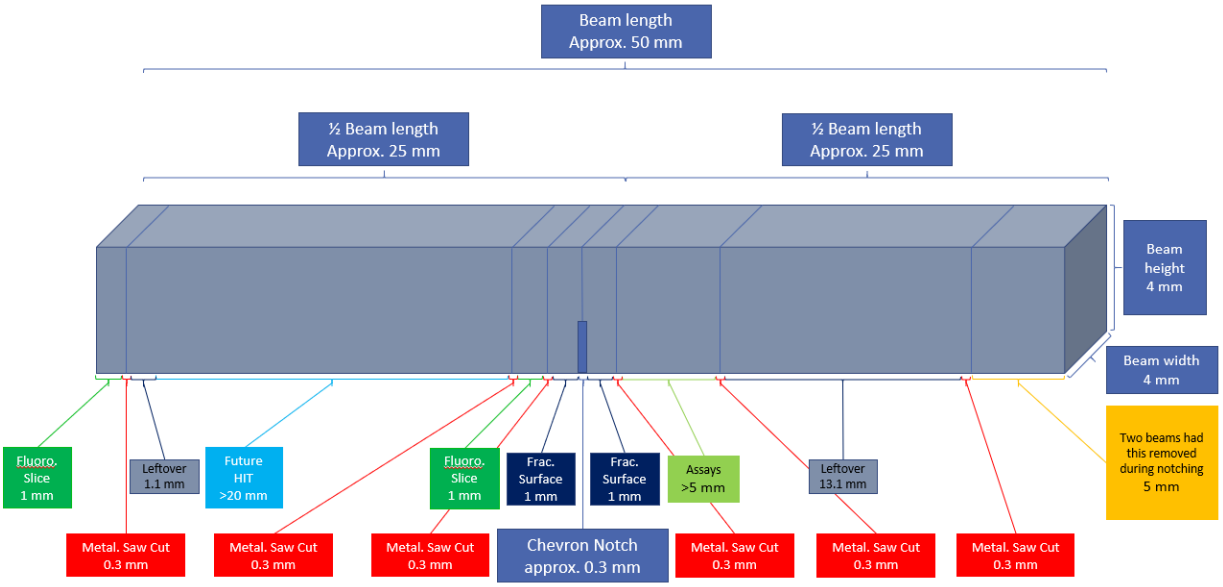

Figure 9 – Schematic depicting how cortical bone beams were portioned following fracture testing. Abbreviations - Fluoro.: Fluorescent Imaging, Metal.: metallurigal, Frac.: Fracture, HIT: hydrothermal isometric tensile testing, Assays: hydroxyproline and carbonyl assays.

3.8.2 Bone slice surface demineralization

Fluorescent microscopy slices from the middle of each beam were demineralized using ethylenediaminetetraacetic acid (EDTA), an irreversible calcium chelator. EDTA binds with calcium in the bone's mineral phase, removing it gradually over time. In order to supply EDTA in large excess and avoid prematurely stalling the chelation reaction, samples were soaked in a volume of EDTA 50x the volume of the sample. Agitation was continued throughout demineralization using tube rocker (VWR, Mississauga, ON).

Bone beam slices approx. 1 mm in thickness were demineralized for 24 hours to demineralize their surfaces for microsopy. Slices were placed into 2 mL microcentrifuge tubes and immersed in 1.5 mL of EDTA.

3.8.3 Fluorescein 5-thiosemicarbazide (FTC) surface staining of slice surfaces for carbonyls

The method described here for staining demineralized bone slice surfaces was formulated by modifying an assay protocol for protein carbonyls used as a standard operating procedure in the Waterloo Composite Biomaterial Systems Laboratory (149). To the author's knowledge it is the first of its kind for staining carbonyls in biological tissues.

Following surface demineralization, bone slices near the centre of each beam were incubated in 1 mL of 5 μM FTC solvated in 50% (v/v) DMSO and distilled H_2O in 1X PBS with 1 mM $CaCl_2$ overnight (approx. 16 hours) at room temperature in microcentrifuge tubes protected from light with aluminum foil and continuously agitated using a rocker (VWR, Mississauga, ON). Following incubation, slices were rinsed 5 times with wash acetone to remove any excess free fluorophore. Number of rinses was determined from a preliminary experiment in which a constant mean pixel intensity was observed in specimens after 5 acetone washes. Slices were then placed in 1X PBS with 1 mM $CaCl_2$ and protected from light for immediate fluorescent microscopic imaging. Samples were stored at 4°C as required before being mounted on glass microscopy slides.

3.8.4 Fluorescence microscopy for damage gradient imaging

Fluorescent imaging was done using a laser scanning confocal microscope (Leica SP5, Leica, Concord, ON) with argon laser. Emission was set to 488 nm, approximately the maximum emission wavelength for FTC 485 nm. Images were taken using the attached CCD camera, a built in FITC filter, which is well suited to image capture here as FITC contains FTC as its fluorescent group, gain set to 561.2, 400 Hz scan speed, 10x objective lens, and default pinhole setting 1 airy.

Bone slice sample dimensions exceeded the microscope's field of view and tiling was conducted to capture the entire specimen surface and z-stacks 459.9 μm in depth were taken at each tile to capture surface features in focus. All images, including stitched and compiled images of entire specimens, were saved as a .lif series for later analysis in ImageJ.

Throughout imaging, exposure time of samples to laser light was minimized when not actively imaging to avoid bleaching the samples.

3.8.5 Fluorescent image processing in ImageJ to analyze damage gradient

Fluorescent microscopy images for each treatment group (n = 1) were imported into ImageJ for analysis. Images were compiled by projecting the slices in the axis perpendicular to the image plane (the z-axis) onto one another using ImageJ's Z-Project tool while retaining the maximum intensity value for each pixel. The underlying assumption is that because the object being imaged was a surface (as opposed to a 3D image such as in an MRI scan) the depth where each pixel is the most in focus is the same depth where it has its highest intensity value. In the case of 3D objects, maximum intensity would provide different images based on the subject of the image, such as in the MRI example shown in (150) where selecting for maximum intensity produces an image of a patient's face, while other selections allow for images to be created of their skull and brain.

In practice, first the total z-stack depth and the depth at which each image in the stack was taken were noted from the metadata for each image set. The height of each slice was preferred to be greater than or equal to the microscope's depth of field, 11 μm in this case. If slices were less than 11 μm in depth, a new stack was compiled from existing stack images by using the "slice keeper" tool to retain only slices that would be 11 μm apart. The rationale for matching or exceeding the microscope's depth of field was to avoid including the same information (pixel intensity value) more than once in

the entire z-projection. Retaining these values would lead to artificially higher intensity values for each pixel in the z-projection due to including the same data more than once in the compilation.

Following compilation of all slices into a single image, each image was saved as a .jpeg file and the colour channels were split to isolate only the green fluorescent signal from FTC. These confocal images were single channel green, and therefore all of the pixel intensity in the green-coloured image was transferred to the greyscale image. Using ImageJ's polygon selection tool, the surface of each sample was segmented from the image background and major artifacts were removed. Mean pixel intensity was calculated using the segmented area and a smaller rectangular region of interest near each sample's centre. Histogram plots indicating the distribution of pixel intensity values and the number of pixels at each intensity within the segmented image were created for each sample. The area under each distribution curve was calculated using the trapezoid rule.

A threshold was established using the no-catalyst negative control image by removing 99.5% of the image's pixel intensity. In practice this required removing all signal from pixels with intensity values less than 220. This same threshold was then applied to all other images to adjust their pixel intensity values relative to this control. As the no-catalyst negative control was healthy bovine cortical bone, not subjected to any form of treatment which may have caused oxidative damage, this threshold also captured autofluorescence and noise naturally present in the bovine cortical bone samples.

3.9 Statistical Analysis

One-way ANOVA (fixed effects, single factor model) was utilized for determining if statistically significant differences existed between means in each group (n = 2). Significance was assigned at the $\alpha = 0.05$ level. An underlying assumption in this analysis was that the data were normally distributed.

Linear regression analysis was conducted in Excel on a linear line of best fit relating hydrogen peroxide concentration to work to fracture, fracture toughness, and maximum displacement. The equation of the linear line of best fit, R^2, and P-values were determined to gauge the strength of each regression. Significance was assigned at the $\alpha = 0.05$ level. P-values were determined using a one-way ANOVA (n = 2) based on the calculated F statistic. Normality was assessed using normal probability plots. In order to adhere to normality, the 0 mM no-catalyst negative control group was excluded from this analysis. The gamma irradiated positive control group was also excluded on account of not being treated with hydrogen peroxide.

Chapter 4
Results and Discussion

4.1 Pore network modelling

This section details results and discussion for the pore network modelling of the reactive oxygen species experiment, the first application of this modelling technique to reactive transient diffusion in bone tissue. Simulations were conducted on both 1.2 x 1.2 x 0.30 mm^3 and 2.4 x 2.4 x 0.30 mm^3 networks to determine time to steady state and transient diffusion concentration gradients of H_2O_2. Results of a sensitivity analysis on the reaction rate constant k are also presented.

4.1.1 - 1.2 x 1.2 x 0.30 mm^3 network

4.1.1.1 Time to steady state

Time to steady state was examined at all boundary condition levels both with (Figure 10) and without (Figure 11) and the reactions active.

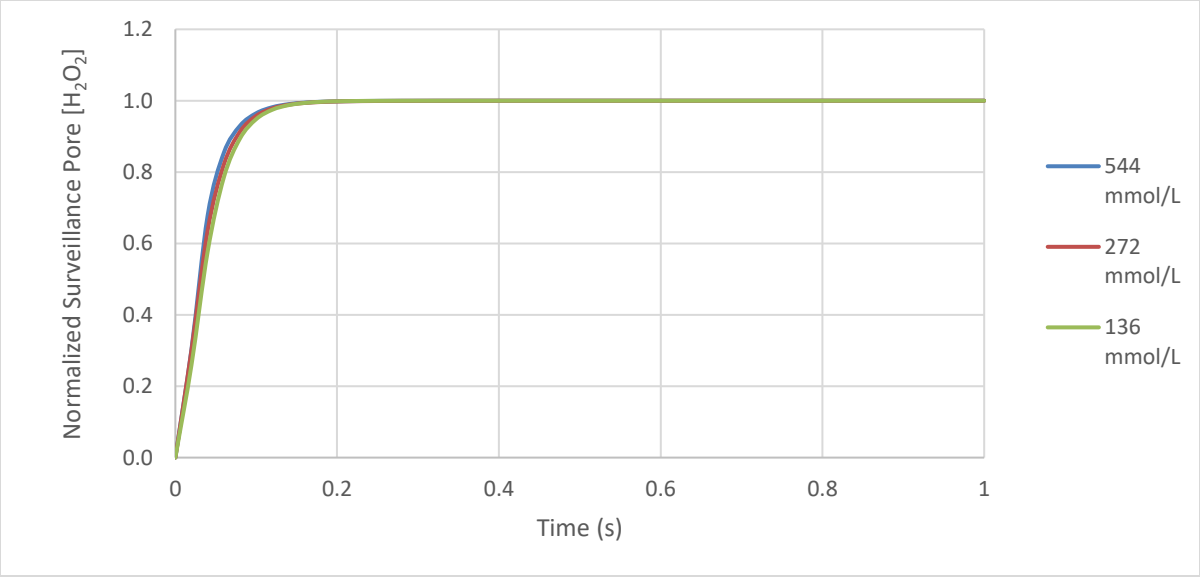

Figure 10 – Normalized surveillance pore hydrogen peroxide concentration over time at each boundary condition with active reactions.

The time to steady state for the nonreactive system was 19 – 21 seconds at each boundary condition. This result helps to validate that the physics in the pore network model were performing as expected. As the boundary concentration changes, the time to steady state should still remain the same for the same network and properties due to the balancing effects of concentration gradient and amount of material to diffuse. For example, as the boundary concentration increases, the driving force for molecular diffusion increases, however, so does the number of molecules that need to diffuse. The higher number of molecules causes a bottleneck effect, limiting the number that can diffuse into the porous network at any given time. This effect counters that of the increased diffusive driving force, leading to the same time to steady state for the system, despite increasing concentrations.

The time to steady state for the reactive system varied from 0.10 – 0.12 seconds across all boundary conditions. This is nearly an order of magnitude faster than the nonreactive system, indicating that when reactions are active, the system reaches steady state much more quickly. The small range of time to steady state values across all boundary conditions indicates that the same balance between diffusive driving force and number of diffusing molecules is in effect as in the nonreactive system, however with less of an exact balance. Overall, this result affirms that the reactive system's diffusive mechanics functioned as expected.

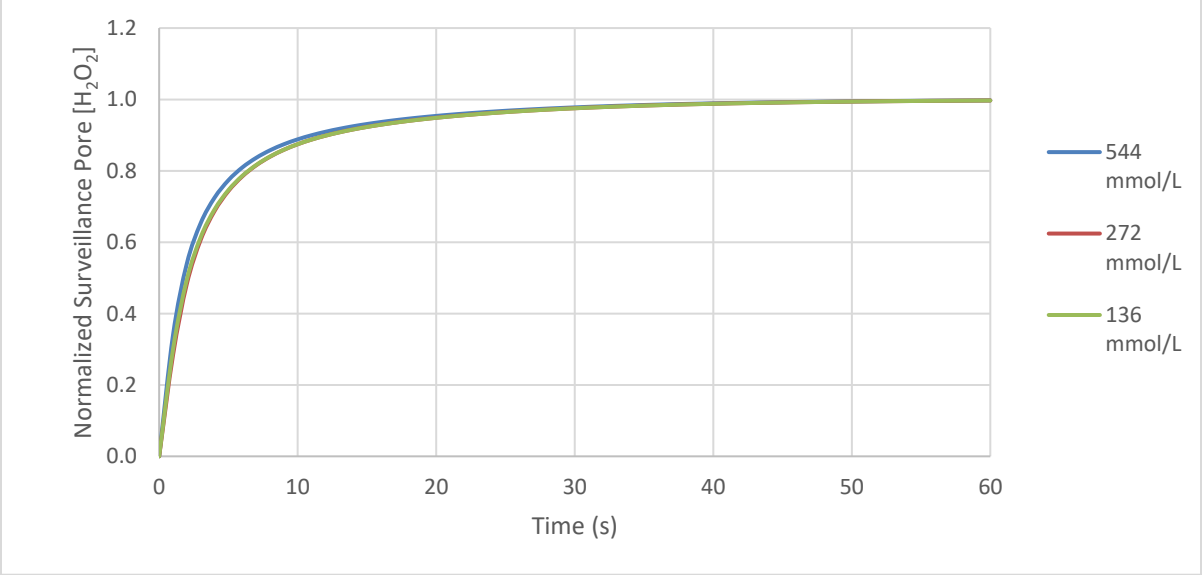

Figure 11 – Normalized surveillance pore hydrogen peroxide concentration over time at each boundary condition without active reactions.

In the context of operating the *in vitro* model's reactor, the modelled time to steady state indicates the theoretical amount of time that bone specimens are required to be exposed to each level of ROS to for them to internally reach the steady state ROS concentrations within their porous internal structure. It does not indicate what that concentration is or if it will be enough to oxidatively damage the bone. Due to the extremely short time to steady state for the reactive system, even shorter than the nonreactive system, it can be posited that the ROS may be reacting and not penetrating deeply into the matrix. The analysis of the simulated concentration profile within the bone slice in the next section provides more insight.

4.1.1.2 Transient diffusion concentration gradient

H_2O_2 concentration over time at all boundary condition levels are plotted both and with (Figure 12) and without (Figure 13) reactions active.

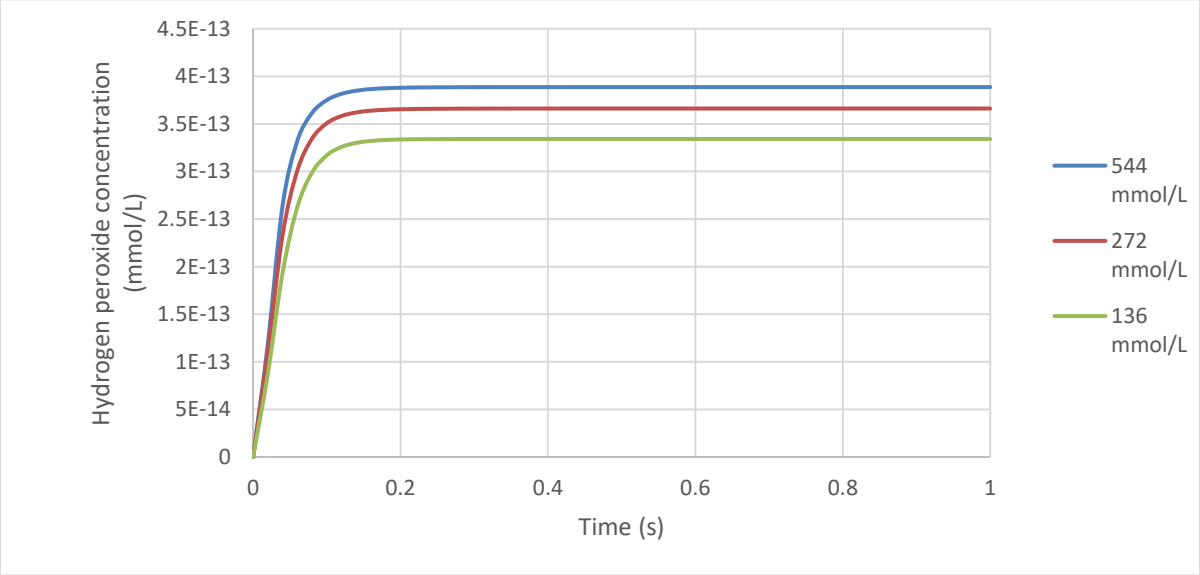

Figure 12 – Hydrogen peroxide concentration in the surveillance pore located near the centre of the volume over time with active reactions. Note that the steady state concentrations are 15 orders of magnitude lower than when reactions are inactive.

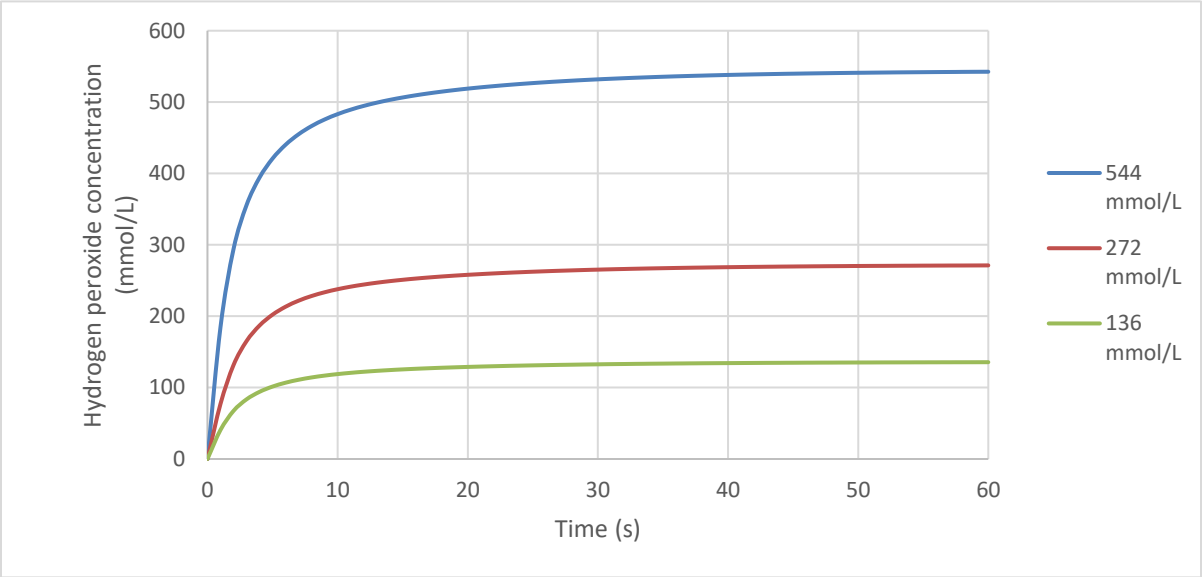

Figure 13 – Hydrogen peroxide concentration in the surveillance pore located near the centre of the volume over time without active reactions.

In the nonreactive system, the concentration in the surveillance pore located near the centre of the representative volume element (RVE) increases over time until it eventually reaches the boundary condition value. The rate of increase is highest initially when the driving force for diffusion due to the concentration gradient between the boundary and the inside of the porous network is highest. As time passes, this driving force decreases proportionally to the decrease in the concentration gradient spatially within the system.

Visualizing this process in Paraview for the $272\,\frac{\text{mmol}}{\text{L}}$ simulation with the RVE sliced halfway through its Z-axis (Figure 14), it is observed that the H_2O_2 initially is only present at the boundary (0 s). At time = 10 s, which is approximately half of the time to steady state, it can be seen that the H_2O_2 has diffused into the network, resulting in a radial concentration gradient about the RVE's centre. The H_2O_2 concentration near the edges of the RVE more closely matches the boundary condition, while the concentration in the middle is still increasing. At steady state, the concentration gradient in the RVE has nearly disappeared, with the remaining pocket of low concentration resting in the middle.

In the reactive system, the surveillance pore concentration does not reach the concentration of the boundary conditions, reaching steady state at values on the order of $10^{-13}\,\frac{\text{mmol}}{\text{L}}$. This marked difference is due to the activation of the reactions, which consume all of the reactant before they have

a chance to diffuse into the RVE, thereby preventing a meaningful increase in concentration in the centre of the bone slice.

Visualizing this process in Paraview for the $272\,\frac{\mathrm{mmol}}{\mathrm{L}}$ simulation with the RVE sliced halfway through its Z-axis (Figure 15), it is observed similarly to the non-reactive system that the $272\,\frac{\mathrm{mmol}}{\mathrm{L}}$ initially is only present at the boundary. As time increases, reaching half of the time to steady state, the concentration profile remains much the same as at time zero, with the exception of some diffusion into the ends of the exposed canals. Even as steady state is reached, this concentration profile does not change, leaving the vast majority of the RVE devoid of H_2O_2.

It is worth noting that this RVE is approximately 11 times smaller in volume than a slice from the experimental specimens. Despite this, with reactions active, it calls into serious doubt whether the ROS will be able to diffuse into the system and cause oxidative damage. Scaling up the system may give insight into this process and will be discussed in the following section.

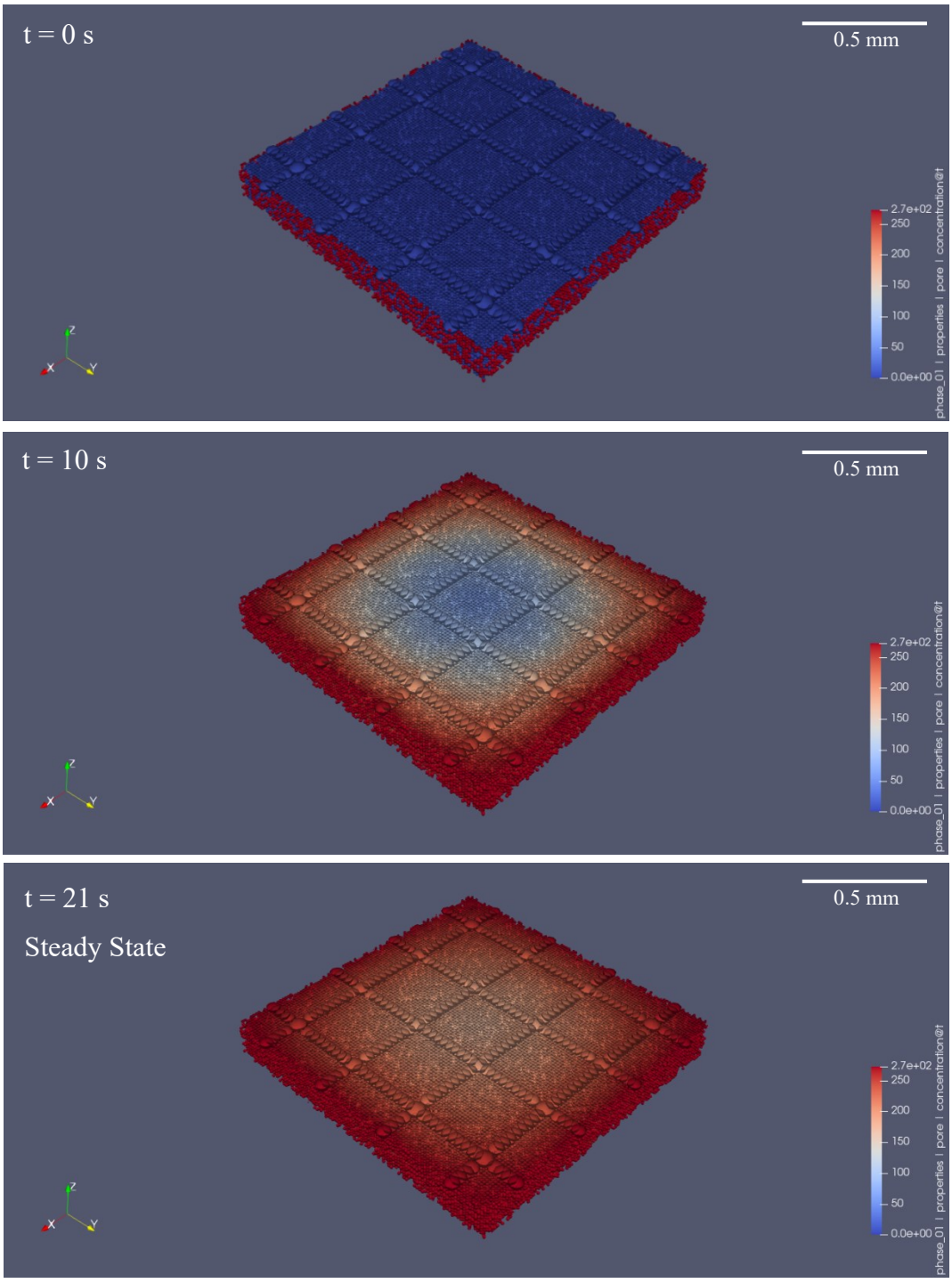

Figure 14 – Transient diffusion of hydrogen peroxide into the RVE with boundary condition = 272 mmol/L.

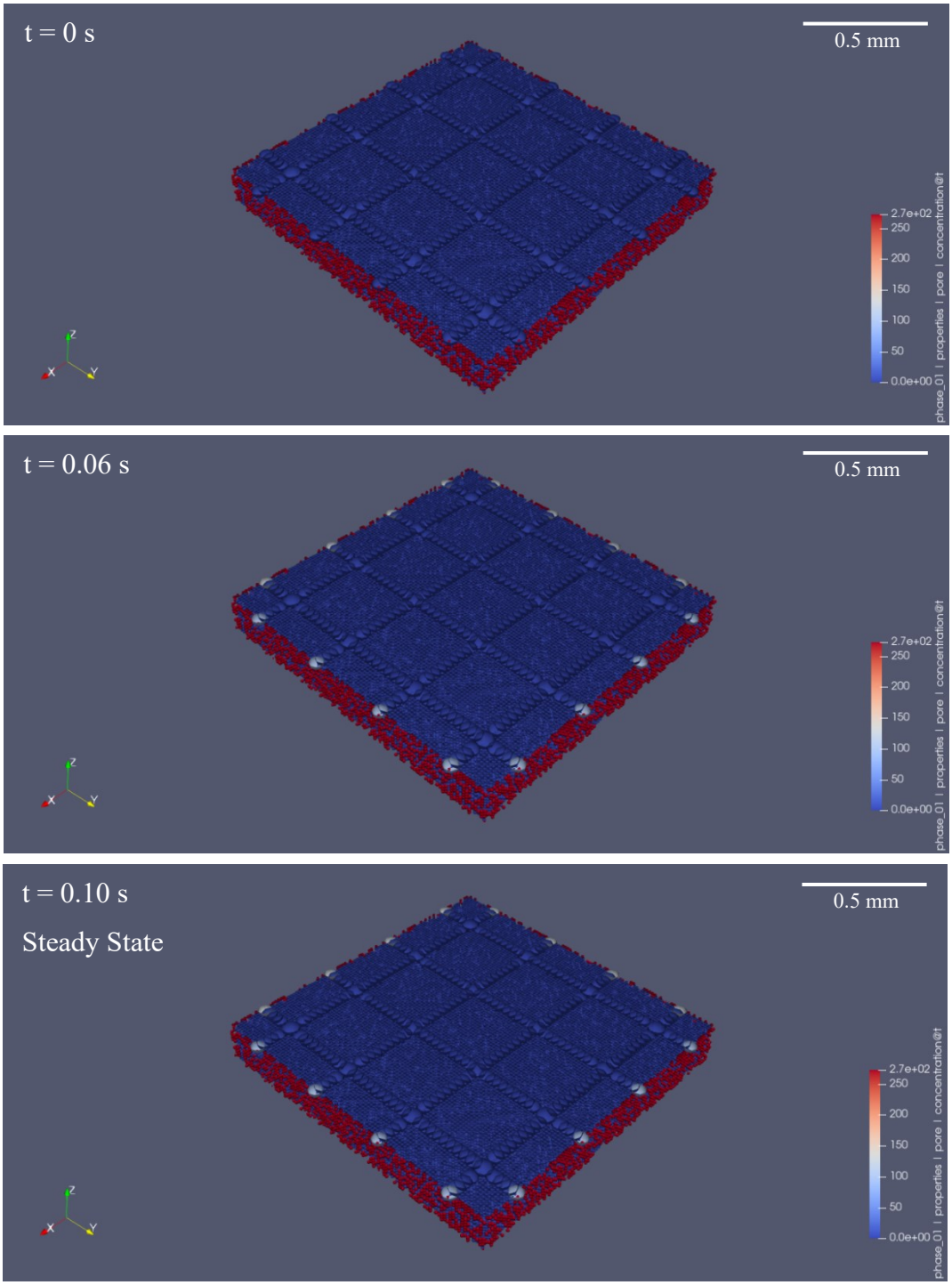

Figure 15 – Transient reactive diffusion of hydrogen peroxide into the RVE with boundary condition = 272 mmol/L.

4.1.2 - 2.4 x 2.4 x 0.30 mm^3 network

4.1.2.1 Time to steady state

Time to steady state was examined at all boundary condition levels both without (Figure 16) and with (Figure 17) the reactions active.

The time to steady state for the nonreactive system was 198 seconds at each boundary condition, a much longer time to steady state than the smaller 1-mm by 1-mm network. This result is sensical, however, as the size of the geometry has quadrupled and the associated distances that individual ROS molecules had to travel were much greater than before. Additionally, the same trend is observed as in the first network where the time to steady state remains constant, despite differing concentration gradient driving forces at each boundary condition.

For the reactive system, the time to steady state was 8.64 seconds, which was considerably faster than the nonreactive case and comparable to the nonreactive 1.2 x 1.2 x 0.30 mm^3 system discussed in the previous section. As with the previous geometry, due to the extremely short time to steady state for the reactive system, even shorter than the nonreactive system, it can be posited that the ROS may be reacting and not penetrating deeply into the matrix. The analysis of the simulated concentration profile within the bone slice in the next section provides more insight.

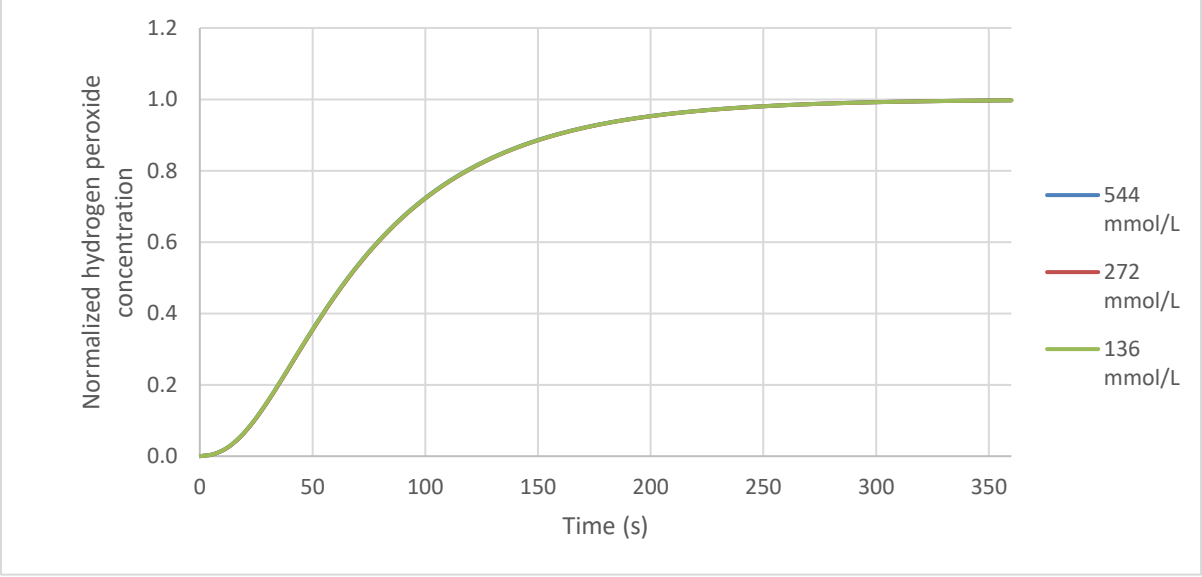

Figure 16 – Normalized surveillance pore hydrogen peroxide concentration over time at each boundary condition without active reactions.

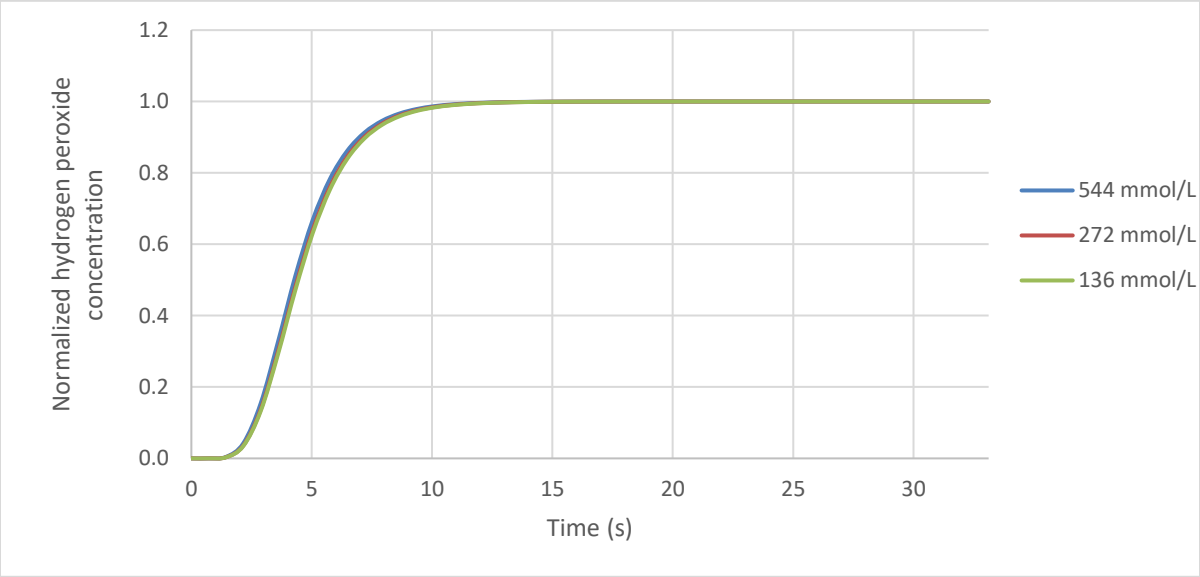

Figure 17 – Normalized surveillance pore hydrogen peroxide concentration over time at each boundary condition with active reactions.

4.1.2.2 Transient diffusion concentration gradient

H_2O_2 concentration over time at all boundary condition levels are plotted both without (Figure 18) and with (Figure 19) reactions active. In the nonreactive case, similar to the 1.2 x 1.2 x 0.30 mm^3 system discussed in the previous section, the concentration in the surveillance pore located near the centre of the representative volume element (RVE) increases over time until it eventually reaches the boundary condition value. The rate of increase is highest initially when the driving force for diffusion due to the concentration gradient between the boundary and the inside of the porous network is highest. As time passes, this driving force decreases proportionally to the decrease in the concentration gradient spatially within the system. Visualizing this process in Paraview for the $272\frac{\text{mmol}}{\text{L}}$ simulation with the RVE sliced halfway through its Z-axis (Figure 20), it is observed that the $272\frac{\text{mmol}}{\text{L}}$ initially is only present on the two edges at $x = 0$ and $y = 0$. At time = 18 s, the diffusion into the RVE becomes clear, identifying that this RVE is acting as a quarter of the larger volume under study. At time = 102 s, which is approximately half of the time to steady state, it can be seen that the $272\frac{\text{mmol}}{\text{L}}$ has diffused into the network, resulting in a radial concentration gradient

about the RVE's centre. At time = 198 s, this concentration gradient disappears and the system reaches steady state at the boundary concentration.

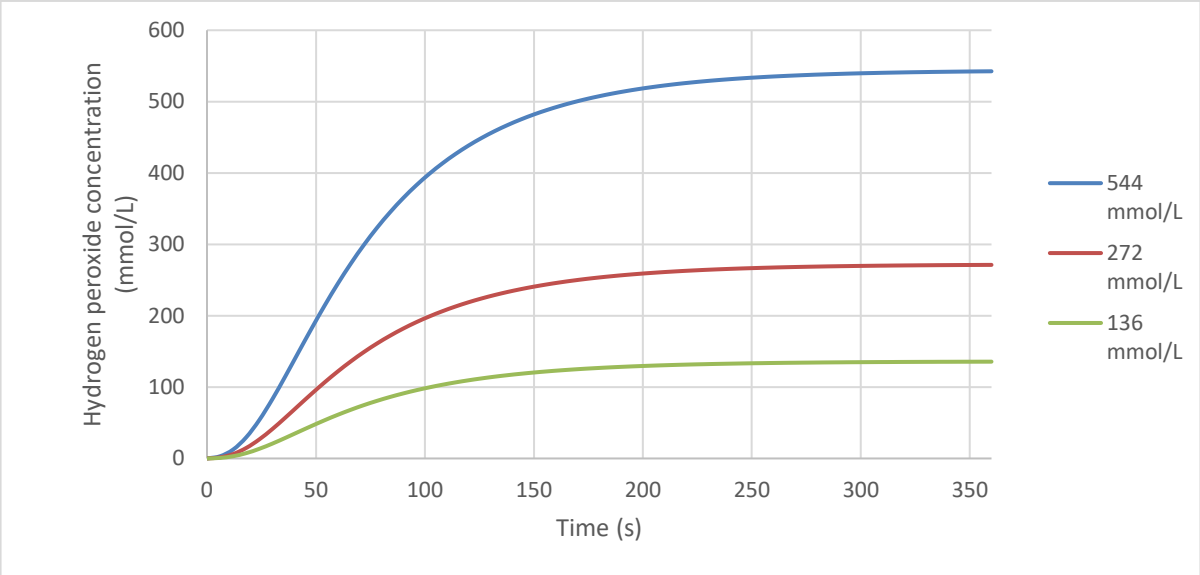

Figure 18 – Hydrogen peroxide concentration in the surveillance pore located near the centre of the volume over time without active reactions.

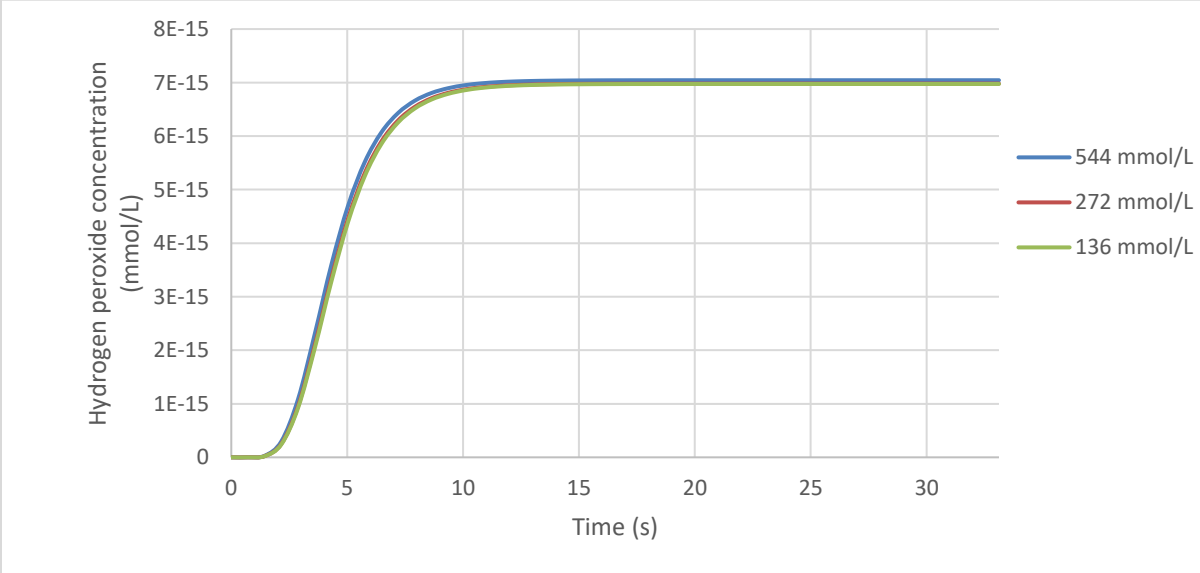

Figure 19 – Hydrogen peroxide concentration in the surveillance pore located near the centre of the volume over time with active reactions.

In the reactive system, the surveillance pore concentration does not reach that of the boundary conditions, reaching steady state at values on the order of $10^{-15}\,\frac{\mathrm{mmol}}{\mathrm{L}}$. Similarly to the previously studied system, this marked difference is due to the activation of the reactions, which consume all of the reactant before it has a chance to diffuse into the RVE, thereby preventing a tangible increase in concentration in the centre of the bone slice.

Visualizing this process in Paraview for the $272\,\frac{\mathrm{mmol}}{\mathrm{L}}$ simulation with the RVE sliced halfway through its Z-axis (Figure 21), it is observed similarly to the non-reactive system that the $272\,\frac{\mathrm{mmol}}{\mathrm{L}}$ initially is only present on the two edges at $\mathrm{x} = 0$ and $\mathrm{y} = 0$. As time increases, reaching half of the time to steady state, the concentration profile remains much the same as at time zero, with the exception of some diffusion into the ends of the exposed canals. Even as steady state is reached, this concentration profile does not change, leaving the vast majority of the RVE devoid of $\mathrm{H_2O_2}$. This RVE is still approximately 2.8 times smaller in volume than the bone slices studied experimentally, leaving a gap in the exact concentration gradient that would be predicted to occur *in vitro*. However, the trends captured in this system and the $1.2 \times 1.2 \times 0.30\ \mathrm{mm^3}$ RVE still offer strong conceptual insight and qualitative predictability for *in vitro* experiments.

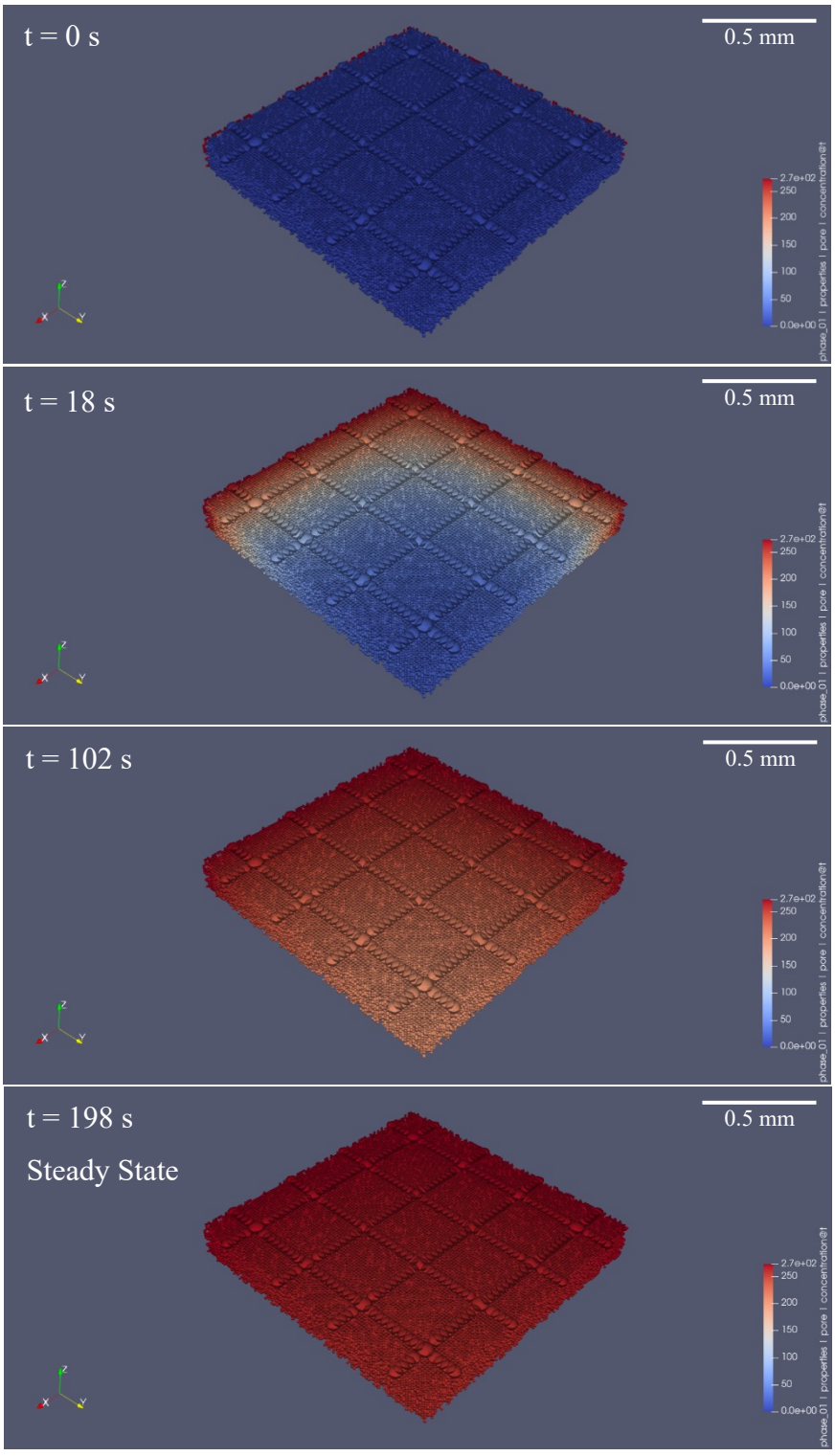

Figure 20 – Transient diffusion of hydrogen peroxide into the 2.4 x 2.4 x 0.30 mm^3 RVE with boundary condition = 272 mmol/L.

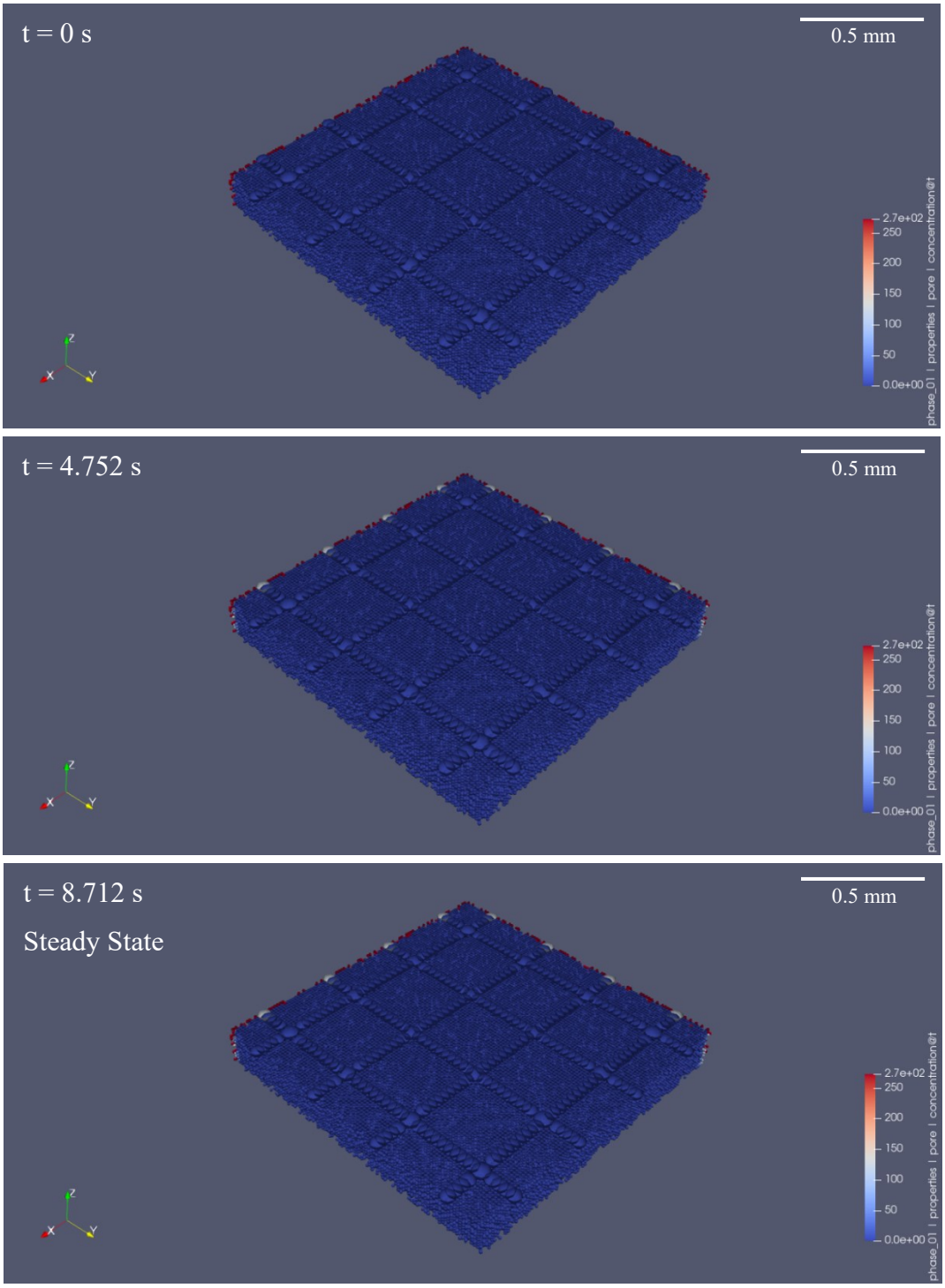

Figure 21 – Transient reactive diffusion of hydrogen peroxide into the 2.4 x 2.4 x 0.30 mm^3 RVE with boundary condition = 272 mmol/L.

4.1.3 Sensitivity Analysis of *k*

As seen in the transient reactive simulations, ROS are unable to diffuse deep within the modelled bovine cortical bone when reactions are active. In order to increase the penetrance of ROS into the bone's porous network, two main options are available: 1) decrease the rate of reaction, and 2) increase the rate of diffusion of ROS into the bone. The first option can be achieved practically by lowering the temperature of the system, thereby slowing down the reaction kinetics. The second option involves changing the ROS' solvent to a chemical that can diffuse more quickly into the bone, for example, supercritical carbon dioxide as proposed in the designed *in vitro* model. In both cases, the developed bovine cortical bone pore network model can offer predictive capabilities, however it is much more practical to run studies of reaction rates than to scour the literature for data on complex chemical mixtures. Additionally, OpenPNM's capabilities are limited when it comes to modelling supercritical fluids. Thus, the justification for a parametric study of the reaction constant k for the decomposition of hydrogen peroxide into the extremely short-lived free radicals which cause oxidative damage is provided.

Results of the parametric study on k are provided in Figure 22. It is clear from Figure 23 that values of k on the order of 10^{-19} and larger nullify the chance of any hydrogen peroxide diffusing into the

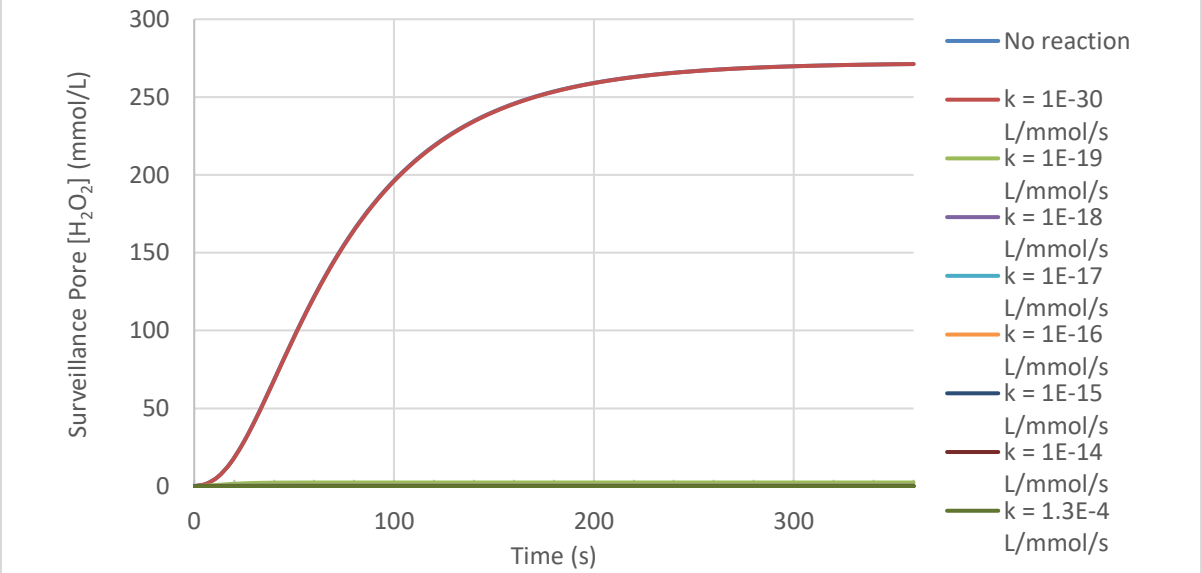

Figure 22 – Parametric study of the reaction constant depicting its influence on the surveillance pore concentration in the 2.4 x 2.4 x 0.30 mm^3 RVE. Time interval 0 – 360 s. Boundary condition: 272 mM.

centre of the RVE in appreciable amounts. Looking more closely at the region near the origin in Figure 23, it is observed that there is some slight variation in the steady state concentrations for $k \geq 10^{-19}$, however compared to the applied boundary condition of $272\,\frac{\text{mmol}}{\text{L}}$, these values are essentially negligible. It is also noteworthy that to achieve the boundary condition concentration in the surveillance pore at the centre of the RVE, the reaction constant must be on the order of 10^{-30}, which results in a response similar to the non-reactive case. This indicates that in order to achieve an appreciable amount of ROS deep within the bone's porous network, the rates of reaction must be reduced by 15 orders of magnitude or turned off altogether.

This foreshadows an important challenge in the experimental work contained within this thesis. The simulation results suggest that H_2O_2 will only accumulate in appreciable concentrations at the bone's surface during the *in vitro* ROS soak experiment. This in turn, will limit the production and reaction of toxic free radicals to this region of the tissue, resulting in an accumulation of oxidative damage localized near the specimen's surface with no penetration further into the bone's volume. The lack of uniformity in the oxidative damage profile may have consequences for the observed fracture toughness and work to fracture values as the fracture testing technique utilized for specimen

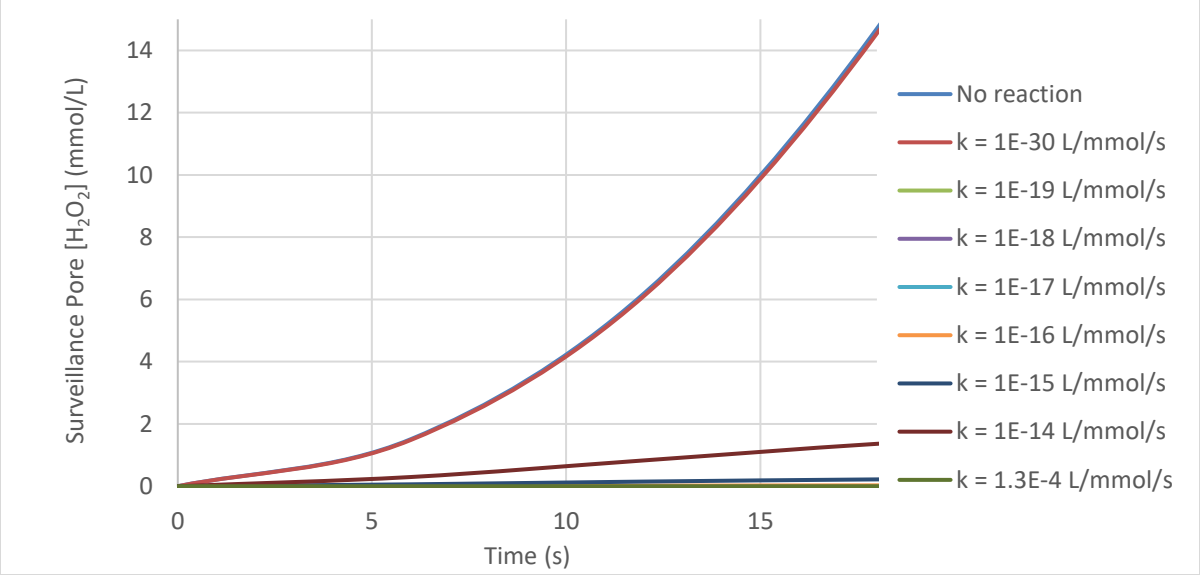

Figure 23 – Parametric study on the reaction constant depicting the influence on the surveillance pore concentration in the 2.4 x 2.4 x 0.30 mm^3 RVE. Time interval 0 – 18 s showcasing the slight differences in concentration at different k values. Boundary condition: 272 mM.

characterization may not be able to detect this damage. The 4-point bending fracture tests conducted utilize a chevron notch to cause the formation of a crack closer to the centre of the bone beam's cross-sectional area, which may be too far away from the beam's surface to experience the effects of the oxidative damage.

4.2 Reactive Oxygen Species Soak Experiment

This section details the results of the reactive oxygen species soak experiment using the H_2O_2 system catalyzed by $CoCl_2$.

4.2.1 Fracture Testing Results

Data gathered from fracture testing included work to fracture, peak load, and maximum crosshead displacement before unstable fracture of each specimen. After fracture, chevron notch area was measured from images. This section details the analysis of these data.

4.2.1.1 Load-deflection curves

Load-deflection curves for each study group are presented in Figure 24. By inspection, an obvious decrease in peak load exists between all groups and the gamma irradiated positive controls.

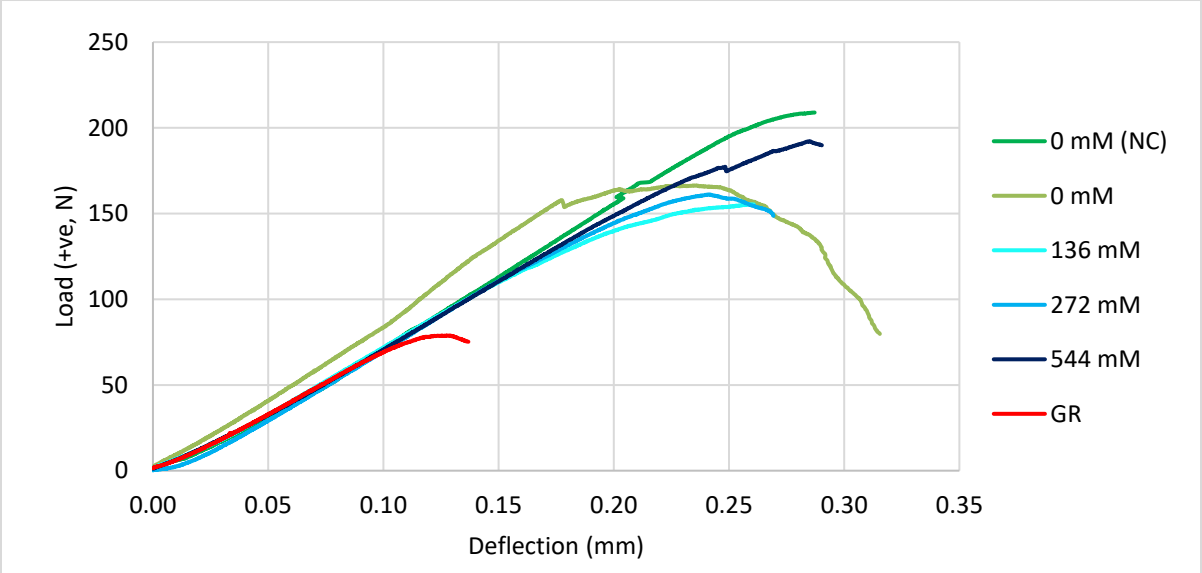

Figure 24 – Load-deflection curves for all specimens at all treatment levels. NC: no-catalyst negative control group; GR: gamma irradiated positive control group.

Additionally, all of the groups had at least one specimen that exhibited non-linear behaviour indicating stable tearing except for specimens in the 0.136 M and 0.272 M treatment groups. The 0 M negative control group had the most variation in both peak load and maximum deflection compared to all other groups, while the 0.136 M treatment group had the most consistent specimen response.

4.2.1.2 Work to fracture

Work to fracture results for each treatment and control group are shown in Figure 25 and work to fracture as a function of hydrogen peroxide concentration is plotted in Figure 26.

While the gamma irradiated positive controls had noticeably lower work to fracture values than all other groups, no statistically significant differences were observed between all groups as indicated by one-way ANOVA ($p > 0.05$). Additionally, the slope of the linear regression model relating work to fracture to hydrogen peroxide concentration was close to zero and regression was not statistically significant ($p > 0.05$).

One possible explanation for the wide variance in work to fracture values causing this result may have been the difference between specimens that exhibited stable tearing or brittle fracture during

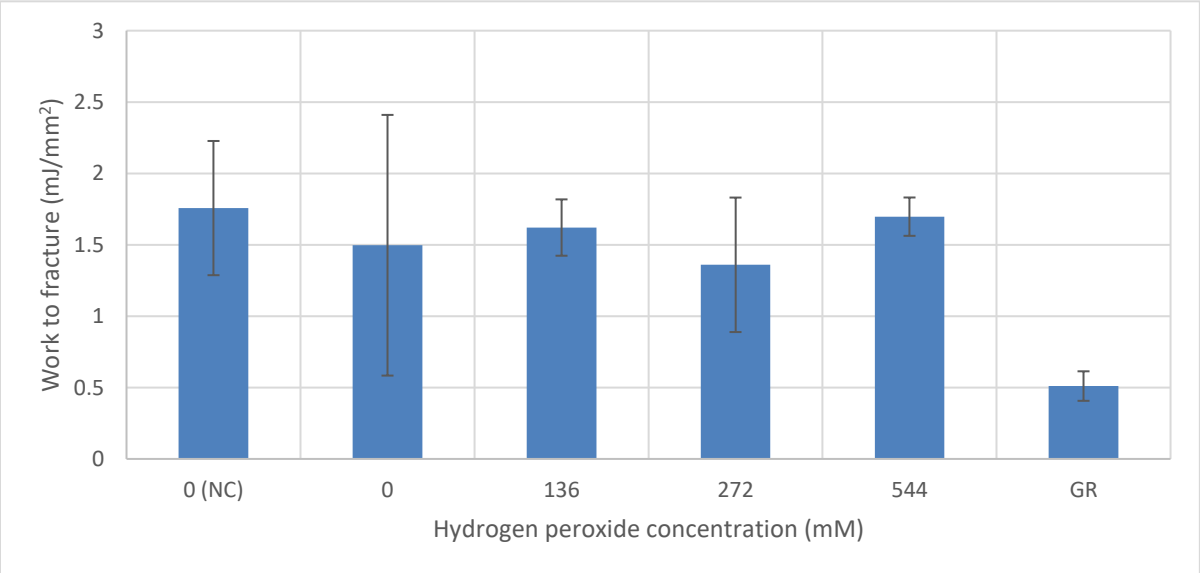

Figure 25 – Work to fracture for all treatment and control groups. Significance was assigned at the α = 0.05 level. Data presented as mean with standard deviation. GR: Gamma irradiated positive control; NC: no catalyst negative control. n = 3 for NC and GR. n = 2 for 0 – 544 mM.

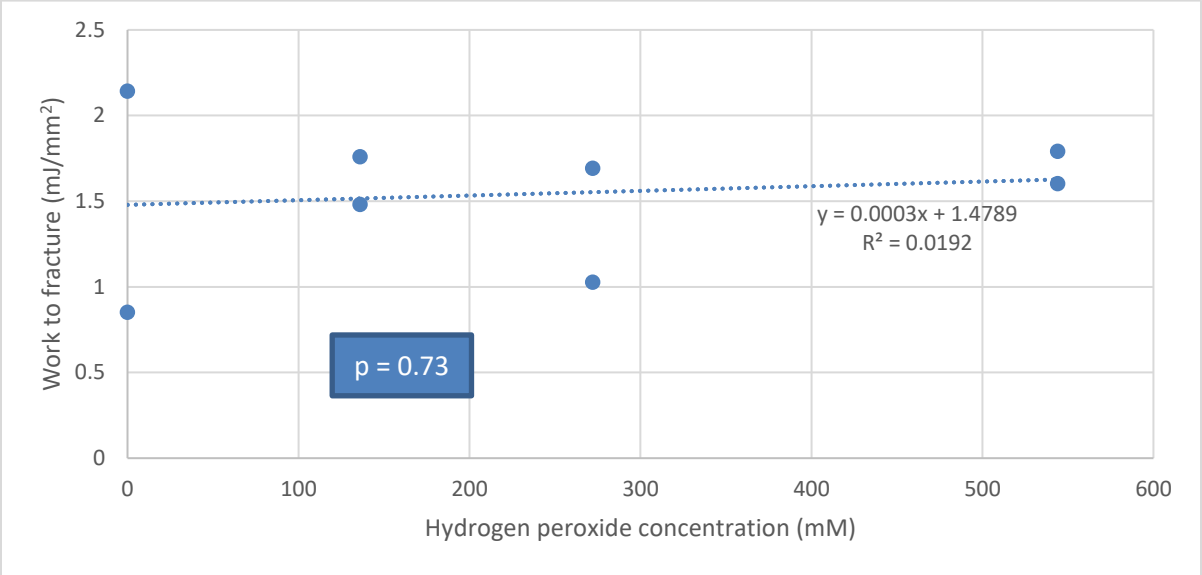

Figure 26 – Linear regression analysis of work to fracture as a function of hydrogen peroxide concentration for treated groups including 0 mM negative control. n = 2. Significance was assigned at the α = 0.05 level.

testing. Work to fracture, as its name suggests, is a measure of the work done by the testing machine on the bone beam to cause it to fracture and is determined using the area under the load-deflection curve normalized to the fracture surface area for each sample. As such, specimens which exhibited stable tearing during testing possessed load-deflection curves with larger areas due to the higher loads sustained over larger deflections when compared to samples which exhibited brittle fracture. Load-deflection curves for specimens that underwent unstable brittle fracture abruptly dropped to zero load at the point of fracture, reducing the amount of area under the curve.

One key promoter of stable tearing in this study was the use of the chevron notch. In other bone fracture mechanics studies, the chevron notch has been deliberately used for this purpose (19). It should be noted that this technique is more often applied to human cortical bone, which typically demonstrates more stable tearing behaviour than bovine. While the purpose of the chevron notch matches that of other stress concentrators in bone fracture testing, notably the single edge notched beam (SENB) approach, by adding an artificial stress concentrator to promote fracture in a more predictable location and cracks with a more predictable trajectory, the chevron notch's unique wedge-like geometry may encourage the bone beam's collagen to engage in the fracture at the tip of the notch, during the fracture's initial moments. The continued engagement of collagen fibres throughout the fracture could then result in stable tearing. However, as observed during fracture testing, stable

tearing does not always occur with this method, and hence it may have introduced an extra element of variation into the area beneath the load-deflection curves for each sample, and in turn, the calculated work to fracture.

Chevron notching aside, Figure 25 clearly depicts challenges in the pursuit of separating differences in work to fracture between all groups. While replicates were collected in each group, with the 0 M no-catalyst and gamma irradiated controls having n = 3, and the 0 M control and treatment groups having n = 2, the variances in each group were still too large for the effects between them to be determined. This most likely indicates that the present study is underpowered and that more replicates in each treatment group are needed to reduce the present variance and make the data more amenable to demonstrating statistically significant differences.

4.2.1.3 Fracture Toughness

Fracture toughness results for each treatment and control group are shown in Figure 27. Regression analysis of fracture toughness is plotted in Figure 28.

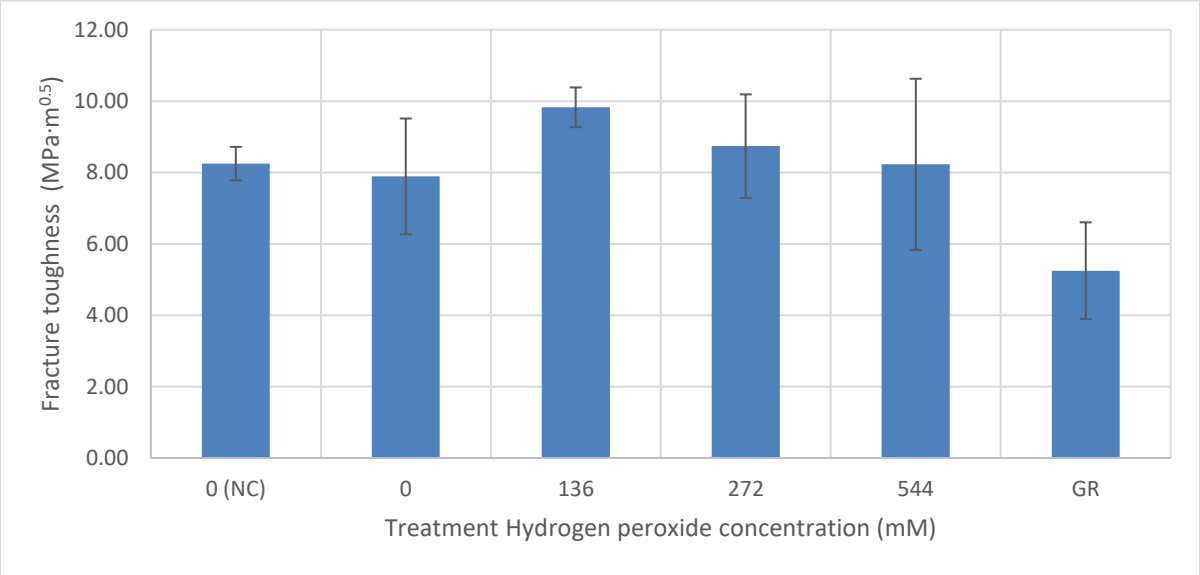

Figure 27 – Fracture toughness for all control and treatment groups. Significance was assigned at the α = 0.05 level. Data presented as mean with standard deviation. GR: gamma irradiated positive oxidative damage controls; NC: no-catalyst negative controls. n = 3 for NC and GR. n = 2 for 0 – 544 mM.

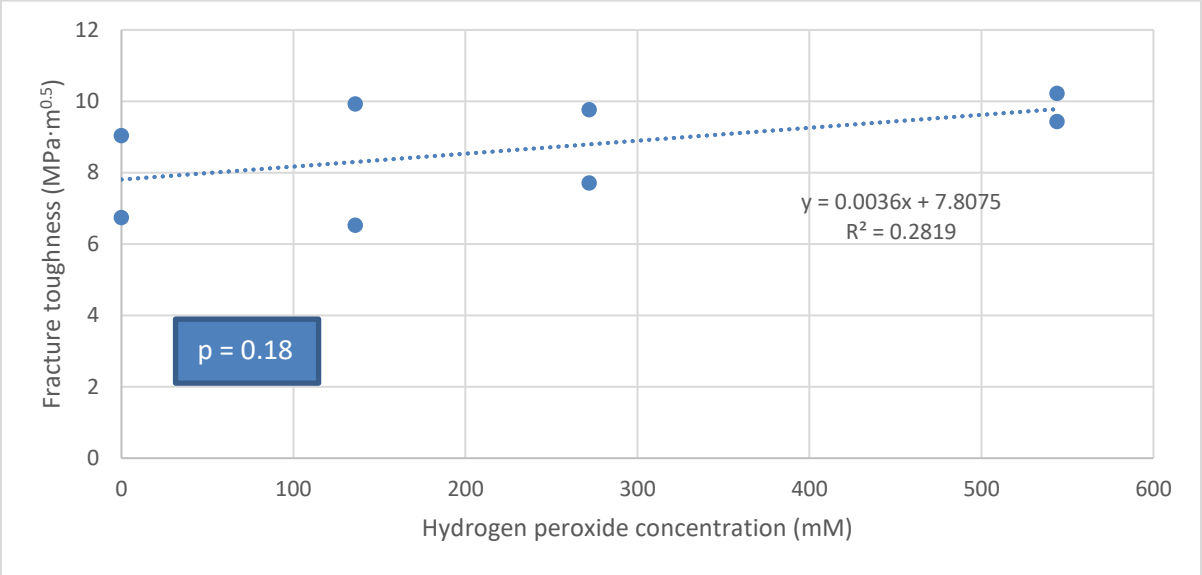

Figure 28 – Linear regression analysis of fracture toughness as a function of hydrogen peroxide concentration for treated groups including 0 mM negative control. Significance was assigned at $\alpha = 0.05$ level. n = 2.

No statistically significant differences were observed between all treatment groups as indicated by one-way ANOVA ($p = 0.07$, $p > 0.05$). A significant decrease in normalized peak load for gamma irradiated specimens would be expected and is consistent with other studies examining bovine cortical bone fracture behaviour following gamma irradiation (12). Burton and colleagues observed not only the absence of nonlinear deformation following the onset of nonlinearity, indicating the loss of "plasticity", but also a decrease in peak load at fracture. The extreme oxidative damage impacted the bone's collagen network, resulting in the bone's embrittlement (12).

While not statistically significant, there is a numerical difference between the mean fracture toughness values for the 136 mM, 272 mM, and 544 mM treatment groups, listed in decreasing order. As with the work to fracture results, the lack of statistical significance greatly decreases the confidence with which inferences may be drawn from the data. Reducing variance by increasing replicates would likely provide an increase in statistical power that would better resolve this issue and may reveal interesting trends in the data.

Linear regression analysis of fracture toughness for the 0 mM, 136 mM, 272 mM, and 544 mM treatment groups determined that there was no statistically significant correlation between hydrogen peroxide concentration and specimen fracture toughness ($p > 0.05$). As per this thesis' hypothesis, it was expected that at higher hydrogen peroxide concentrations, the fracture toughness would decrease, indicating an increase in oxidative damage within the bone specimens and therefore an increase in bone fragility. Interestingly, the lack of statistical significance here may serve to protect this thesis' hypothesis by negating any significance assigned to the unexpected weakly positive correlation shown in Figure 28.

4.2.1.4 Maximum deflection

Maximum deflection results for each treatment and control group are shown in Figure 29. Regression analysis of fracture toughness is plotted in Figure 30.

Similarly to the fracture toughness results, there were no statistically significant differences between groups ($p > 0.05$). Figure 29 also depicts a numerical difference between the mean maximum deflection values for the 136 mM, 272 mM, and 544 mM treatment groups, listed in decreasing order,

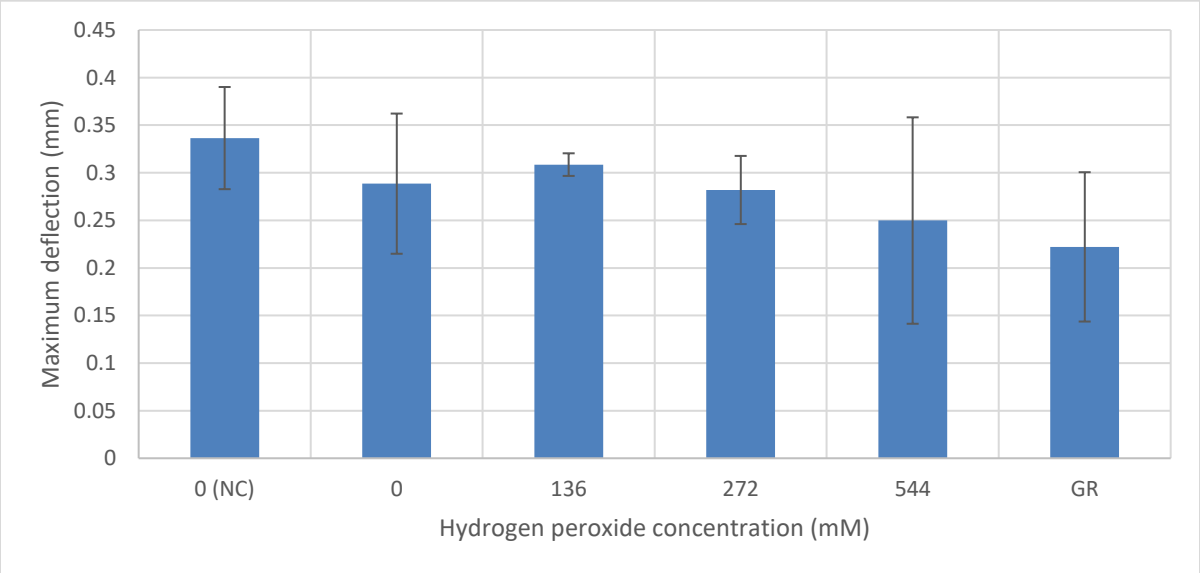

Figure 29 – Maximum deflection for all groups. Significance was assigned at the $\alpha = 0.05$ level. Data presented as mean with standard deviation. GR: gamma irradiated controls; NC: no-catalyst controls. n = 3 for NC and GR. n = 2 for 0 – 544 mM.

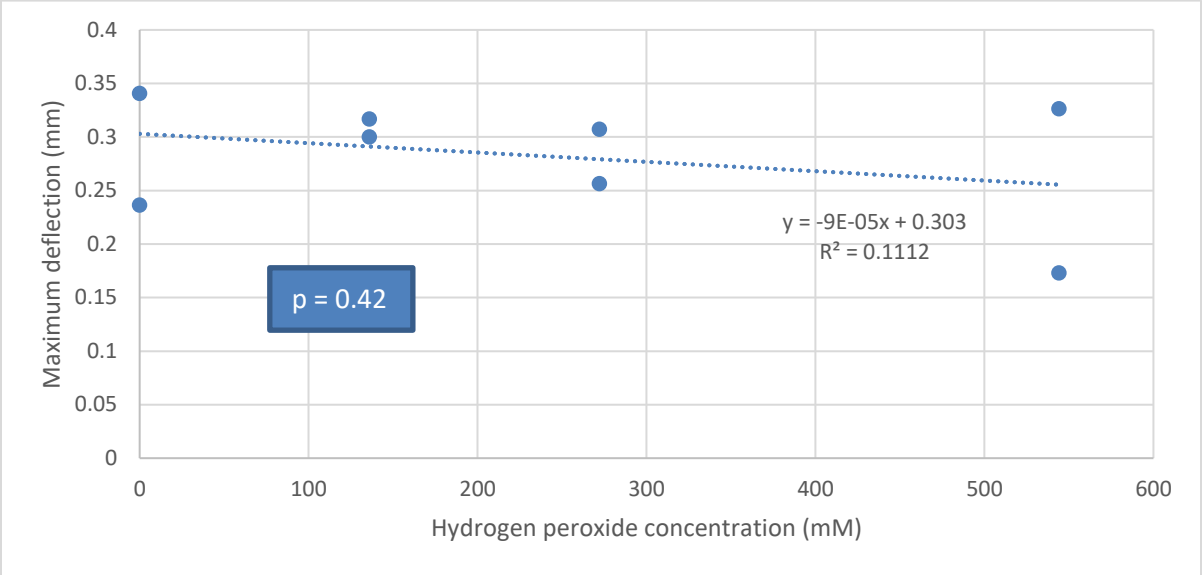

Figure 30 – Linear regression analysis of maximum deflection as a function of hydrogen peroxide concentration for treated groups including 0 M negative control. Significance was assigned at the α = 0.05 level. n = 2.

seen in the fracture toughness results (Figure 27). As with the other quantities studied, the lack of statistical significance greatly decreases the confidence with which inferences may be drawn from the data. Reducing variance by increasing replicates would likely provide an increase in statistical power that would better resolve this issue and may reveal interesting trends in the data.

The inconsistent display of stable tearing and brittle fracture during fracture testing likely had an influence on the variance seen in maximum deflection values. Specimens which exhibited stable tearing were capable of fracturing at higher maximum deflection values compared to those which demonstrated brittle fracture. The nonlinear behaviour of beams in stable tearing following crack growth initiation allowed them to more gradually dissipate energy supplied by the mechanical testing machine as well as energy released by the creation of the fracture surfaces. This allowed beams undergoing stable tearing to have a higher chance of fracturing at higher maximum displacement compared to those that did not.

4.2.1.5 Chevron notch area

Chevron notch area results for each treatment and control group are shown in Figure 31. One-way ANOVA indicated that there were no statistically significant differences present between any of the control or experimental groups ($p > 0.05$).

Chevron notch area was analyzed to determine if variance in notch area introduced any bias into the data, for example if one group's notch areas were significantly larger or smaller than the others. The lack of statistical significance between groups indicates that differences in chevron notch area likely did not impact work to fracture, fracture toughness, or maximum deflection values in a confounding manner.

While the nominal chevron notch area prescribed by the ASTM standard generally followed for specimen preparation and four point fracture testing (ASTM C1421-18: Determination of Fracture Toughness of Advanced Ceramics at Ambient Temperature) is 6.928 mm^2, manual machining of the notches using a Buehler Isomet metallurgical saw with a custom notching jig proved difficult to replicate this value (109). The overall average chevron notch area machined was 7.889 ± 0.371 mm^2, which was 0.961 mm^2 higher than the value listed in the standard. Laboratory expertise in this area

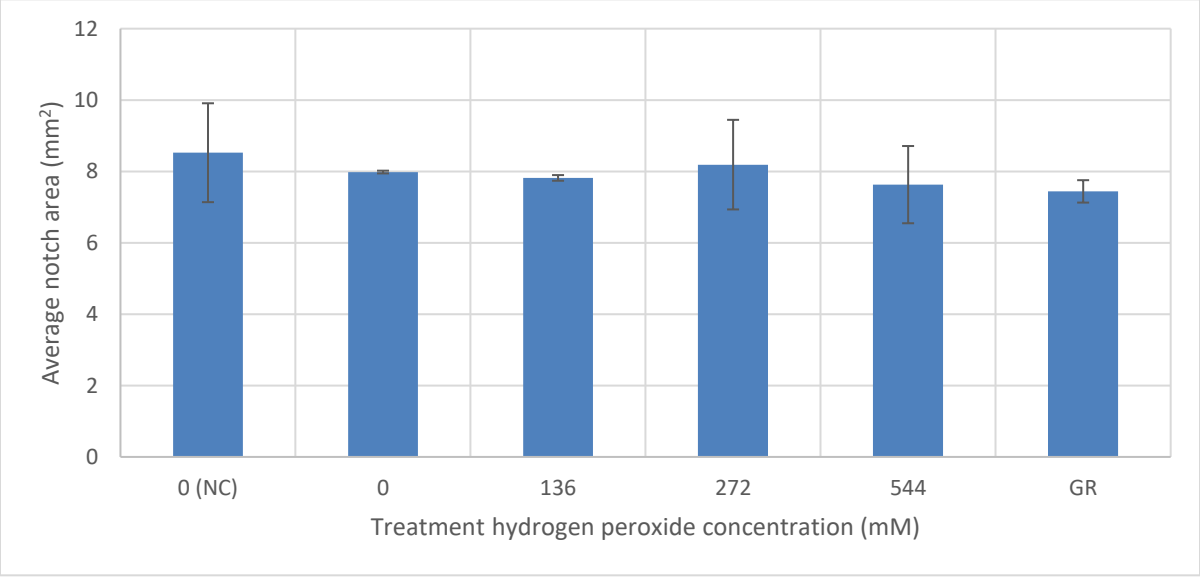

Figure 31 – Mean chevron notch area for all groups. Significance was assigned at the α = 0.05 level. n = 2. Data presented as mean with standard deviation. GR: gamma irradiated controls; NC: no-catalyst controls. n = 3 for NC and GR. n = 2 for 0 – 544 mM.

within the author's research group has often indicated the challenge of perfectly replicating the specifications of this standard and indeed some leading researchers in bone toughness research have altogether deviated from ASTM C1421-18 and adapted the notch dimensions to suit their testing purposes (19). While the difficulty of replicating this material testing standard is certainly salient, the data presented here suggests that it was not a significant source of bias in fracture testing.

4.2.2 Fluorescent Imaging

Fluorescent imaging of slices taken near the middle of the length of each cortical bone beam helped elucidate the distribution of carbonyls and, in turn, oxidative damage within each specimen. Images and their analyses are discussed in the following subsections.

4.2.2.1 Raw image analysis

Raw images compiled into Z-projections while taking into account focal length are displayed in Figure 32.

All images produced a green fluorescent signal, including the negative controls. This fluorescence was expected as carbonyls naturally exist in the amino acids which compose the collagen peptides in the bone's organic phase. These carbonyls would be stained by FTC and hence produce a corresponding green fluorescent signal when imaged using the confocal microscope. Areas with unnaturally high carbonyl concentrations indicated regions of oxidative damage. The $\cdot OH$ and $\cdot O_2^-$ free radicals produced from H_2O_2 attacked the amino acids in these regions, abstracting hydrogen atoms to produce carbonyls, and perhaps even fragment protein backbones (10,73). These regions would produce relatively stronger fluorescent signals.

By inspection, some key details in the raw images are revealed. The gamma irradiated positive oxidative damage control appeared brightest and had a uniform distribution of fluorescence across its surface as expected. In direct contrast, the no-catalyst negative control appears darkest but also possesses an equally uniform distribution of fluorescence.

The 544 mmol/L treatment group exhibits the most striking images featuring edges that are clearly much brighter than their centres, with the exception of the top left corner of the sample where the signal was attenuated due to imaging constraints creating an image artifact. The other treatment groups also display this trend.

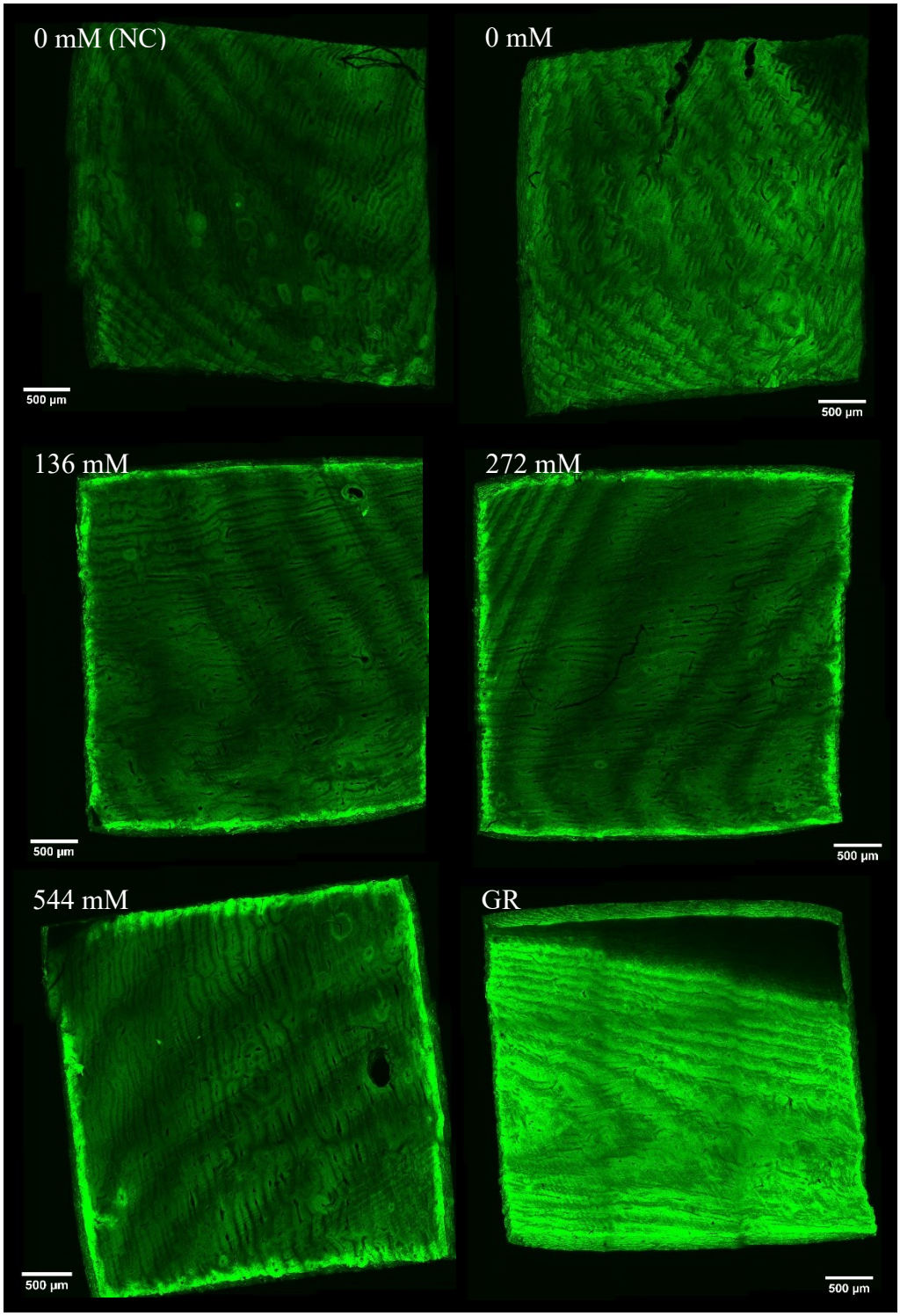

Figure 32 – Z-projections of stitched raw fluorescent images taken of each sample using a confocal microscope. NC: no-catalyst negative control; GR: gamma irradiated positive control. GR z-stack: 400.1 µm. NC & 0 – 544 mM z-stack: 459.9 µm. Scale bars: 500 µm.

Other small bright regions are visible around osteons present in the samples. These additional bright spots are in line with transport limitations within the bone's porous network. Osteons contain Haversian canals at their centre. As seen in the simulation results, Haversian canals, and their connected Volkmann's canals, act as areas of higher diffusive conductance for ROS due to their larger diameter than the other pores present.

Specifically in bovine bones, there are two main types of cortical bone present. The first is osteonal cortical bone, which contains high densities of osteons, and therefore canals (78). The second major type is plexiform cortical bone, which is composed of a brick-like structure and virtually devoid of osteons (78,151). The images in Figure 32 depict plexiform bone in which only the 544 mM sample shows an osteon highlighted due to fluorescence near the bottom left corner. Plexiform bone would offer more diffusive resistance to H_2O_2 transport than osteonal bone due to its lack of canals, and this may have exacerbated the lack of diffusion into the centre of each sample's area and, hence, the oxidative damage gradient. It is important to note that human cortical bone is largely osteonal and may offer different transport resistances, therefore a more osteonal sample of bovine cortical bone may be more representative (151).

4.2.2.2 Image thresholding analysis

Fluorescent images in greyscale with the applied threshold are displayed in Figure 33. These images confirm the initial observations by inspection. The gamma irradiated positive control still contains areas of high pixel intensity distributed relatively more uniformly over its surface area than the other specimens. While one of no hydrogen peroxide negative controls virtually matches the no-catalyst control used to devise the threshold, the other retained more signal than expected on its edges.

The 544 mmol/L treatment group shows most clearly the fluorescent signal, and therefore carbonyls created via oxidative damage, on its edges, with the exception of the artifact in the top left corner. This key qualitative evidence matches the concentration gradient observed during transient reactive diffusion simulations on both RVEs. The ROS was unable to penetrate deep within the bone's porous structure due to the prohibitively high rate of the hydrogen peroxide decomposition reaction. The damage profile shown in these images reflects the added residence time not captured in the simulation. If a given area of bone (i.e., the edges of a slice) were exposed to free radicals for a longer period of time, it would be reasonable to predict that more oxidative damage would accumulate there.

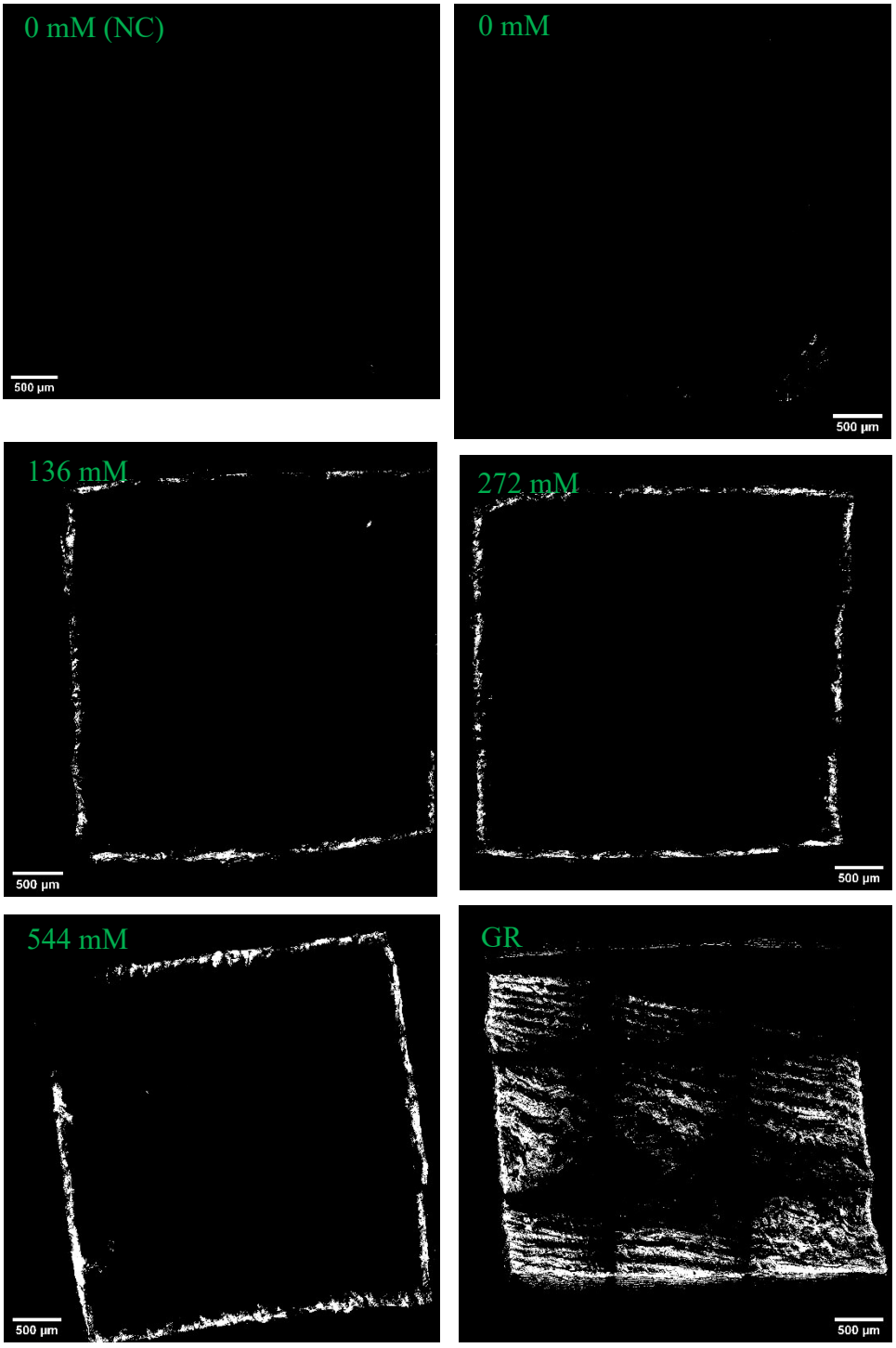

Figure 33 – Stitched confocal microscopy images of FTC-stained bone beam slices after threshold application. Threshold was set according to 0 M (NC) sample fluorescence to remove 99.5% of pixels. NC: no-catalyst negative control; GR: gamma irradiated positive control. GR z-stack: 400.1 µm. NC & 0 – 544 mM z-stack: 459.9 µm. Scale bars: 500 µm.

The regions that did not see concentrations of hydrogen peroxide near the boundary condition values (i.e., the interior of the beam and middle of the slices) would not have the chance for such exposure and as such would not accumulate carbonyls indicating oxidative damage. The 272 mmol/L and 136 mmol/L treatment groups also echo this trend.

4.2.2.3 Mean pixel intensity analysis

Mean pixel intensity was computed for each slice in its entirety and for a rectangular region of interest (ROI) in its centre using ImageJ. Thresholds were not applied for this analysis. Results were taken as mean and standard deviation values from ImageJ.

Full slice fluorescence depicted in Figure 34 suggests that the gamma irradiated positive control and the no-catalyst control are saliently different, while there may still be some overlap between each of these two groups and the remaining treatments.

Plotting the central ROI mean pixel intensity values in Figure 35 tells a slightly more compelling story. Less overlap is present between the gamma irradiated positive control and the other treatment

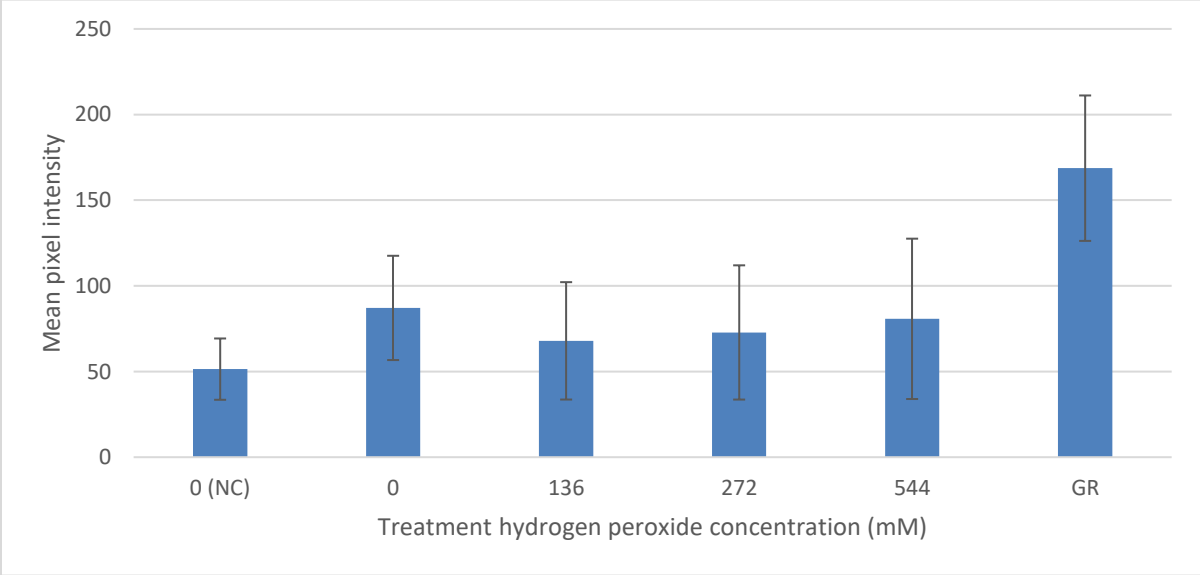

Figure 34 – Full slice mean pixel intensity values for all groups. Significance was assigned at the α = 0.05 level. n = 1. Data presented as mean with standard deviation. GR: gamma irradiated controls; NC: no-catalyst controls.

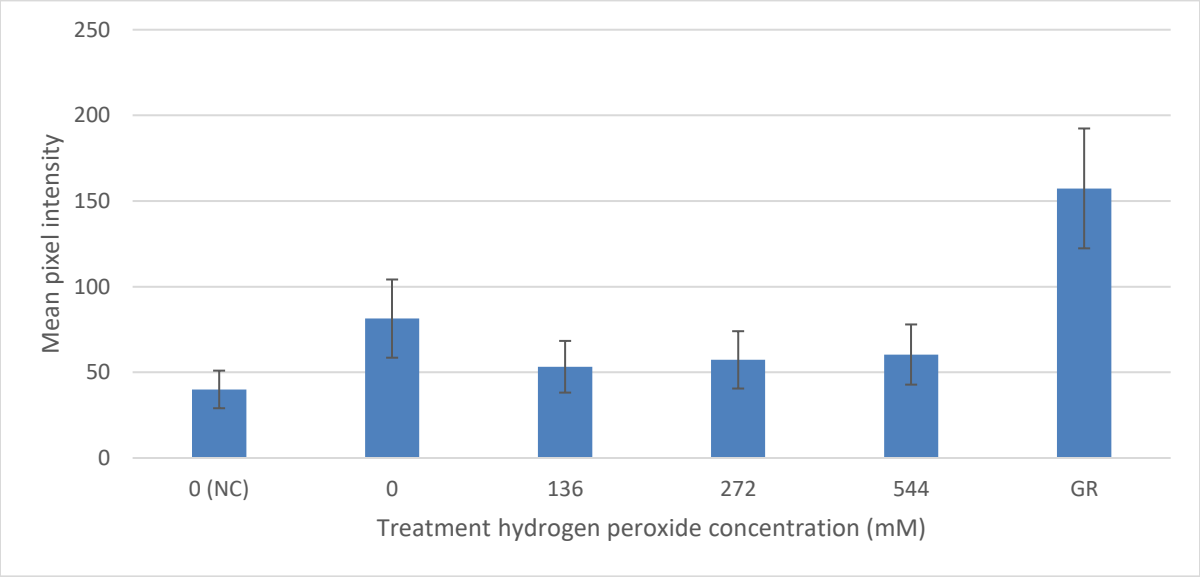

Figure 35 – Central ROI mean pixel intensity values for all groups. Significance was assigned at the α = 0.05 level. n = 1. Data presented as mean with standard deviation. GR: gamma irradiated controls; NC: no-catalyst controls.

groups. Some overlap is still present between the no-catalyst negative control and the other treatment groups, with the exception of the no hydrogen peroxide negative control. These results indicate that replicates are required to determine if these suggested trends are statistically significant. Should they be significant, they could provide a quantitative way to analyze fluorescent images for the distribution of oxidative damage with bone specimens. Current approaches to quantify carbonyls as indicators of oxidative damage are assay-focused (152,153).

4.2.2.4 Pixel intensity distribution analysis

The pixel intensity distributions for all specimens are displayed in Figure 36 and the area under each curve is captured in Figure 37.

Pixel intensity values ranged from 0 – 255, with the latter representing saturated pixels; those in the image at their maximum intensity. The no catalyst 0 mM negative control had the highest peak at an intensity of 42 and no pixels with an intensity of 255. The 0 mM negative control featured a quite different distribution, with a much lower peak around an intensity of 74 and 8 saturated pixels. Treatment groups 136 mM and 272 mM featured similar peaks at intensities of 55 and 54 respectively

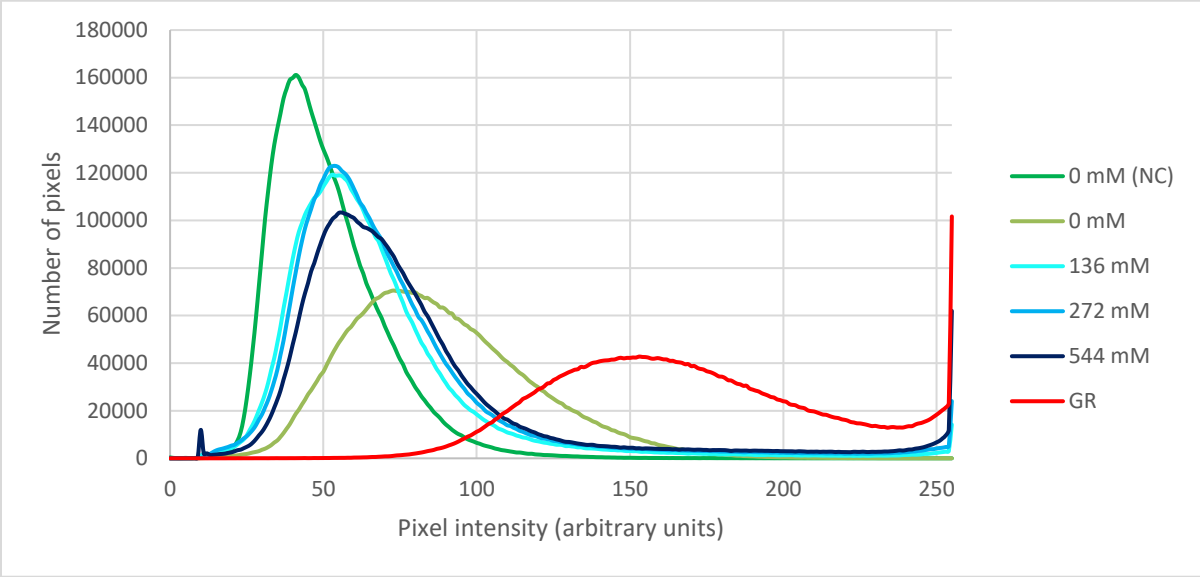

Figure 36 – Pixel intensity histograms for each specimen. Saturated pixels were those at the maximum possible pixel intensity value of 255.

with the curve for 272 mM being slightly more flattened, indicated by its higher number of pixels at higher intensity values compared to the 136 mM group. The 544 mM group also peaked near these two treatment groups at an intensity of 56 but with a lower number of pixels and possessed a flatter curve than the 272 mM group. The number of saturated pixels was also higher in the 544 mM group compared to the 272 mM group, which was in turn higher than the 136 mM group. The gamma irradiated positive oxidative damage control possessed the flattest curve, peaking at a much lower number of pixels at an intensity of 153 and the highest number of saturated pixels, greater than the number of pixels at the peak of the 544 mM group.

The flattening of the curves at increasing levels of oxidative damage was expected as the number of pixels in each image at higher intensity values increased. More damaged specimens had stronger fluorescent signals in the pixels capturing regions of the sample that were more highly carbonylated. The increased in the number of saturated pixels was also expected and indicates that confocal microscopy imaging settings must be adjusted in future specimen imaging to reduce the number of saturated pixels in each specimen to zero. Saturated pixels represent fluorescent signals beyond the maximum range of intensity captured during imaging. As such, minimizing the number of saturated pixels retains the maximum amount of information in each image and imaging settings should be calibrated based on the sample with the highest pixel intensity.

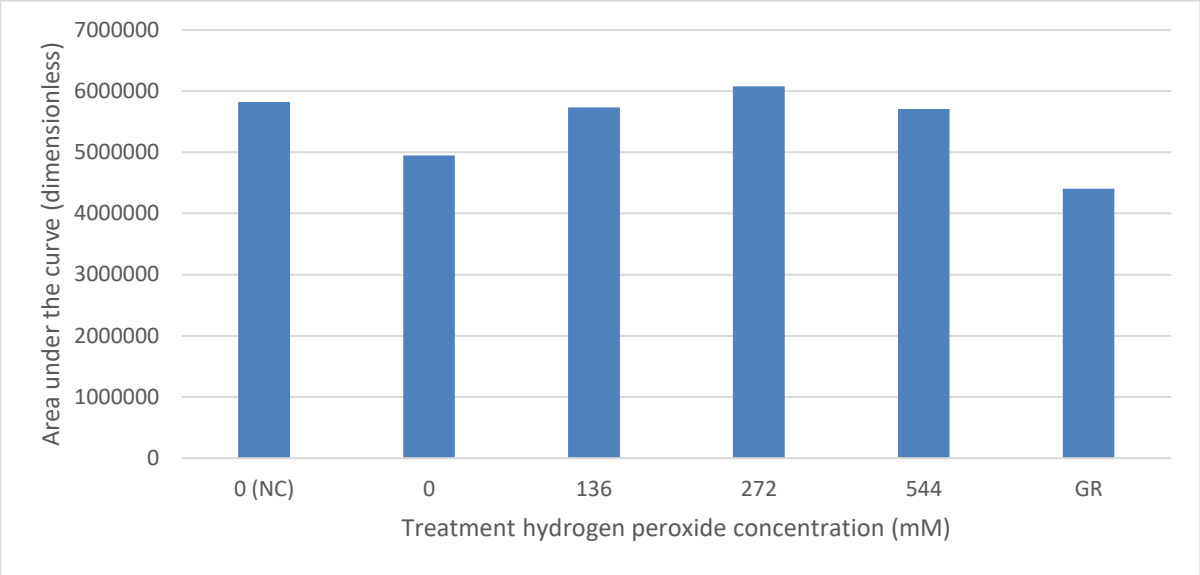

Figure 37 – Area under the curve for all groups (n = 1). GR: gamma irradiated controls; NC: no-catalyst controls.

Statistically significant differences between groups were unable to be ascertained due to the lack of replicates (n = 1). While two sets of replicates were imaged, the first was excluded from this analysis due to low pH values during treatment which could have damaged the bone in a confounding manner. The second set of replicates was excluded due to image acquisition issues, including sample movement, dehydration, and the use of coverslips when mounting samples on slides. Sample movement added dark artifacts to the corners of images where the signal was sharply attenuated by the confocal microscopy. Dehydration increased the sample's surface roughness, which on its own, could be compensated for by the use of the confocal z-stack. Dehydration in tandem with cover slip specimen mounting however, cause the middle of the samples to become too contorted and sharply attenuated by the confocal microscope, while the edges became compressed and artificially brighter. These factors caused these replicates to be excluded from this analysis.

The lack of statistical significance means that the noticeable and unexpected difference between the no catalyst 0 mM and 0 mM control groups in pixel intensity distribution may be resolved with replicates.

4.3 Limitations

One key discrepancy between the pore network model and the ROS soak experiment was the time specimens were exposed to H_2O_2. While reactive simulations reached steady state on the order of seconds to minutes, experimental bone beams were exposed to H_2O_2 for 96 hours, with reaction solutions replaced once the H_2O_2 reactant was exhausted. Despite the vast difference in exposure time, the simulation results were qualitatively validated by those from the experiments. This result is not unexpected, as once the pore concentrations throughout both systems reached steady state, heavily influenced by the fast reaction rate, no more H_2O_2 would diffuse deeper into the bone's volume. It is likely that the experimental system reached steady state long before the 96-hour timepoint point and that soaking for longer without any modifications to the procedure utilized would not increase uniformity of the H_2O_2 concentration gradient, and therefore oxidative damage gradient within the bone.

As a result, a more effective approach to achieve a uniform oxidative damage gradient within the bone samples would instead require reducing the rate of reaction and increasing the diffusive flux of H_2O_2 deeper into the network. The oxidative damage gradient is the product of the H_2O_2 concentration gradient and the amount of residence time that specific regions within the porous network are exposed to H_2O_2. Soaking bone specimens for longer would be expected to result in more carbonylation at these regions, and hence, stronger fluorescent signals. Due to transport limitations and the boundary conditions being located at the surfaces of the bone beams, the regions of the sample near these surfaces would experience the longest residence time and therefore accumulate the most oxidative damage. This means that even if the rates of diffusion and reaction are altered to deliver H_2O_2 quickly to the centre of the bone's volume, longer soak times may still result in an oxidative damage gradient, with the most damage accumulating near the surface of the beams.

Another key discrepancy between the pore network model and the ROS soak experiment was the presence of gas bubbles. Experimentally, the Fenton-like reaction of H_2O_2 with the transition metal ion catalyst produces oxygen gas in addition to the hydroxyl radical. This gas was observed to bubble up from the bone beams over their entire surface area throughout the experiment. Due to the accumulation of oxidative damage on the edges of specimens as observed in the gathered fluorescent images, the H_2O_2 must have also penetrated into the bone's porous network to this depth, decomposing and producing oxygen gas within the bone matrix, which then bubbled out. The gas bubbles were also assumed to provide enough mixing to the reaction solution for it to be considered

well mixed. In the pore network model, the system was assumed to be single phase liquid and the formation of a gaseous phase was not accounted for. The reason behind this assumption was that gas bubbles would have occupied space within the porous network, decreasing or altogether preventing diffusion of aqueously solvated species by reducing the available area for their diffusive flux. While simulation results were qualitatively validated by visualizing the oxidative damage gradient, it is likely that the evolution of oxygen gas within the experimental specimens further hampered the diffusion of H_2O_2 into the network beyond what the simulation predicted.

In analyzing the data while composing this thesis, one set of treatment replicates (0 mM – 544 mM) was rejected due to their fluorescent images showcasing bright and uniform signal akin to the gamma irradiated controls which clearly marked them as outliers from the other specimens in each group. All of the brighter more uniformly distributed images belonged to specimens from the first batch of experimental testing. During this test, the pH of the catalyst soaking solution was not strictly maintained at the desired pH 7.4 to avoid adverse and unpredictable effects on the bone samples. As a result, a white precipitate formed in the catalyst perfusion solution, and later during testing, the 544 mmol/L and 272 mmol/L beams shed a gelatinous pink "skin" during the hydrogen peroxide soaking step. In the second batch of experimental testing, the desired pH was maintained, and no such peeling "skin" was observed. It is possible that the specimens in batch 1 were unpredictably impacted by these inconsistencies and that those effects have manifested in the fluorescent images in this manner.

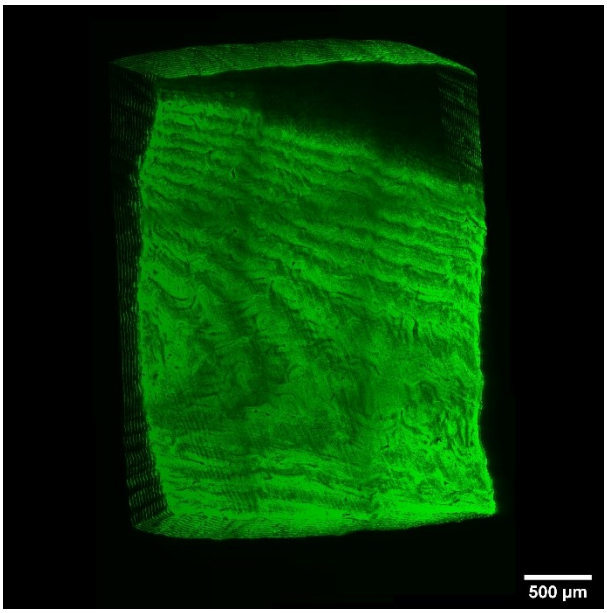

Figure 38 – Three-dimensional rendering of the surface of the stitched confocal image for the gamma irradiated control specimen, illustrating its curved morphology. Z-stack: 400.1 µm.

In the 0 mM and gamma irradiated confocal images, there are clear artifacts in the form of blacked out corners. These artifacts were due to the difficulty in imaging the curved surfaces of the slices. While normally rigid, once the surface of each bone slice was demineralized, the resulting biomaterial became softer and more

flexible, allowing it to take on curved geometries it otherwise would not. Figure 38 illustrates this using a three-dimensional rendering of the surface of the gamma irradiated positive control. The blackened top right corner is clearly just an attenuated portion of the surface that should normally exist but was inaccessible due to the surface's curvature.

An additional artifact was a tic-tac-toe board motif of darker pixels on the surface of nearly every single specimen. This artifact was caused by the specimens' movement during confocal imaging as each tile was taken. Future steps must be taken to reduce these image artifacts and avoid their hinderance on the actual intensity values of each pixel.

4.4 Overall Discussion

The lack of statistical significance between negative controls and treatment groups may also indicate that the differences in mean work to fracture, fracture toughness, and maximum displacement created as a result of the oxidative damage induced by the addition of $CoCl_2$ catalyst and varying levels of hydrogen peroxide may be too minute to be detected at this scale of study. Perhaps larger amounts of oxidative damage, not as extreme as gamma irradiation, but more severe than that in the present study, would assist in creating statistically significant differences in these quantities between negative and positive controls, and treated groups. This argument is corroborated by the fluorescent confocal microscopy images of beam cross sections, which indicated that the oxidative damage caused by $H_2O_{2(aq)}$ and $CoCl_2$ was localized to the beam's surface and did not penetrate deep into the bone's porous volume. This extremely localized and shallow oxidative damage may have not been enough to incur a statistically significant difference in work to fracture between treatment groups and negative controls.

The scarcity of information available in the literature on carbonyl levels in healthy and oxidatively damaged cortical bone presented a challenge in developing the reactive oxygen species soak and oxidative damage gradient staining techniques. Without established values of carbonylation, exact experimental parameters, including total soak time for bone specimens, had to be determined by trial-and-error. Current work in the Waterloo Composite Biomaterial Systems Lab conducted by Jindra Tupy aims to establish these benchmarks, providing foundation for the optimization of these techniques and further study of oxidative damage in cortical bone.

Chapter 5
Conclusions and Recommendations

5.1 Conclusions

A first-of-its-kind technique was developed to create controlled levels of oxidative damage in bovine cortical bone beams using free radicals generated from the decomposition of hydrogen peroxide (H_2O_2) using a Co^{2+} catalyst in aqueous solution at ambient temperature and pressure.

This system was modelling using a pore network modelling approach in OpenPNM, the first ever application of this technique to study transient reactive diffusion in bone, to determine concentration profiles of H_2O_2 within the bone's porous network. Results indicated that the decomposition reaction proceeded extremely fast, causing the greatest concentrations of H_2O_2 to exist at the surfaces of the bone specimens and limiting the diffusion of H_2O_2 into the bone to be essentially null. A sensitivity analysis of the reaction constant k determined that it would have to be reduced by 15 orders of magnitude to see an appreciable change in the internal H_2O_2 concentration.

Experimental study of the aqueous H_2O_2 system included exposing bovine cortical beams to controlled levels of oxidative stress via the *in situ* decomposition of H_2O_2 into toxic free radicals using $CoCl_2$ as a catalyst at conditions which matched the simulations. Positive oxidative damage controls were gamma irradiated specimens. Negative controls included a group which was not exposed to catalyst, and a group which was exposed to catalyst but not H_2O_2.

Load-displacement data indicated that gamma irradiated controls were noticeably more damaged via their much lower peak load and maximum deflection during fracture testing. Analysis of work to fracture and fracture toughness data revealed no statistically significant differences between groups and no statistically significant correlations with hydrogen peroxide concentration. Analysis of maximum deflection data also revealed no statistically significant differences or correlations. The large variation and lack of statistical significance in these analyses indicated that the study was underpowered, and more replicates were needed in each group. Analyses of the maximum displacement and chevron notch area data showed no statistically significant differences between all groups.

A novel fluorescent tissue staining technique was developed to visualize the oxidative damage gradient within the bone beams. Fluorescent imaging of the oxidative damage gradient was conducted

by staining slices excised near the centre of experimental specimen beams for carbonyls using FTC. Subsequently taken confocal microscopy images qualitatively mirrored pore network modelling results, depicting high concentrations of oxidative damage on samples' exposed surfaces, and relatively lower levels of damage in the interior. This qualitative validation provided a critical ink between the experimental and modelling components of this work which would have been unable to be obtained using current assay-based methods.

Analysing the mean pixel intensity distribution over the entire slices and only in their centres did not reveal and statistically significant differences between all groups. Pixel intensity distribution analysis suggested higher numbers of pixels at higher intensities for more oxidatively damaged specimens, but statistical significance was unable to be ascertained due to the lack of replicates.

Returning to this thesis' hypothesis, while bovine bone specimens were successfully treated with controlled and elevated levels of physiologically-relevant ROS, the resulting effect on the bone's fracture toughness was not detected. Despite a numerical difference in mean work to fracture and fracture toughness between gamma irradiated positive control specimens and all other group, no statistically significant differences between groups were detected and different concentrations of H_2O_2 did not result in statistically significant correlations with these quantities. As such, this study was unable to confirm oxidative stress and its associated oxidative damage as a mechanism of bone fragility.

While this study's hypothesis was not confirmed, its objectives were near completely met. Objective 1) was partially satisfied via the design and use of an aqueous *in vitro* model of controlled and elevated physiologically-relevant oxidative damage using bovine cortical bone as detailed in the Process Design and Assembly sections. While this model successfully created oxidative damage in bone specimens, it failed to create a uniform damage gradient throughout the bone beam's volume and did not cause damage capable of producing statistically significant differences between any of the analyzed quantities.

Objective 2) was satisfied by conducting the first ever pore network modelling of transient reactive diffusion within the bovine cortical bone beam specimens exposed to controlled levels of H_2O_2 in an aqueous system. The results of these simulations informed the design and execution of experiments on the same system, the results of which satisfied Objective 3) via qualitatively validated the

predicted concentration gradient within the bone by showing a similar oxidative damage gradient in experimental specimens.

This work provides important contributions to the study of oxidative stress and bone fragility in the form of a novel application of PNM to bone and new techniques for both causing and characterizing oxidative damage in tissues. These techniques may be applied to other biological materials and human tissues to address the paucity of much-needed foundational knowledge for the study of oxidative stress, damage, and tissue fragility in biological systems.

5.2 Recommendations

Examining the fracture testing method in relation to the fluorescent images, it is noted that for specimens oxidatively damaged in the bone soak experiment, there was a mismatch between the location of the crack tip and the regions of oxidative damage. Oxidative damage was most highly concentrated on the surface of the beam, while the tip of the chevron notch, and hence the tip of the crack, were located away from the edges and more towards the centre of the beam's cross-sectional area. This resulted in crack formation and the majority of the fracture surface area being created in undamaged tissue. Based on fracture testing results, this could have been a major confound of detecting any effects in fracture resistance in treated specimens. A more uniform damage profile throughout each beam's cross-section that allowed the tip of the chevron notch to be located within it, as seen in the gamma irradiated specimens, would likely have resulted in more pronounced differences between the untreated controls and treated specimens. It is also of note that improving the notching technique and consistency may still have a role to play in reducing the large variances seen in the fracture testing data.

Additionally, it was noted from analysis of the fluorescent oxidative damage gradient images that doing experiments on more osteonal bovine cortical bone, as opposed to the highly plexiform bone studied in this work, could allow for diffusion of H_2O_2 deeper into the bone's porous network on account of the presence of more highly conductive Haversian and Volkmann's canals. This may lead to a more uniform oxidative damage gradient. For this reason, study using more osteonal bovine cortical bone may also be more representative of H_2O_2 diffusion in human cortical bone.

Taking the results of fracture testing, modelling, and fluorescent imaging together, there is strong impetus for finding ways to significantly alter the balance between the rate of decomposition of H_2O_2 and its rate of diffusion into the porous network in order to achieve more uniform oxidative damage throughout the volume of the bovine cortical bone beam specimens. Options discussed included decreasing the system temperature to decrease the rate of reaction or utilizing a solvent with higher diffusivity (i.e., supercritical CO_2) to increase the rate of diffusion. Additionally, the total experimental runtime must likely be increased to enhance the penetrance of ROS into the bone and achieve uniformity of oxidative damage throughout the entire bone beam's volume, however excessive soaking time will likely still result in an oxidative damage gradient between the surface and central regions. A supercritical CO_2 process was designed, and the relevant equipment was procured as described in Appendix A to frame future investigation in this area.

With respect to pore network modelling, the network under study should be enlarged to $4.0 \text{ x } 4.0 \text{ x } 0.30 \text{ mm}^3$ in size to align more closely with experimental specimens. To reduce computational requirements, this may be accomplished by taking advantage of the symmetry present in the square slice and running the simulations on a $2.0 \text{ x } 2.0 \text{ x } 0.30 \text{ mm}^3$ network with boundary conditions configured in the same manner as those in the $2.4 \text{ x } 2.4 \text{ x } 0.30 \text{ mm}^3$ network studied here. Additionally, more natural variability may be added to the geometry of the pore network under study in the form of non-symmetric Volksmann's canals. While being more representative of the real tissue, this approach would significantly increase the computational requirements for simulation as the size of the network would need to be $4.0 \text{ x } 4.0 \text{ x } 0.30 \text{ mm}^3$ to capture the required level of asymmetric detail.

Pore network modelling may also be conducted depicting the diffusion of the catalyst out of the bone's porous network while the H_2O_2 diffuses in. This may reveal more representative concentration gradients which could shed further light on the mechanics of the diffusive transport occurring within specimens during the bone soak experiment.

As tortuosity was incredibly different to determine for the bovine cortical bone network due to the lack of literature values and correlations for this material and an arbitrary value was used, it is recommended to utilize correlations for materials similar to bovine cortical bone and to also conduct a parametric study to determine the influence of tortuosity on the time to steady state. It is noted that changes in tortuosity may appreciably impact time to steady state and is worthy of further study.

Finally with respect to modelling, pore network modelling of other solvents for the delivery of ROS deep within the bone's porous network valuable for predicting operation of analogous ROS soak experiments. Other solvents aside from H_2O, such as supercritical CO_2, may provide higher diffusive fluxes capable of combatting the fast H_2O_2 rate of reaction and delivering ROS deeper into the bone. Namely, it would be desired to predict the time it takes to reach a uniform concentration gradient of H_2O_2 within the bone while utilizing a new solvent, which may be used in itself as a screening tool for selecting new solvents.

Further analysis may be done on the bone specimens treated in this study to quantify the impact of the generated oxidative damage on the bone's collagen phase. Hydrothermal isometric tensile testing of portions of these beams would allow assessment of the collagen network's connectivity, which should decrease with increasing levels of oxidative damage due to peptide bond scission, leading to lower fracture toughness in the bone.

5.3 Contributions

The research presented in this thesis took fundamental steps towards establishing a link between oxidative stress, its associated damage, and bone fragility. This research featured the first-ever application of pore network modelling to the study of transient reactive diffusion in cortical bone. This modelling approach provided key insights which were used to develop a first-of-its kind method for generating oxidative damage using physiologically-relevant ROS *in vitro* within bovine cortical bone. To characterize this damage, a novel tissue staining technique was established using FTC to stain carbonyls and visualize the oxidative damage gradient within the tissue, a result which would have been impossible using current assay-based characterization methods. Additionally, a novel method to exceed the transport limitations in the previously mentioned *in vitro* technique was designed using supercritical CO_2, and the necessary equipment was procured, as described in Appendix A. Taken together, these techniques provide a fundamental basis for both causing and characterizing oxidative damage within biological tissues.

In the pursuit of developing and applying these methods, literature knowledge was compiled from diverse fields regarding ROS chemistry in biological systems, oxidative stress, the interaction of ROS with biomolecules and collagen, human and bovine cortical bone structure, oxidative damage in bone,

fracture mechanics, transport phenomena in porous media, and supercritical fluids. This comprehensive collection provided a much needed knowledge base for studying the impact of oxidative stress on cortical bone and will serve as an important resource for future study of this and other biological tissues.

Bibliography

1. Aspray TJ, Hill TR. Osteoporosis and the Ageing Skeleton. In: Harris JR, Korolchuk VI, editors. Biochemistry and Cell Biology of Ageing: Part II Clinical Science [Internet]. Singapore: Springer Singapore; 2019. p. 453–76. Available from: https://doi.org/10.1007/978-981-13-3681-2_16

2. Henrique P, Oliveira Limirio J, Barbosa P, Soares F, Tadashi E, Emi P, et al. Ionizing radiation and bone quality: time-dependent effects. [cited 2021 Jul 21]; Available from: https://doi.org/10.1186/s13014-019-1219-y

3. Napoli N, Chandran M, Pierroz DD, Abrahamsen B, Schwartz A V., Ferrari SL. Mechanisms of diabetes mellitus-induced bone fragility. Vol. 13, Nature Reviews Endocrinology. Nature Publishing Group; 2017. p. 208–19.

4. McNerny EMB, Nickolas TL. Bone Quality in Chronic Kidney Disease: Definitions and Diagnostics. Curr Osteoporos Rep. 2017;15(3):207–13.

5. Rachner TD, Coleman R, Hadji P, Hofbauer LC. Bone health during endocrine therapy for cancer. Lancet Diabetes Endocrinol [Internet]. 2018;6(11):901–10. Available from: https://www.sciencedirect.com/science/article/pii/S2213858718300470

6. Ong JCY, Gill JR, Parker MJ. Mobility after intertrochanteric hip fracture fixation with either a sliding hip screw or a cephalomedullary nail: Sub group analysis of a randomised trial of 1000 patients. Injury [Internet]. 2019;50(10):1709–14. Available from: https://www.sciencedirect.com/science/article/pii/S0020138319303602

7. Canada's Aging Population. Health Canada; 2002.

8. Mcglaason R, Zellermeyer V, MacDonald V, Lo N, Spafford D, McMullan JL, et al. National Hip Frctaure Toolkit - Guidelines [Internet]. Vol. 342, Bone and Joint Decade Canada. 2011. Available from: www.boneandjointcanada.com

9. Brieger K, Schiavone S, Miller FJ, Krause KH. Reactive oxygen species: From health to disease. Swiss Med Wkly. 2012;142(August):1–14.

10. Stadtman ER, Berlett BS. Reactive oxygen-mediated protein oxidation in aging and disease. Drug Metab Rev. 1998;30(2):225–43.

11. Dröge W. Free radicals in the physiological control of cell function. Physiol Rev. 2002;82(1):47–95.

12. Burton B, Gaspar A, Josey D, Tupy J, Grynpas MD, Willett TL. Bone embrittlement and collagen modifications due to high-dose gamma-irradiation sterilization. Bone [Internet]. 2014 Apr [cited 2020 Nov 11];61:71–81. Available from: http://dx.doi.org/10.1016/j.bone.2014.01.006

13. Nyman JS, Uppuganti S, Unal M, Leverant CJ, Adabala S, Granke M, et al. Manipulating the Amount and Structure of the Organic Matrix Affects the Water Compartments of Human Cortical Bone. JBMR Plus. 2019 Jun 1;3(6).

14. Gustafsson A, Wallin M, Khayyeri H, Isaksson H. Crack propagation in cortical bone is affected by the characteristics of the cement line: a parameter study using an XFEM interface damage model. Biomech Model Mechanobiol [Internet]. 2019;18(4):1247–61. Available from: https://doi.org/10.1007/s10237-019-01142-4

15. Torres-Del-Pliego E, Vilaplana L, Güerri-Fernández R, Diez-Pérez A. Measuring bone quality. Curr Rheumatol Rep. 2013;15(11).

16. Compston J. Bone quality: What is it and how is it measured? Arq Bras Endocrinol Metabol. 2006;50(4):579–85.

17. Harman D. Free radical theory of aging: An update - Increasing the functional life span. Ann N Y Acad Sci. 2006;1067(1):10–21.

18. Zioupos P, Currey JD, Hamer AJ. The role of collagen in the declining mechanical properties of aging human cortical bone. J Biomed Mater Res. 1999;45(2):108–16.

19. Zioupos P, Kirchner HOK, Peterlik H. Ageing bone fractures: The case of a ductile to brittle transition that shifts with age. Bone [Internet]. 2020;131(November 2019):115176. Available from: https://doi.org/10.1016/j.bone.2019.115176

20. Bedouhène S, Moulti-Mati F, Hurtado-Nedelec M, Dang PM-C, El-Benna J. Luminol-amplified chemiluminescence detects mainly superoxide anion produced by human neutrophils. Am J Blood Res [Internet]. 2017;7(4):41–8. Available from: http://www.ncbi.nlm.nih.gov/pubmed/28804681%0Ahttp://www.pubmedcentral.nih.gov/articlerender.fcgi?artid=PMC5545213

21. Grootveld M, Rhodes CJ. Methods for the Detection and Measurement of Reactive Radical Species in vivo and in vitro. In: Winyard PG, Blake DR, editors. Immunopharmacology of Free Radical Species. 1st ed. San Diego, CA: Academic Press; 1995. p. 1–18.

22. Hayyan M, Ali Hashim M, AlNashef IM. Superoxide Ion: Generation and Chemical Implications. Chem Rev [Internet]. 2016 [cited 2021 Jun 24];116(5):3029–85. Available from: https://pubs.acs.org/sharingguidelines

23. Florence TM. The production of hydroxyl radical from hydrogen peroxide. J Inorg Biochem. 1984;22(4):221–30.

24. Poundarik AA, Wu PC, Evis Z, Sroga GE, Ural A, Rubin M, et al. A direct role of collagen glycation in bone fracture. J Mech Behav Biomed Mater. 2015;52:120–30.

25. Saito M, Marumo K. Collagen cross-links as a determinant of bone quality: A possible explanation for bone fragility in aging, osteoporosis, and diabetes mellitus. Osteoporos Int. 2010;21(2):195–214.

26. Mauch L, Lun A, O'gorman MRG, Harris JS, Schulze I, Zychlinsky A, et al. Chronic Granulomatous Disease (CGD) and Complete Myeloperoxidase Deficiency Both Yield Strongly Reduced Dihydrorhodamine 123 Test Signals but Can Be Easily Discerned in Routine Testing for CGD. 2007 [cited 2021 Jul 4]; Available from: https://academic.oup.com/clinchem/article/53/5/890/5627456

27. Klopfleisch R, Jung F. The pathology of the foreign body reaction against biomaterials. Vol. 105, Journal of Biomedical Materials Research - Part A. John Wiley and Sons Inc.; 2017. p. 927–40.

28. Gautieri A, Passini FS, Silván U, Guizar-Sicairos M, Carimati G, Volpi P, et al. Advanced glycation end-products: Mechanics of aged collagen from molecule to tissue. Matrix Biol [Internet]. 2017;59:95–108. Available from: http://dx.doi.org/10.1016/j.matbio.2016.09.001

29. Sena LA, Chandel NS. Physiological roles of mitochondrial reactive oxygen species. Mol Cell. 2012;48(2):158–67.

30. Kanzaki H, Wada S, Narimiya T, Yamaguchi Y, Katsumata Y, Itohiya K, et al. Pathways that regulate ROS scavenging enzymes, and their role in defense against tissue destruction in periodontitis. Front Physiol. 2017;8(MAY).

31. Balasaheb Nimse S, Pal D. Free radicals, natural antioxidants, and their reaction mechanisms. 2015; Available from: www.rsc.org/advances

32. Burton GJ, Jauniaux E. Oxidative stress. Best Pract Res Clin Obstet Gynaecol [Internet]. 2011;25(3):287–99. Available from: http://dx.doi.org/10.1016/j.bpobgyn.2010.10.016

33. Winyard, Paul G., Blake, David R., Evans CH. Free Radicals and Inflammation. Winyard PG, Blake DR, Evans CH, editors. Vol. 53, Progress in Inflammation Research. Springer Basel, AG; 2000. 1689–1699 p.

34. von Zglinicki T. Aging at the Molecular Level [Internet]. Springer Netherlands; 2003. 248 p. Available from: http://link.springer.com/10.1007/978-94-017-0667-4

35. Méndez-Garrido A, Hernández-Rodríguez M, Zamorano-Ulloa R, Correa-Basurto J, Mendieta-Wejebe JE, Ramírez-Rosales D, et al. In vitro effect of H2O2, some transition metals and hydroxyl radical produced via fenton and fenton-like reactions, on the catalytic activity of AChE and the Hydrolysis of ACh. Neurochem Res. 2014;39(11):2093–104.

36. Drolet G, Dumbroff EB, Legge RL, Thompson JE. Radical scavenging properties of polyamines. Phytochemistry. 1986;25(2):367–71.

37. Hoffman PS, Pine L, Bell S. Production of superoxide and hydrogen peroxide in medium used to culture Legionella pneumophila: Catalytic decomposition by charcoal. Appl Environ Microbiol. 1983;45(3):784–91.

38. Brugmans MCP, Söntjens SHM, Cox MAJ, Nandakumar A, Bosman AW, Mes T, et al. Hydrolytic and oxidative degradation of electrospun supramolecular biomaterials: In vitro degradation pathways. Acta Biomater. 2015;27:21–31.

39. Gutteridge JMC, Wilkins S. Copper salt-dependent hydroxyl radical formation. Damage to proteins acting as antioxidants. Biochim Biophys Acta. 1983;759(1–2):38–41.

40. Gell DA. Structure and function of haemoglobins. Blood Cells, Mol Dis [Internet]. 2018;70(October 2017):13–42. Available from: https://doi.org/10.1016/j.bcmd.2017.10.006

41. Guengerich FP, Waterman MR, Egli M. Recent Structural Insights into Cytochrome P450 Function. Trends Pharmacol Sci [Internet]. 2016;37(8):625–40. Available from: http://dx.doi.org/10.1016/j.tips.2016.05.006

42. Kitajima N, Fukuzumi SI, Ono Y. Formation of superoxide ion during the decomposition of

hydrogen peroxide on supported metal oxides. J Phys Chem. 1978;82(13):1505–9.

43. Hawkins CL, Davies MJ. Oxidative damage to collagen and related substrates by metal ion/hydrogen peroxide systems: Random attack or site-specific damage? Biochim Biophys Acta - Mol Basis Dis. 1997;1360(1):84–96.

44. Weinstein J, Bielski BHJ. Kinetics of the Interaction of HO2 and O2 Radicals with Hydrogen Peroxide. The Haber-Weiss Reaction1 [Internet]. Vol. 101, Journal of the American Chemical Society. 1979 [cited 2021 Feb 24]. Available from: https://pubs.acs.org/sharingguidelines

45. Collin F. Molecular Sciences Chemical Basis of Reactive Oxygen Species Reactivity and Involvement in Neurodegenerative Diseases. [cited 2021 Feb 22]; Available from: www.mdpi.com/journal/ijms

46. Folkes LK, Candeias LP, Wardman P. Kinetics and mechanisms of hypochlorous acid reactions. Arch Biochem Biophys. 1995;323(1):120–6.

47. Giulivi C, Poderoso JJ, Boveris A. Production of nitric oxide by mitochondria. J Biol Chem. 1998;273(18):11038–43.

48. Laporte F, Doussiere J, Vignais P V. Respiratory burst of rabbit peritoneal neutrophils: Transition from an NADPH diaphorase activity to an ·O−2-generating oxidase activity. Eur J Biochem. 1990;194(1):301–8.

49. Darden AG, Ries WL, Wolf WC, Rodriguiz RM, Key LL. Osteoclastic superoxide production and bone resorption: Stimulation and inhibition by modulators of NADPH oxidase. J Bone Miner Res. 1996;11(5):671–5.

50. Yang S, Madyastha P, Bingel S, Ries W, Key L. A New Superoxide-generating Oxidase in Murine Osteoclasts. J Biol Chem [Internet]. 2001;276(8):5452–8. Available from: http://dx.doi.org/10.1074/jbc.M001004200

51. Chainy GBN, Dipak &, Sahoo K. Hormones and oxidative stress: an overview. 2019 [cited 2021 Jul 4]; Available from: https://doi.org/10.1080/10715762.2019.1702656

52. Lo YYC, Wong JMS, Cruz TF. Reactive oxygen species mediate cytokine activation of c-Jun NH2- terminal kinases. J Biol Chem. 1996;271(26):15703–7.

53. Levine AB, Punihaole D, Levine TB. Characterization of the role of nitric oxide and its clinical applications. Cardiology. 2012;122(1):55–68.

54. Bardaweel SK, Gul M, Alzweiri M, Ishaqat A, Alsalamat HA, Bashatwah RM. Reactive oxygen species: The dual role in physiological and pathological conditions of the human body. Eurasian J Med. 2018;50(3):193–201.

55. Yang Y, Bazhin A V, Werner J, Karakhanova S. Reactive Oxygen Species in the Immune System. Int Rev Immunol [Internet]. 2013 [cited 2021 Jul 18];32(3):249–70. Available from: https://www.tandfonline.com/action/journalInformation?journalCode=iiri20

56. Chen X, Song M, Zhang B, Zhang Y. Reactive Oxygen Species Regulate T Cell Immune Response in the Tumor Microenvironment. 2016 [cited 2021 Jul 4]; Available from: http://dx.doi.org/10.1155/2016/1580967

57. Boyle WJ, Simonet WS, Lacey DL. Osteoclast differentiation and activation. Nature. 2003;423(May):337–42.

58. Teitelbaum SL. Bone Resorption by Osteoclasts. Science (80-). 2000;289(September):1504–9.

59. Bax BE, Alam ASMT, Banerji B, Bax CMR, Bevis PJR, Stevens CR, et al. Stimulation of osteoclastic bone resorption by hydrogen peroxide. Biochem Biophys Res Commun. 1992;183(3):1153–8.

60. Chen X, Wang Z, Duan N, Zhu G, Schwarz EM, Xie C. Osteoblast–osteoclast interactions. Connect Tissue Res [Internet]. 2018;59(2):99–107. Available from: https://doi.org/10.1080/03008207.2017.1290085

61. Callaway DA, Jiang JX. Reactive oxygen species and oxidative stress in osteoclastogenesis, skeletal aging and bone diseases. J Bone Miner Metab [Internet]. 2015 Jul 23 [cited 2021 Feb 26];33(4):359–70. Available from: http://dx.doi.org/10.1007/s00774-015-0656-4

62. Sohal RS, Sohal BH. Hydrogen peroxide release by mitochondria increases during aging. Mech Ageing Dev. 1991;57(2):187–202.

63. Muller FL, Lustgarten MS, Jang Y, Richardson A, Van Remmen H. Trends in oxidative aging theories. Free Radic Biol Med. 2007;43(4):477–503.

64. Weber D, Davies MJ, Grune T. Determination of protein carbonyls in plasma, cell extracts, tissue homogenates, isolated proteins: Focus on sample preparation and derivatization conditions. Vol. 5, Redox Biology. Elsevier B.V.; 2015. p. 367–80.

65. Stadtman ER, Berlett BS. Reactive Oxygen-Mediated Protein Oxidation in Aging and Disease. Drug Metab Rev [Internet]. 1998 [cited 2021 Jan 31];30(2):225–43. Available from: https://www.tandfonline.com/action/journalInformation?journalCode=idmr20

66. Wolff SP, Garner A, Dean RT. Free radicals, lipids and protein degradation. Trends Biochem Sci. 1986;11(1):27–31.

67. Croce AC, Bottiroli G. Autofluorescence spectroscopy and imaging: a tool for biomedical research and diagnosis. Eur J Histochem. 2014;58:2461.

68. Balasaheb Nimse S, Pal D. Free radicals, natural antioxidants, and their reaction mechanisms. 2015 [cited 2021 Jul 19]; Available from: www.rsc.org/advances

69. Nash KM, Ahmed S. Nanomedicine in the ROS-mediated pathophysiology: Applications and clinical advances. Nanomedicine Nanotechnology, Biol Med [Internet]. 2015;11(8):2033–40. Available from: http://dx.doi.org/10.1016/j.nano.2015.07.003

70. Teissie J. Involvement of Reactive Oxygen Species in Membrane Electropermeabilization. In: Miklavcic D, editor. Handbook of Electroporation [Internet]. Cham: Springer International Publishing; 2017. p. 1–15. Available from: https://doi.org/10.1007/978-3-319-26779-1_40-1

71. Schiller J, Arnhold J, Schwinn J, Sprinz H, Brede O, Arnold K. Reactivity of Cartilage and Selected Carbohydrates with Hydroxyl Radicals: An NMR Study to Detect Degradation Products Reactivity of Cartilage and Selected Carbohydrates with Hydroxyl Radicals An NMR Study to Detect Degradation Products. Free Radic Res [Internet]. 2009 [cited 2021 Jun 24];28(2):215–28. Available from: https://doi.org/10.3109/10715769809065806

72. Nita M, Grzybowski A. The Role of the Reactive Oxygen Species and Oxidative Stress in the Pathomechanism of the Age-Related Ocular Diseases and Other Pathologies of the Anterior and Posterior Eye Segments in Adults. Oxid Med Cell Longev [Internet]. 2016 [cited 2021 Jun 24]; Available from: http://dx.doi.org/10.1155/2016/3164734

73. Berlett BS, Stadtman ER. Protein Oxidation in Aging, Disease, and Oxidative Stress. J Biol Chem [Internet]. 1997 [cited 2021 Jan 31];272(33):20313–6. Available from: http://www.jbc.org

74. Thomas CJ, Cleland TP, Sroga GE, Vashishth D. Accumulation of carboxymethyl-lysine (CML) in human cortical bone. Bone [Internet]. 2018;110:128–33. Available from:

https://doi.org/10.1016/j.bone.2018.01.028

75. Davies KJ. Protein damage and degradation by oxygen radicals. I. general aspects. J Biol Chem [Internet]. 1987;262(20):9895–901. Available from: http://dx.doi.org/10.1016/S0021-9258(18)48018-0

76. Stadtman ER, Levine RL. Free radical-mediated oxidation of free amino acids and amino acid residues in proteins. Amino Acids. 2003;25(3–4):207–18.

77. Schieber M, Chandel NS. ROS function in redox signaling and oxidative stress. Curr Biol [Internet]. 2014;24(10):R453–62. Available from: http://dx.doi.org/10.1016/j.cub.2014.03.034

78. Currey JD. The Mechanical Adaptations of Bones. New Jersey: Princeton University Press; 1984.

79. Rho JY, Kuhn-Spearing L, Zioupos P. Mechanical properties and the hierarchical structure of bone. Med Eng Phys. 1998;20(2):92–102.

80. Buehler MJ, Wong SY. Entropic elasticity controls nanomechanics of single tropocollagen molecules. Biophys J [Internet]. 2007;93(1):37–43. Available from: http://dx.doi.org/10.1529/biophysj.106.102616

81. Gautieri A, Buehler MJ, Redaelli A. Deformation rate controls elasticity and unfolding pathway of single tropocollagen molecules. J Mech Behav Biomed Mater [Internet]. 2009;2(2):130–7. Available from: http://dx.doi.org/10.1016/j.jmbbm.2008.03.001

82. Launey ME, Buehler MJ, Ritchie RO. On the Mechanistic Origins of Toughness in Bone [Internet]. Vol. 40, Annual Review of Materials Research. 2010 [cited 2020 Nov 11]. 25–53 p. Available from: http://www.annualreviews.org/doi/10.1146/annurev-matsci-070909-104427

83. Hoc T, Henry L, Verdier M, Aubry D, Sedel L, Meunier A. Effect of microstructure on the mechanical properties of Haversian cortical bone. Bone. 2006;38(4):466–74.

84. Manilay Z, Novitskaya E, Sadovnikov E, McKittrick J. A comparative study of young and mature bovine cortical bone. Acta Biomater [Internet]. 2013;9(2):5280–8. Available from: http://dx.doi.org/10.1016/j.actbio.2012.08.040

85. Cooper DML, Turinsky AL, Sensen CW, Hallgrímsson B. Quantitative 3D analysis of the canal network in cortical bone by micro-computed tomography. Vol. 274, Anatomical Record - Part B New Anatomist. Wiley-Liss Inc.; 2003. p. 169–79.

86. Langdahl B, Ferrari S, Dempster DW. Therapeutic Advances in Musculoskeletal Disease. Ther Adv Musculoskelet Dis [Internet]. 2016 [cited 2021 Jul 5];8(6):225–35. Available from: http://tab.sagepub.com

87. Wang X, Ni Q. Determination of cortical bone porosity and pore size distribution using a low field pulsed NMR approach. J Orthop Res. 2003;21(2):312–9.

88. Willett TL, Pasquale J, Grynpas MD. Collagen modifications in postmenopausal osteoporosis: Advanced glycation endproducts may affect bone volume, structure and quality. Curr Osteoporos Rep. 2014;12(3):329–37.

89. Woodside M, Willett TL. Elastic–plastic fracture toughness and rising JR-curve behavior of cortical bone is partially protected from irradiation–sterilization-induced degradation by ribose protectant. J Mech Behav Biomed Mater [Internet]. 2016;64:53–64. Available from: http://dx.doi.org/10.1016/j.jmbbm.2016.07.001

90. Tami AE, Schaffler MB, Knothe Tate ML. Probing the tissue to subcellular level structure underlying bone's molecular sieving function. Biorheology. 2003;40(6):577–90.

91. Gilles MA, Hudson AQ, Borders CL. Stability of water-soluble carbodiimides in aqueous solution. Anal Biochem. 1990;184(2):244–8.

92. Nagai R, Shirakawa J, Fujiwara Y, Ohno R, Moroishi N, Sakata N. Detection of AGEs as markers for carbohydrate metabolism and protein denaturation. J Clin Biochem Nutr. 2014;55(1):31–8.

93. Saito M, Marumo & K. Collagen cross-links as a determinant of bone quality: a possible explanation for bone fragility in aging, osteoporosis, and diabetes mellitus. Osteoporos Int. 2010;21(2):195–214.

94. Arakawa S, Suzuki R, Kurosaka D, Ikeda R, Hayashi H, Kayama T, et al. Mass spectrometric quantitation of AGEs and enzymatic crosslinks in human cancellous bone. Sci Rep. 2020 Dec 1;10(1).

95. Lee JS, Chung YS, Chang SY, Jung YS, Kim SH. Simple Quantification of Pentosidine in Human Urine and Plasma by High-Performance Liquid Chromatography. Int J Anal Chem. 2017;2017:0–5.

96. Ikeda K, Higashi T, Sano H, Jinnouchi Y, Yoshida M, Araki T, et al. N_-

(carboxymethyl)lysine protein adduct is a major immunological epitope in proteins modified with advanced glycation end products of the maillard reaction. Biochemistry. 1996;35(24):8075–83.

97. Gkogkolou P, Böhm M. Advanced glycation end products: Keyplayers in skin aging? Dermatoendocrinol. 2012;4(3):259–70.

98. Willett TL, Dapaah DY, Uppuganti S, Granke M, Nyman JS. Bone collagen network integrity and transverse fracture toughness of human cortical bone. Bone. 2019;120(July 2018):187–93.

99. Baek KH, Oh KW, Lee WY, Lee SS, Kim MK, Kwon HS, et al. Association of oxidative stress with postmenopausal osteoporosis and the effects of hydrogen peroxide on osteoclast formation in human bone marrow cell cultures. Calcif Tissue Int. 2010;87(3):226–35.

100. Gauthier R, Langer M, Follet H, Olivier C, Gouttenoire PJ, Helfen L, et al. 3D micro structural analysis of human cortical bone in paired femoral diaphysis, femoral neck and radial diaphysis. J Struct Biol [Internet]. 2018;204(2):182–90. Available from: https://doi.org/10.1016/j.jsb.2018.08.006

101. Törnquist E, Gentile L, Prévost S, Diaz A, Olsson U, Isaksson H. Comparison of small-angle neutron and X-ray scattering for studying cortical bone nanostructure. Sci Rep. 2020 Dec 1;10(1).

102. Lupsa BC, Isogna K. Bone Health and Osteoporosis. Endocrinol Metab Clin N Am. 2015;44:517–30.

103. Williams JG. Chapter 1 - Fracture Mechanics of Anisotropic Materials. In: Klaus F, editor. Application of Fracture Mechanics to Composite Materials, vol 6. Elsevier; 1989. p. 3–38.

104. Zehnder AT. Griffith Theory of Fracture. In: Wang QJ, Chung Y-W, editors. Encyclopedia of Tribology. Boston, MA: Springer US; 2013. p. 1570–3.

105. Griffith AA. The Phenomena of Rupture and Flow in Solids. Philos Trans R Soc London [Internet]. 1921;221:163–98. Available from: https://web.archive.org/web/20061016053324/http://www.cmse.ed.ac.uk/AdvMat45/Griffith20.pdf

106. Zimmermann EA, Launey ME, Ritchie RO. The significance of crack-resistance curves to the mixed-mode fracture toughness of human cortical bone. Biomaterials [Internet].

2010;31(20):5297–305. Available from: http://dx.doi.org/10.1016/j.biomaterials.2010.03.056

107. Pruitt L, Chakravartula A. Mechanics of Biomaterials: Fundamental Principles for Implant Design. Cambridge: Cambridge University Press; 2011.

108. Mouritz AP, editor. Fracture toughness properties of aerospace materials. In: Introduction to Aerospace Materials. 2012. p. 454–68.

109. ASTM. ASTM C1421 − 18: Standard Test Methods for Determination of Fracture Toughness of Advanced Ceramics at Ambient Temperature. ASTM Book of Standards. 2018.

110. Munz D, Bubsey RT, Srawley JE. Compliance and stress intensity coefficients for short bar specimens with chevron notches. Int J Fract. 1980;16(4):359–74.

111. Ritchie RO. Mechanisms of fatigue crack propagation in metals, ceramics and composites: Role of crack tip shielding. Mater Sci Eng. 1988;103(1):15–28.

112. Launey ME, Chen PY, McKittrick J, Ritchie RO. Mechanistic aspects of the fracture toughness of elk antler bone. Acta Biomater [Internet]. 2010;6(4):1505–14. Available from: http://dx.doi.org/10.1016/j.actbio.2009.11.026

113. Maghsoudi-Ganjeh M, Wang X, Zeng X. Computational investigation of the effect of water on the nanomechanical behavior of bone. J Mech Behav Biomed Mater [Internet]. 2020;101(June 2019):103454. Available from: https://doi.org/10.1016/j.jmbbm.2019.103454

114. Willett TL, Burton B, Woodside M, Wang Z, Gaspar A, Attia T. γ-Irradiation sterilized bone strengthened and toughened by ribose pre-treatment. J Mech Behav Biomed Mater [Internet]. 2015;44:147–55. Available from: http://dx.doi.org/10.1016/j.jmbbm.2015.01.003

115. Yeni YN, Kim DG, Dong XN, Turner AS, Les CM, Fyhrie DP. Do sacrificial bonds affect the viscoelastic and fracture properties of bone? Clin Orthop Relat Res. 2006;(443):101–8.

116. Willett T, Josey D, Lu RXZ, Minhas G, Montesano J. The micro-damage process zone during transverse cortical bone fracture: No ears at crack growth initiation. J Mech Behav Biomed Mater [Internet]. 2017;74(March):371–82. Available from: http://dx.doi.org/10.1016/j.jmbbm.2017.06.029

117. Zimmermann EA, Gludovatz B, Schaible E, Busse B, Ritchie RO. Fracture resistance of human cortical bone across multiple length-scales at physiological strain rates. Biomaterials [Internet]. 2014;35(21):5472–81. Available from:

http://dx.doi.org/10.1016/j.biomaterials.2014.03.066

118. Bird RB, Stewart WE, Lightfoot EN. Transport Phenomena. 2nd ed. New York: John Wiley and Sons Inc.; 2002.

119. Von D. A. G. Bruggeman. Berechnzcrrg verschCedcner physikalducher Eonstanten von heterogenew Yuhstan.xen 1. Ann Phys. 1935;5(24):636–64.

120. García-Salaberri PA, Zenyuk I V., Hwang G, Vera M, Weber AZ, Gostick JT. Implications of inherent inhomogeneities in thin carbon fiber-based gas diffusion layers: A comparative modeling study. Electrochim Acta [Internet]. 2019 Feb 1 [cited 2020 Nov 11];295:861–74. Available from: https://doi.org/10.1016/j.electacta.2018.09.089

121. Sadeghi MA, Aghighi M, Barralet J, Gostick JT. Pore network modeling of reaction-diffusion in hierarchical porous particles: The effects of microstructure. Chem Eng J. 2017;330(July):1002–11.

122. Gostick J, Aghighi M, Hinebaugh J, Tranter T, Hoeh MA, Day H, et al. OpenPNM: A Pore Network Modeling Package. Comput Sci Eng [Internet]. 2016 [cited 2020 Nov 11];18(4):60–74. Available from: https://ieeexplore.ieee.org/stamp/stamp.jsp?tp=&arnumber=7478437

123. Sadeghi MA, Agnaou M, Barralet J, Gostick J. Dispersion modeling in pore networks: A comparison of common pore-scale models and alternative approaches. J Contam Hydrol [Internet]. 2020 Jan 1 [cited 2020 Nov 11];228. Available from: https://doi.org/10.1016/j.jconhyd.2019.103578

124. Koretsky MD. Engineering and Chemical Thermodynamics. 2nd ed. John Wiley and Sons Inc.; 2013.

125. Dechema Chemistry Data Series [Internet]. Deutsche Gesellschaft für Chemisches Aparatewesen; 2004. Available from: https://dechema.de/en/CDS.html

126. Perry RH, Green DW. Perry's chemical engineers' handbook. 15th ed. New York: McGraw-Hill; 2008.

127. Lide DR, editor. CRC Handbook of Chemistry and Physics. 85th ed. Boca Raton, FL: CRC Press; 2004.

128. Suehiro Y, Nakajima M, Yamada K, Uematsu M. Critical parameters of {xCO2 + (1 - x)CHF3} for x = (1.0000, 0.7496, 0.5013, and 0.2522). J Chem Thermodyn.

1996;28(10):1153–64.

129. Carbon dioxide [Internet]. [cited 2021 Jul 20]. Available from: https://webbook.nist.gov/cgi/cbook.cgi?ID=C124389&Mask=4

130. Sahena F, Zaidul ISM, Jinap S, Karim AA, Abbas KA, Norulaini NAN, et al. Application of supercritical CO2 in lipid extraction - A review. J Food Eng [Internet]. 2009;95(2):240–53. Available from: http://dx.doi.org/10.1016/j.jfoodeng.2009.06.026

131. Muangrat R, Pongsirikul I. CyTA-Journal of Food Recovery of spent coffee grounds oil using supercritical CO 2 : Extraction optimisation and physicochemical properties of oil Rattana Muangrat & Israpong Pongsirikul Recovery of spent coffee grounds oil using supercritical CO 2 : Extraction optimisation and physicochemical properties of oil. CyTA-Journal Food [Internet]. 2019 [cited 2021 Jul 18];17(1):334–46. Available from: https://www.tandfonline.com/action/journalInformation?journalCode=tcyt20

132. Li S, Li Z, Dong Q. Diffusion coefficients of supercritical CO2 in oil-saturated cores under low permeability reservoir conditions. J CO2 Util [Internet]. 2016;14:47–60. Available from: http://dx.doi.org/10.1016/j.jcou.2016.02.002

133. Li S, Qiao C, Zhang C, Li Z. Determination of diffusion coefficients of supercritical CO2 under tight oil reservoir conditions with pressure-decay method. J CO2 Util [Internet]. 2018;24(March):430–43. Available from: https://doi.org/10.1016/j.jcou.2018.02.002

134. Wimmer Z, Zarevúcka M. A review on the effects of supercritical carbon dioxide on enzyme activity. Int J Mol Sci. 2010;11(1):233–53.

135. Aucoin MG, Legge RL. Effects of supercritical CO2 exposure and depressurization on immobilized lipase activity. Biotechnol Lett. 2001;23(22):1863–70.

136. Zhang J, Dalal N, Matthews MA, Waller LN, Saunders C, Fox KF, et al. Supercritical carbon dioxide and hydrogen peroxide cause mild changes in spore structures associated with high killing rate. J Microbiol Methods [Internet]. 2007;70:442–51. Available from: https://www.ncbi.nlm.nih.gov/pmc/articles/PMC3624763/pdf/nihms412728.pdf

137. Fages J. Viral inactivation of human bone tissue using supercritical fluid extraction. Vol. 44, ASAIO Journal. 1998. p. 289–93.

138. Fages J, Marty A, Delga C, Condoret JS, Combes D, Frayssinet P. Use of supercritical CO2

for bone delipidation. Biomaterials. 1994;15(9):650–6.

139. You L, Weikang X, Lifeng Y, Changyan L, Yongliang L, Xiaohui W, et al. In vivo immunogenicity of bovine bone removed by a novel decellularization protocol based on supercritical carbon dioxide. Artif Cells, Nanomedicine Biotechnol [Internet]. 2018;46(sup2):334–44. Available from: https://doi.org/10.1080/21691401.2018.1457044

140. Nguyen H, Cassady AI, Bennett MB, Gineyts E, Wu A, Morgan DAF, et al. Reducing the radiation sterilization dose improves mechanical and biological quality while retaining sterility assurance levels of bone allografts. Bone [Internet]. 2013;57(1):194–200. Available from: http://dx.doi.org/10.1016/j.bone.2013.07.036

141. Russell NA, Rives A, Pelletier MH, Bruce WJ, Walsh WR. The effect of sterilization on the mechanical properties of intact rabbit humeri in three-point bending, four-point bending and torsion. Cell Tissue Bank. 2013;14(2):231–42.

142. Russell N, Rives A, Pelletier MH, Wang T, Walsh WR. The effect of supercritical carbon dioxide sterilization on the anisotropy of bovine cortical bone. Cell Tissue Bank. 2015;16(1):109–21.

143. Mitton D, Rappeneau J, Bardonnet R. Effect of a supercritical CO2 based treatment on mechanical properties of human cancellous bone. Eur J Orthop Surg Traumatol. 2005;15(4):264–9.

144. Tresguerres FGF, Torres J, López-Quiles J, Hernández G, Vega JA, Tresguerres IF. The osteocyte: A multifunctional cell within the bone. Ann Anat [Internet]. 2020;227:151422. Available from: https://doi.org/10.1016/j.aanat.2019.151422

145. Soysa NS, Alles N. Osteoclast function and bone-resorbing activity: An overview. Biochem Biophys Res Commun [Internet]. 2016;476(3):115–20. Available from: http://dx.doi.org/10.1016/j.bbrc.2016.05.019

146. Schumb WC, Satterfield CN, Wentworth RL. Hydrogen Peroxide. New York: Reinhold Publishing Corporation; 1955.

147. PubChem. Hydrogen peroxide [Internet]. 2019 [cited 2019 Nov 4]. Available from: https://pubchem.ncbi.nlm.nih.gov/compound/784

148. Malek K, Coppens M-O. Effects of Surface Roughness on Self- and Transport Diffusion in

Porous Media in the Knudsen Regime. Phys Rev Lett [Internet]. 2001 Aug 31;87(12):125505. Available from: https://link.aps.org/doi/10.1103/PhysRevLett.87.125505

149. Mohanty JG, Bhamidipaty S, Evans MK, Rifkind JM. A fluorimetric semi-microplate format assay of protein carbonyls in blood plasma. Anal Biochem [Internet]. 2010;400(2):289–94. Available from: http://dx.doi.org/10.1016/j.ab.2010.01.032

150. Z-functions [Internet]. [cited 2021 Jul 15]. Available from: https://imagej.net/imaging/z-functions#Maximum_Intensity_Z-projection

151. Martin RB, Burr DB. Structure, function, and adaptation of compact bone. New York: Raven Press; 1989.

152. Dalle-Donne I, Rossi R, Giustarini D, Milzani A, Colombo R. Protein carbonyl groups as biomarkers of oxidative stress. Clin Chim Acta. 2003;329(1–2):23–38.

153. Levine RL, Williams JA, Stadtman EP, Shacter E. Carbonyl assays for determination of oxidatively modified proteins. Methods Enzymol. 1994 Jan;233(C):346–57.

154. Ng M. Cell Permeabilization Using Supercritical Carbon Dioxide. University of Waterloo; 2001.

155. During A. Lipid determination in bone marrow and mineralized bone tissue: From sample preparation to improved high-performance thin-layer and liquid chromatographic approaches. J Chromatogr A [Internet]. 2017;1515:232–44. Available from: http://dx.doi.org/10.1016/j.chroma.2017.08.004

Appendix

Appendix A Supercritical Carbon Dioxide Process Design

This appendix describes the work undertaken to design an *in vitro* supercritical carbon dioxide process for use in simulating oxidative stress in cortical bone specimens using hydrogen peroxide. This appendix also includes the Process Flow Diagrams, Piping & Instrumentation Diagrams, and Bill of Materials for the designed process.

A.1 Process Design and Assembly

A.1.1 Process type

A batch process was selected by considering available equipment, limited resources, and the size of the specimens to be treated. A high-pressure Parr reactor was available in the laboratory, which had previously been used for a supercritical CO_2 batch process for permeabilizing cell membranes (154). The previous project had utilized a batch process to expose samples to solvent for a specified amount of time at given conditions. This approach was continued in the present work and had the advantage of also minimizing the amount of solvent compared to continuous processes. With regards to specimen size, this thesis focused on cortical bone beams with dimensions 4 x 4 x 50 mm to align with relevant ASTM standards for 3- and 4-point bending fracture testing, however other specimen sizes and geometries could be used (109). The number of specimens that can be treated at a given time depends on the size of both the specimens and the reactor. The chosen batch process is outlined in Figure 3.

A.1.2 Oxidative damage simulation

The selected reactive oxygen species to simulate oxidative stress was hydrogen peroxide (H_2O_2), an ROS present abundantly in the body and capable of being decomposed into toxic free radicals by physiologically-relevant catalysts, including enzymes such as superoxide dismutase, and metal ions, such as Fe^{2+} and Fe^{3+} (23,37). The selected catalyst was cobalt (II) chloride ($CoCl_2$) for its ability to catalyze the Fenton-like decomposition of H_2O_2 into the toxic hydroxyl radical ($\dot{}OH$) and oxygen (O_2) (35).

The selected solvent was supercritical carbon dioxide ($SCCO_2$). Widely known for its use in decaffeinating coffee and in oil recovery (132,133), the use of $SCCO_2$ in the sterilization (136,141,142) and delipidation (138) of biomaterials and biological tissues has become more common in recent years. $SCCO_2$ is inert in biological systems and combines the high diffusivity of gas phase CO_2 with the density near that of liquid CO_2. This allows $SCCO_2$ to penetrate deeply into the porous structures of biomaterials, solubilize lipids and other chemicals within, and remove them from the material. The low critical point ($32°C, 73\ bar$) protects tissues from temperature related damage, although some issues have been noted in the tissue banking industry with regards to soft tissues and damage caused by the depressurization following treatment. With respect to the inherent diffusion limits of human cortical bone (300 Da) (90), CO_2's small molecule size (44 Da) is another inherent advantage in diffusing through its porous structure.

It should be noted that further testing is required to confirm whether the mixture of H_2O_2, H_2O (due to the aqueous H_2O_2 solution), $CoCl_2$, and $SCCO_2$ performs favorably in the supercritical batch process and can induce uniform oxidative damage in specimens without causing undue safety risks due to overpressure.

A.1.3 Process Flow Description

The following description is for the process flow drawings 100-PFD-001/A to G, which can be found at the end of this appendix. Safety devices, instrumentation, and detailed specifications are depicted in the piping & instrumentation diagrams (P&IDs) and bill of materials described in the following sub-sections.

100-PFD-001 depicts the overall process flow. Gas cylinders TK-001 and TK-002 dispense research-grade and supercritical-grade carbon dioxide respectively via CO_2 regulators V-01 and V-02. Streams S01 and S02 intersect via three-way valve, V-03, to form S03, the CO_2 supply stream for the supercritical reactor R-001. V-04 provides CO_2 inlet isolation for R-001. H_2O_2 is supplied to R-001 via TK-003. This tank is a placeholder for any vessel or syringe used to introduce H_2O_2 into the system as a feed for high-pressure piston pump P-001. This pump discharges H_2O_2 into R-001 via the inlet isolation valve V-05. The outlet of R-001 vents into a fume hood and can be isolated via valve V-06.

100-PFD-001A/B/C/D/E describe process flow during process start up after specimens have been installed within R-001. 100-PFD-001A depicts the process for purging the reactor and tubing with research-grade CO_2. Vapor phase CO_2 flows from TK-001 through R-001 and is discharged into the fume hood. The three-way valve V-03 is configured to allow flow from TK-001 to R-001 and block flow in S02. Additionally, V-05 is used to isolate the H_2O_2 inlet stream S06 during purge. This purge is completed to remove air from the system prior to startup.

100-PFD-001B depicts the process for purging the reactor and tubing with liquid-phase supercritical-grade CO_2. This purge is done identically to the previous, with the key exception being the altered position of V-03 and the phase of the CO_2. Initially, the CO_2 will be in the vapor phase and will become liquid as the system cools down towards the end of this purge step. Purging with supercritical-grade CO_2 is done to further flush out any impurities from the system. Supercritical-grade CO_2 is higher purity than research-grade. It is worth noting that this second purge step can be skipped if research-grade CO_2 will be used for the remaining startup and steady-state operations. This also allows TK-002, V-02, and S02 to be omitted from the design altogether if users intend to only use research-grade CO_2.

100-PFD-001C illustrates filling R-001 with liquid supercritical-grade CO_2. During this start up step, the outlet valve V-06 is closed. R-001 will be only partially filled with liquid CO_2 to avoid overpressure while heating the reactor to generate vapor and build pressure in the final start up step.

100-PFD-001D shows the injection of aqueous H_2O_2 using P-001. V-04 is closed to isolate the CO_2 inlet while V-05 is opened to allow the passage of H_2O_2. V-06 remains closed. The volume of aqueous H_2O_2 injected depends on the desired H_2O_2 concentration for the given batch.

100-PFD-001E depicts the final start up step: heating and pressurizing of R-001. Heating is done to produce vapor from the liquid CO_2, which in turn rapidly increases the pressure. Both of R-001's inlets are isolated, and pressure is controlled via its outlet valve V-06. Temperature and pressure are increased until they surpass the mixture's critical point.

100-PFD-001F describes the steady state operation of the batch process where specimens are exposed to *in vitro* oxidative stress. Once the mixture within R-001 reaches the supercritical state, the temperature and pressure are maintained for the duration of steady state operation. Temperature and pressure control are detailed in the following P&ID sub-section. The length of time specimens are

exposed to the mixture depends on the desired oxidative damage gradient and the desired extent of oxidative damage.

100-PFD-001G outlines the shutdown of the process. V-06 is opened wider to depressurize the system. The desired rate of depressurization must be determined experimentally, although literature sources using $SCCO_2$ for tissue sterilization depressurized over 40 – 60 minutes (141).

A.1.4 Process & Instrumentation Description

The following description is for piping and instrumentation (P&ID) drawings 100-PID-000 (P&ID legend) and 100-PID-001/2, which can be found at the end of this appendix. All piping shown is 1/8 in. diameter stainless steel tubing with 0.028 in wall thickness, with the exception of the reactor R-001's outlet, which is 1/4 in. diameter.

100-PID-001 depicts the Feeds Zone, the piping and instrumentation for the equipment where the solvent (CO_2) and ROS (H_2O_2) enters the process. TK-001 contains research-grade CO_2 for use in purging the system during start up. TK-002 contains supercritical-grade CO_2 for use during steady state process operation. Regulators V-01 and V-02 are connected to both tanks. Outlet streams from these regulators connect at three-way valve V-03, which is used to allow CO_2 to flow into the process from the desired tank while blocking back-flow into the adjacent stream. Downstream of V-03 is pressure safety valve PSV-01, which is suitable for CO_2 and low temperature service. Its set pressure is low enough to protect tubing and connectors upstream. In the event it activates, PSV-01 discharges into the fume hood. It is worth noting that if operators decide to instead use research-grade CO_2 for operation, TK-002, V-02, S02, and V-03 may be omitted from the setup altogether.

TK-003 is the placeholder vessel representing the H_2O_2 supply. This tank may be an actual vessel, a syringe, or another container deemed safe and appropriate. TK-003 feeds high-pressure pump P-001, which is used to inject H_2O_2 into the pressurized reactor R-001 (100-PID-002) during startup. P-001 is a piston pump (positive displacement) and therefore needed overpressure protection downstream in the form of PSV-02 to protect the asset and ensure process safety. PSV-02 is suited for H_2O_2 service and has a set pressure low enough to protect equipment upstream.

100-PID-002 illustrates the Reactor R-001 inlet and outlet. The CO_2 inlet stream S03 and the H_2O_2 inlet stream S06 (from 100-PID-001) pass through inlet isolation valves and connect with the high-

pressure reactor R-001. Four ports are present in the lid of R-001. Two of these ports are used as inlets for CO_2 (S04) and H_2O_2 (S07) which allows these fluids to directly enter the reaction chamber.

One of the remaining ports in R-001's lid allows the insertion of type-T thermocouple TT-001 for temperature measurements. TT-001A connects via electrical wiring to digital temperature indicator and controller TIC-001A, which compares the measured reactor temperature with the user-input setpoint and switches electrical heating tape EHT-001 on and off to maintain that set temperature. The 'A' at the end of the thermocouple and temperature controller labels indicates the control loop for each instrument. There is only one temperature control loop in this system corresponding to the label 'A.'

The final port in R-001's lid is for the reactor outlet, which exhausts the reactor's fluid and dissolved lipid contents into the fume hood. Mounted on the outlet, immediately downstream of R-001 is rupture disk RD-001 which will burst at a set pressure of $2033.50\ psig$ at $72°F$ to prevent overpressure of the reactor, protecting the operator's safety and the asset. Moving slightly further downstream on the reactor outlet, pressure gauge PI-001 allows the operator to view the pressure within R-001 in real time. Pressure control in R-001 is executed manually by the operator by adjusting the position of V-06 to maintain the desired reactor pressure by venting some of the mixture within to the fume hood.

Within the reactor vessel itself, specimens are supported by perforated stainless steel platform PFT-001, which allows circulation of the reaction mixture on all sides of the specimens while preventing them from contacting the magnetic stir bar MSB-001 located on the chamber's bottom. MSB-001 is controlled via magnetic stir plate STP-001, upon which the reactor is placed. Sight glasses SG-001/2 allow direct visualization by the operator of the mixture within the reactor, allowing for confirmation of the supercritical state once the initially clear mixture becomes cloudy near the critical point and then clear again beyond it.

A.1.5 Equipment procurement

This section details the process used for selecting equipment to purchase.

A.1.5.1 In-house process

Please refer to the Bill of Materials document and process drawings found at the end of this appendix for equipment details. The total equipment cost of the in-house process was $5,556.55 CAD.

The high-pressure reactor R-001, magnetic stir bar MSB-001, H_2O_2 supply vessel TK-003, high-pressure piston pump P-001, type-T thermocouple TT-001A, pressure gauge PI-001, rupture disk RD-001, CO_2 regulator V-01, and Parr-to-Swagelok adapter fittings were readily available within the laboratory. Additionally, the piston pump was repurposed from an HPLC machine and successfully leak tested at $2000\ psig$ without incident.

The remaining valves, tubing, and fittings were selected from the Swagelok catalog to match the P&ID's specifications. All items were stainless steel to avoid corrosion when exposed to H_2O_2. As liquid CO_2 was initially used to fill the reactor during the startup phase, tubing and valves upstream of R-001 and downstream of both CO_2 tanks were selected for cold (-23°C and below) service. In the case of valves, this was largely determined by the material used for the valve seats, which was selected under advisement of the Swagelok sales representative for best operation and safety practices.

A backpressure regulator was also included on the bill of materials but omitted from the P&IDs. Backpressure regulator valves allow for the maintenance of a setpoint pressure via the release of vapor once the pressure exceeded the setpoint. This piece of equipment was determined to be advantageous, as the designed reactor pressure control loop involved manual operator manipulation of V-06 to maintain R-001's pressure setpoint. The backpressure regulator was considered an accessory that may be included in the order should funds become available for its purchase. Additionally, an outlet filter for the backpressure regulator was also included in the bill of materials to protect the asset from lipids and other solid particulate exiting the reactor. Lipids are commonly extracted from many materials, such as coffee beans, using supercritical CO_2, and it is reasonable to suggest that the lipids present in bovine cortical bone samples would be no exception (130,131,155). Clogging of the backpressure regulator valve could lead to the overpressure of R-001, posing a significant safety risk which would have to be mitigated by the use of rupture disk RD-001.

CO_2 cylinders were selected from Praxair. The cylinder for TK-001 was selected as research-grade CO_2, while the cylinder for TK-002 was selected as supercritical extraction grade. Referring to the process flow diagrams at the end of this appendix, supercritical extraction grade was selected as a high purity solvent for use in the batch process while treating specimens. The research-grade CO_2 would be used to purge the system in the vapor phase and therefore would be consumed consistently

prior to system start up. As a result, it was desired to use a grade of CO_2 with a purity similar to supercritical grade but which was also less expensive for purging the system.

Temperature control loop equipment were purchased from Cole-Parmer. A temperature indicator and controller compatible with the laboratory's type T thermocouple and capable of maintaining reactor temperature at 37°C was selected from the Cole-Parmer catalog for TIC-001A. Additionally, an electric heating tape compatible with this temperature controller was selected for EHT-001 to act as the heating element. The length and width of the heating tape were selected to allow it to completely wrap around the reactor chamber's exterior while minimizing cost and taking into account electrical safety concerns. As the exterior of the reactor was stainless steel, it was desired to purchase an electrical heating tape that did not allow the conduction of electricity from itself to other metals it was in contact with.

In order to ensure that liquid CO_2 was able to flow to the reactor from TK-002 without vaporizing, it was important to minimize the pressure drop between TK-002 and R-001. Under advisement from Praxair technical experts, no pressure regulator would be purchased for V-02 and instead the tank would be directly connected to three-way valve V-03 and isolated using its own valve present on the cylinder. A regulator for TK-002 was included as V-02 in the bill of materials in the event it would be required in the future, however it was not factored into the total equipment cost calculation.

This approach of connecting the full gas cylinder pressure directly to the process presented some significant safety considerations. Firstly, the pressure of the CO_2 flow would match that of the cylinder (830 psig), which would impose significant stress in a sudden manner on the piping, valves and fittings once the main cylinder valve was opened. This sudden impact, while most likely not being as severe as extreme cases of other types of fluid hammer in processes, such as water hammer, still contained the potential to jar loose and defective components apart, releasing CO_2 into the laboratory and causing the potential for metal shrapnel and projectiles to be hurled at bystanders.

The second major problem with this approach is that it did not guarantee that the CO_2 would remain in the liquid phase after exiting the tank. More likely, the downstream piping and fittings would have to be chilled to maintain the liquid phase. This meant that initially, the liquid CO_2 from the cylinder would flash, chilling the immediate environment. Praxair technical experts advised that water ice and frost often form on the outside of tubing through which CO_2 is flowing during this stage. Additionally, the risk existed that the immediate environment surrounding the CO_2 would be chilled to such an extreme degree that solid CO_2 could form. This would pose a new hazard, as solid CO_2

particulate could become lodged in downstream tubing, valves, and fittings, creating a risk for system overpressure.

To reliably mitigate this risk while still delivering liquid CO_2 to the reactor, it was determined that a high-pressure pump would be required on the outlet of TK-002. The increase in pressure provided by this pump would maintain CO_2 in the liquid phase, even at ambient temperatures, thereby negating the risks of solid CO_2 formation, and its related potential for overpressure, within the process. While several pumps existed on the market for CO_2 service, their addition to the total equipment cost ($1500 - $2000 CAD) was non-trivial, pushing the total equipment cost to approximately $7500 CAD.

While evaluating options for high-pressure liquid CO_2 pumps, the author became aware of a commercially available system for biomaterial sterilization which utilized supercritical CO_2 and followed a nearly identical process design to that developed and described in this thesis. The cost of the commercial system was comparable to the equipment cost of the in-house process including the high-pressure liquid CO_2 pump but offered the chance to use a system proven commercially to be safe for operation. It was therefore decided to not purchase any equipment for the in-house process and instead pivot to purchasing this third-party process. Details of the third-party process are discussed in more detail in the following subsection.

A.1.5.2 Third-party process

Stemming from safety risks associated with the assembly and operation of the in-house process for treating bovine cortical bone beams with supercritical CO_2 and H_2O_2, a process of incredibly similar design was discovered commercially available from NovaSterilis (Lansing, NY). NovaSterilis is a company which specializes in producing biomaterial sterilization systems that utilize supercritical CO_2 and their own sterilant (peracetic acid, H_2O_2, and other antimicrobial ingredients). Their systems are in use worldwide, including in labs at the forefront of supercritical CO_2 sterilization/treatment of bone and at tissue banking facilities, including Héma-Québec (141). While efficacy is still being assessed, this sterilization approach seems to be detrimental to soft tissues, while having limited effects on hard tissues such as bone, at least to the extent of the analyses which have been done (142).

The system most similar to the designed *in vitro* model presented in this thesis was their NovaGenesis model, which utilized nearly all of the same types of equipment including a high-pressure reactor, rupture disk, temperature control, magnetic stirring, and instrumentation with the addition of a high-

pressure liquid CO_2 pump which fed the reactor. Batch process flow follows a similar path as the in-house process, with the key exception of omitting the CO_2 purge step altogether.

While other commercial systems for supercritical CO_2 sterilization were considered, the similarity between the designed in-house process and the NovaGenesis system provided clearer justification for the purchase of this system and greater confidence in its ability to effectively create oxidative damage in bovine cortical bone specimens.

While the NovaGenesis system mitigated the safety issues of the in-house process, it introduced new complications in operation. The high-pressure reactor utilized in this setup did not possess quartz windows through which the achievement of a supercritical state could be confirmed within the reactor. This meant that when operating this system, the operator would have to trust that their operating conditions were sufficiently elevated to maintain the sterilant-solvent mixture above its critical point. As previously mentioned, the NovaGenesis system did not allow for purge with vapor-phase CO_2 prior to startup to remove any air and other gases within the reactor and tubing. This creates the opportunity for these other species to be part of the mixture in the reactor during treatment, which would alter the thermodynamics of the mixture and change its critical point. The lack of visual confirmation would make it impossible to ascertain the phase of the system and troubleshoot these errors.

Another key issue was that the addition of sterilant was done at the same time as the specimens were added into the reactor. Following addition, the reactor was sealed and liquid CO_2 would be pumped into the reaction chamber to start the treatment process. This procedure would cause samples to be exposed to the sterilant for longer than the desired treatment time while the mixture was at the supercritical state and could bias results by causing oxidative damage on the outer surfaces of the specimen during this residence time. Additionally, if a purge step were to be incorporated, the vast majority of the sterilant would be blown through the reactor, leaving the system and preventing samples from being successfully treated.

Taking these limitations into account, the author reached out to NovaSterilis and, after multiple meetings, proposed custom modifications to their commercial process. The main modification was to the high-pressure reactor itself. The NovaGenesis system's reactor typically has two ports on its lid, one which functioned as the liquid CO_2 inlet and mixture outlet and another which allowed passage of the thermocouple into the reaction chamber. The proposed change was to add two additional ports, one for the purpose of purging the system with vapor-phase research-grade CO_2 and another to allow

for the injection of H_2O_2 using a high-pressure pump. Utilizing these four ports, the reactor could be effectively purged during startup and remain isolated from the environment while being filled with liquid CO_2 and H_2O_2, allowing for a greater degree of confidence that the supercritical state would actually be achieved during sample treatment. The addition of these two ports also brought the NovaGenesis' reactor more in line with the reactor in the in-house process (See drawing 100-PID-002). NovaSterilis agreed to these modifications at a cost of approximately $450 USD for each additional reactor port and the addition of weeks to the lead time for the device. It should be noted that the ongoing COVID-19 pandemic likely added delays to the underlying supply chain in securing materials and parts to complete these modifications.

ASME certification was requested for the high-pressure reactor and electrical certification was requested for the entire NovaGenesis unit. To operate in line with University of Waterloo policies, electronics in use on university campuses must have CSA Group (formerly the Canadian Standards Association; CSA) or Underwriter Labs (UL) certification or pass an Electrical Safety Authority (ESA) inspection. NovaGenesis was able to procure the ASME certification but was unable to procure either of these electronic certifications at their facility in the United States. An agreement was reached to conduct an ESA electrical inspection at the University of Waterloo and lease the NovaGenesis system on a rent-to-own basis to mitigate the financial risk of purchasing a piece of laboratory equipment which may not be usable.

Unfortunately, the NovaGenesis system failed the electrical inspection at the University of Waterloo, significantly delaying its usage in the laboratory. The failure was on account of the Pelican case used to house the system not being fireproof. An agreement was reached to swap out this case for a metal box which would mitigate the risk of fire hazard. The system was shipped back to the University of Waterloo following this modification and passed the electrical inspection after the submission of this thesis. Future experiments utilizing the NovaGenesis system will be forthcoming outside of the scope of this thesis and offer an exciting opportunity to create uniform oxidative damage deep within bone specimens as well as modify internal microstructure.

One key limitation of the NovaGenesis system was the lack of sight-glasses for visually confirming the supercritical state of the mixture within the reactor. While the critical point of pure $CO_2$is well established, the critical point for the mixture of CO_2, H_2O_2, H_2O, and bone lipids has not yet been characterized. As a result, the system may not be operating in the supercritical phase and further experiments need to be conducted to determine operating temperature and pressure for the system.

A.1.6 Process Drawings and Bill of Materials

This section includes the process flow diagrams (PFD), piping & instrumentation diagrams (P&ID), and Bill of Materials for the designed supercritical carbon dioxide process.

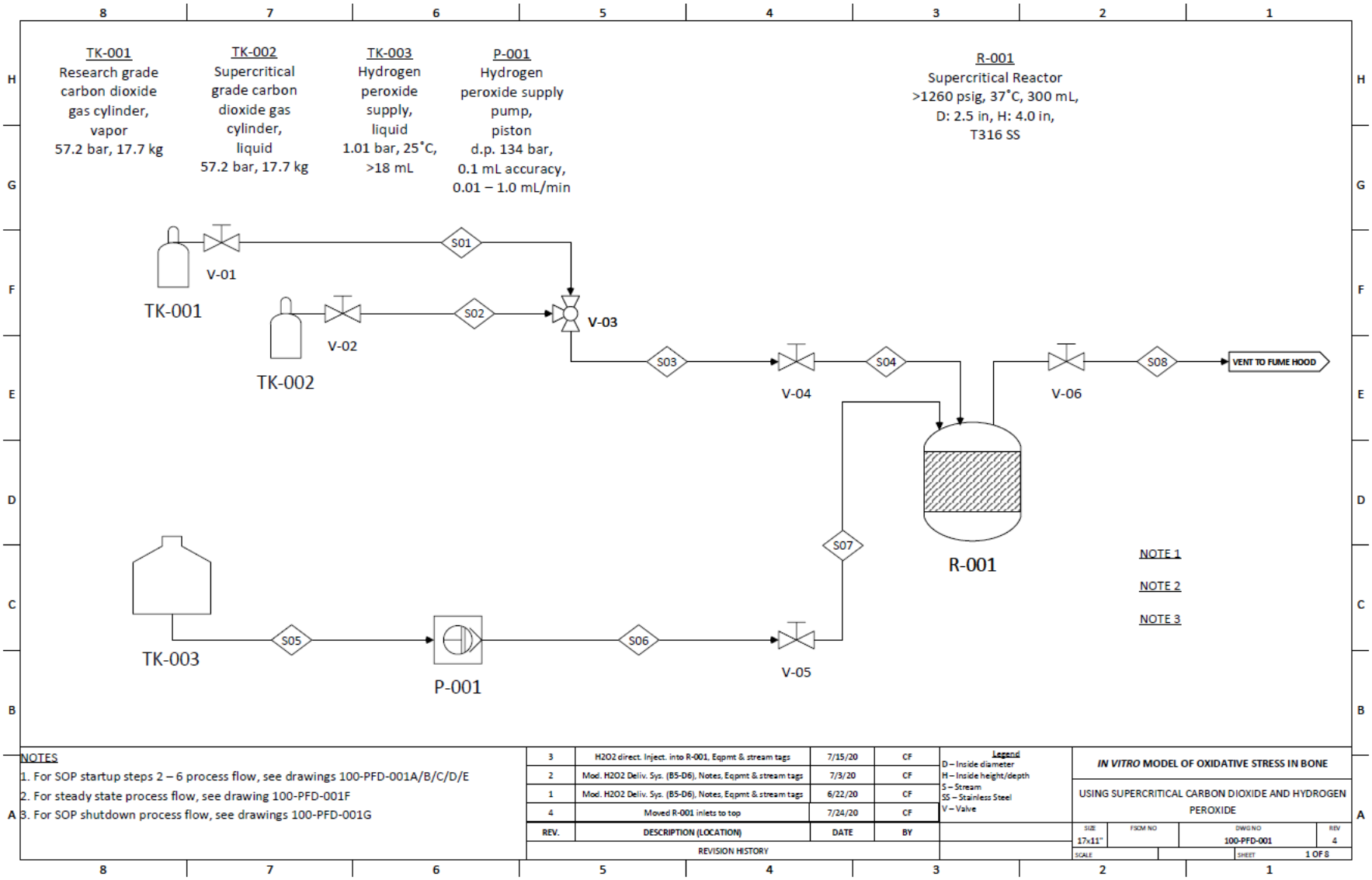
TK-001
Research grade carbon dioxide gas cylinder, vapor
57.2 bar, 17.7 kg
TK-002
Supercritical grade carbon dioxide gas cylinder, liquid
57.2 bar, 17.7 kg
TK-003
Hydrogen peroxide supply, liquid
1.01 bar, 25˚C, >18 mL
P-001
Hydrogen peroxide supply pump, piston
d.p. 134 bar, 0.1 mL accuracy, 0.01 – 1.0 mL/min
R-001
Supercritical Reactor
>1260 psig, 37˚C, 300 mL,
D: 2.5 in, H: 4.0 in,
T316 SS
V-01
V-02
V-03
V-04
V-05
V-06
S01
S02
S03
S04
S05
S06
S07
S08
VENT TO FUME HOOD
NOTE 1
NOTE 2
NOTE 3
NOTES
1. For SOP startup steps 2 – 6 process flow, see drawings 100-PFD-001A/B/C/D/E
2. For steady state process flow, see drawing 100-PFD-001F
3. For SOP shutdown process flow, see drawings 100-PFD-001G
REV. DESCRIPTION (LOCATION) DATE BY
3 H2O2 direct. Inject. into R-001, Eqpmt & stream tags 7/15/20 CF
2 Mod. H2O2 Deliv. Sys. (B5-D6), Notes, Eqpmt & stream tags 7/3/20 CF
1 Mod. H2O2 Deliv. Sys. (B5-D6), Notes, Eqpmt & stream tags 6/22/20 CF
4 Moved R-001 inlets to top 7/24/20 CF
REVISION HISTORY
Legend
D – Inside diameter
H – Inside height/depth
S – Stream
SS – Stainless Steel
V – Valve
IN VITRO MODEL OF OXIDATIVE STRESS IN BONE
USING SUPERCRITICAL CARBON DIOXIDE AND HYDROGEN PEROXIDE
SIZE 17x11"
FSCM NO
DWG NO 100-PFD-001
REV 4
SCALE
SHEET 1 OF 8

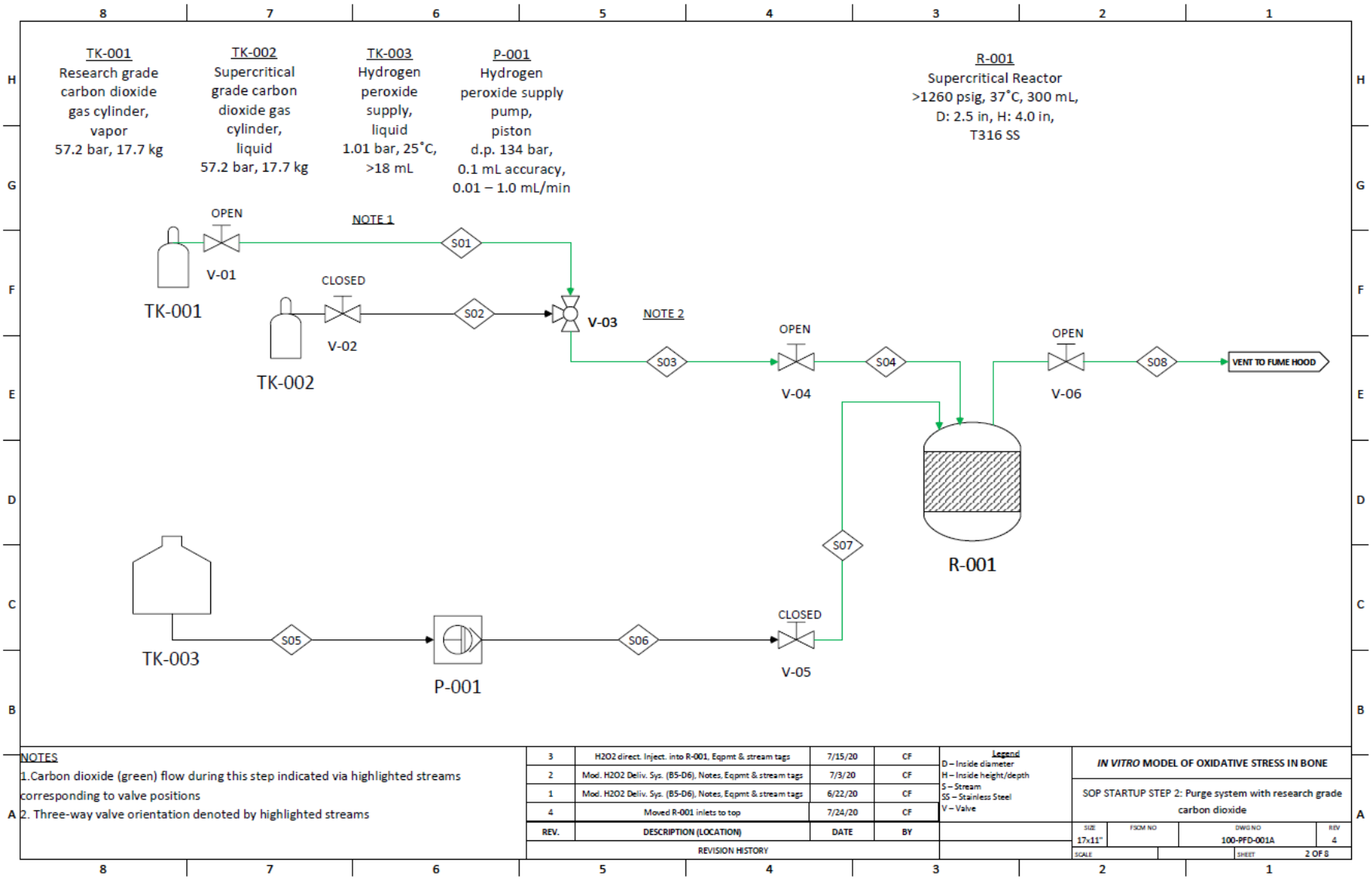

NOTES

1.Carbon dioxide (green) flow during this step indicated via highlighted streams corresponding to valve positions

2. Three-way valve orientation denoted by highlighted streams

REV.	DESCRIPTION (LOCATION)	DATE	BY
3	H2O2 direct. Inject. into R-001, Eqpmt & stream tags	7/15/20	CF
2	Mod. H2O2 Deliv. Sys. (B5-D6), Notes, Eqpmt & stream tags	7/3/20	CF
1	Mod. H2O2 Deliv. Sys. (B5-D6), Notes, Eqpmt & stream tags	6/22/20	CF
4	Moved R-001 inlets to top	7/24/20	CF

REVISION HISTORY

Legend
D – Inside diameter
H – Inside height/depth
S – Stream
SS – Stainless Steel
V – Valve

***IN VITRO* MODEL OF OXIDATIVE STRESS IN BONE**

SOP STARTUP STEP 2: Purge system with research grade carbon dioxide

SIZE	FSCM NO	DWG NO	REV
17x11"		100-PFD-001A	4
SCALE		SHEET	2 OF 8

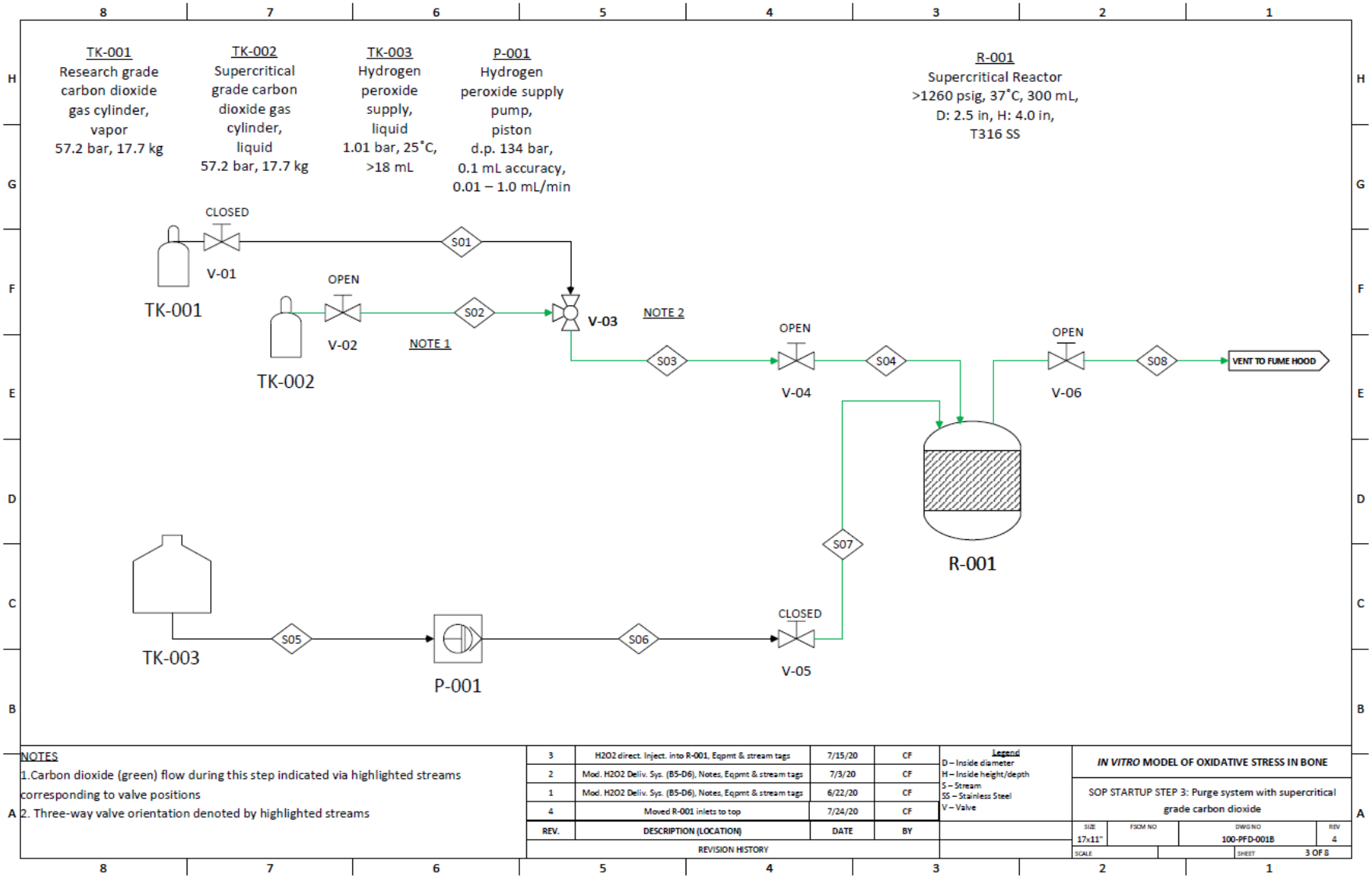

NOTES

1.Carbon dioxide (green) flow during this step indicated via highlighted streams corresponding to valve positions

2. Three-way valve orientation denoted by highlighted streams

REV.	DESCRIPTION (LOCATION)	DATE	BY
3	H2O2 direct. Inject. into R-001, Eqpmt & stream tags	7/15/20	CF
2	Mod. H2O2 Deliv. Sys. (B5-D6), Notes, Eqpmt & stream tags	7/3/20	CF
1	Mod. H2O2 Deliv. Sys. (B5-D6), Notes, Eqpmt & stream tags	6/22/20	CF
4	Moved R-001 inlets to top	7/24/20	CF

REVISION HISTORY

Legend
D – Inside diameter
H – Inside height/depth
S – Stream
SS – Stainless Steel
V – Valve

IN VITRO MODEL OF OXIDATIVE STRESS IN BONE

SOP STARTUP STEP 3: Purge system with supercritical grade carbon dioxide

SIZE	FSCM NO	DWG NO	REV
17x11"		100-PFD-001B	4

SCALE | SHEET 3 OF 8

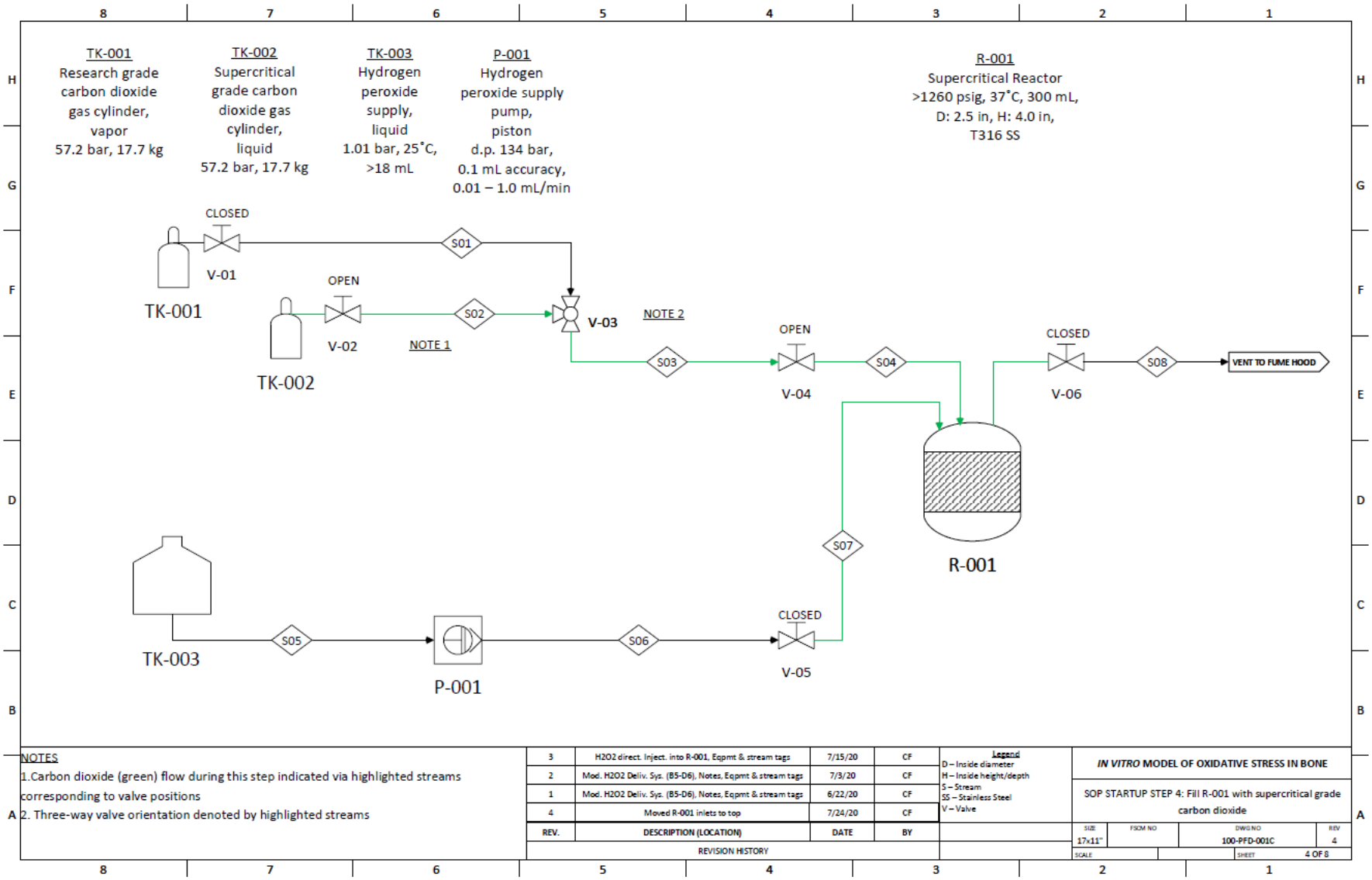

NOTES

1.Carbon dioxide (green) flow during this step indicated via highlighted streams corresponding to valve positions

2. Three-way valve orientation denoted by highlighted streams

REV.	DESCRIPTION (LOCATION)	DATE	BY
3	H_2O_2 direct. Inject. into R-001, Eqpmt & stream tags	7/15/20	CF
2	Mod. H_2O_2 Deliv. Sys. (B5-D6), Notes, Eqpmt & stream tags	7/3/20	CF
1	Mod. H_2O_2 Deliv. Sys. (B5-D6), Notes, Eqpmt & stream tags	6/22/20	CF
4	Moved R-001 inlets to top	7/24/20	CF

REVISION HISTORY

Legend
D – Inside diameter
H – Inside height/depth
S – Stream
SS – Stainless Steel
V – Valve

IN VITRO MODEL OF OXIDATIVE STRESS IN BONE

SOP STARTUP STEP 4: Fill R-001 with supercritical grade carbon dioxide

SIZE	FSCM NO	DWG NO	REV
17x11"		100-PFD-001C	4

SCALE | SHEET 4 OF 8

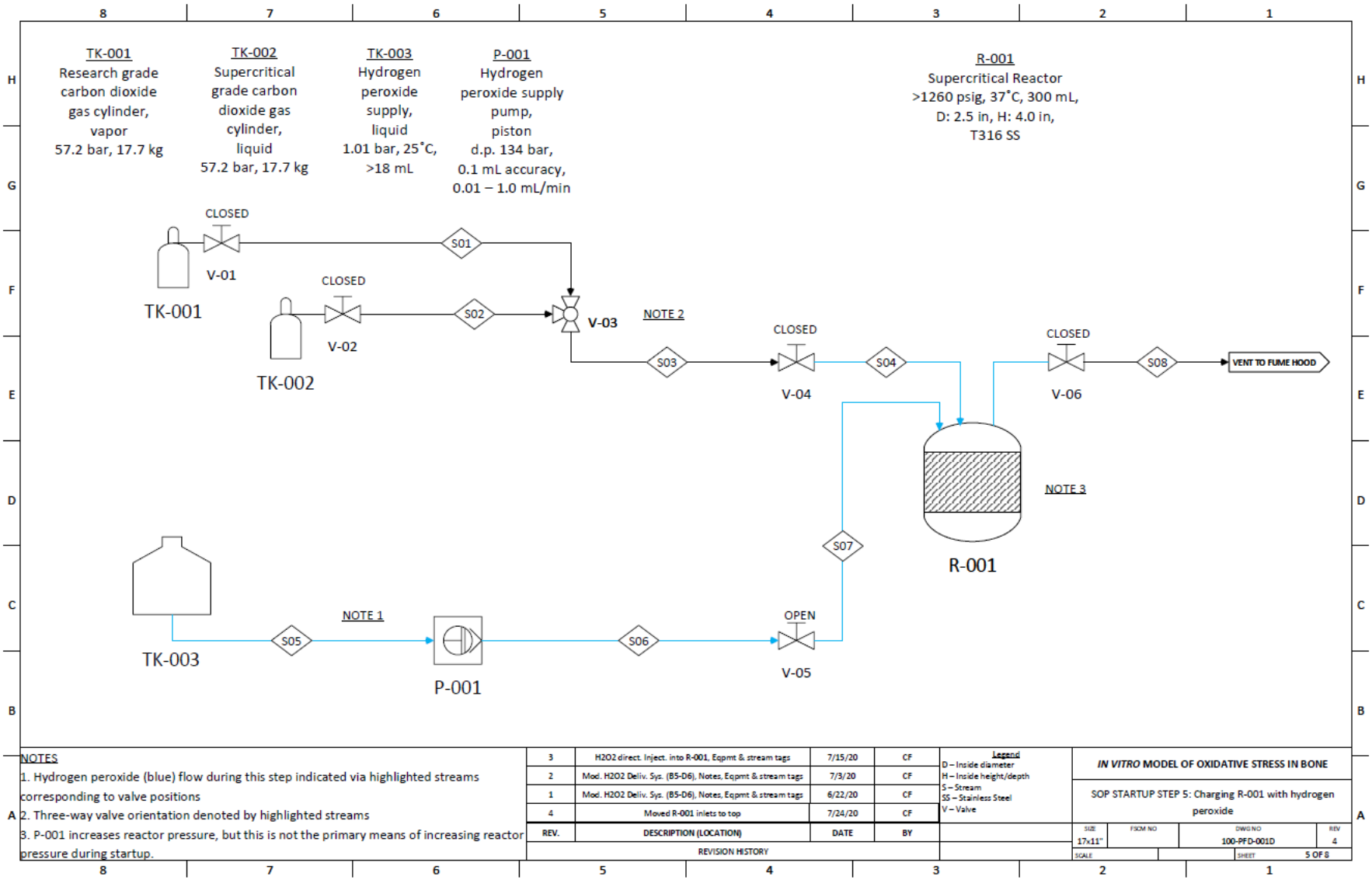

NOTES

1. Hydrogen peroxide (blue) flow during this step indicated via highlighted streams corresponding to valve positions
2. Three-way valve orientation denoted by highlighted streams
3. P-001 increases reactor pressure, but this is not the primary means of increasing reactor pressure during startup.

REV.	DESCRIPTION (LOCATION)	DATE	BY
3	H_2O_2 direct. Inject. into R-001, Eqpmt & stream tags	7/15/20	CF
2	Mod. H_2O_2 Deliv. Sys. (B5-D6), Notes, Eqpmt & stream tags	7/3/20	CF
1	Mod. H_2O_2 Deliv. Sys. (B5-D6), Notes, Eqpmt & stream tags	6/22/20	CF
4	Moved R-001 inlets to top	7/24/20	CF

REVISION HISTORY

Legend
D – Inside diameter
H – Inside height/depth
S – Stream
SS – Stainless Steel
V – Valve

***IN VITRO* MODEL OF OXIDATIVE STRESS IN BONE**

SOP STARTUP STEP 5: Charging R-001 with hydrogen peroxide

SIZE 17x11" | FSCM NO | DWG NO 100-PFD-001D | REV 4

SCALE | SHEET 5 OF 8

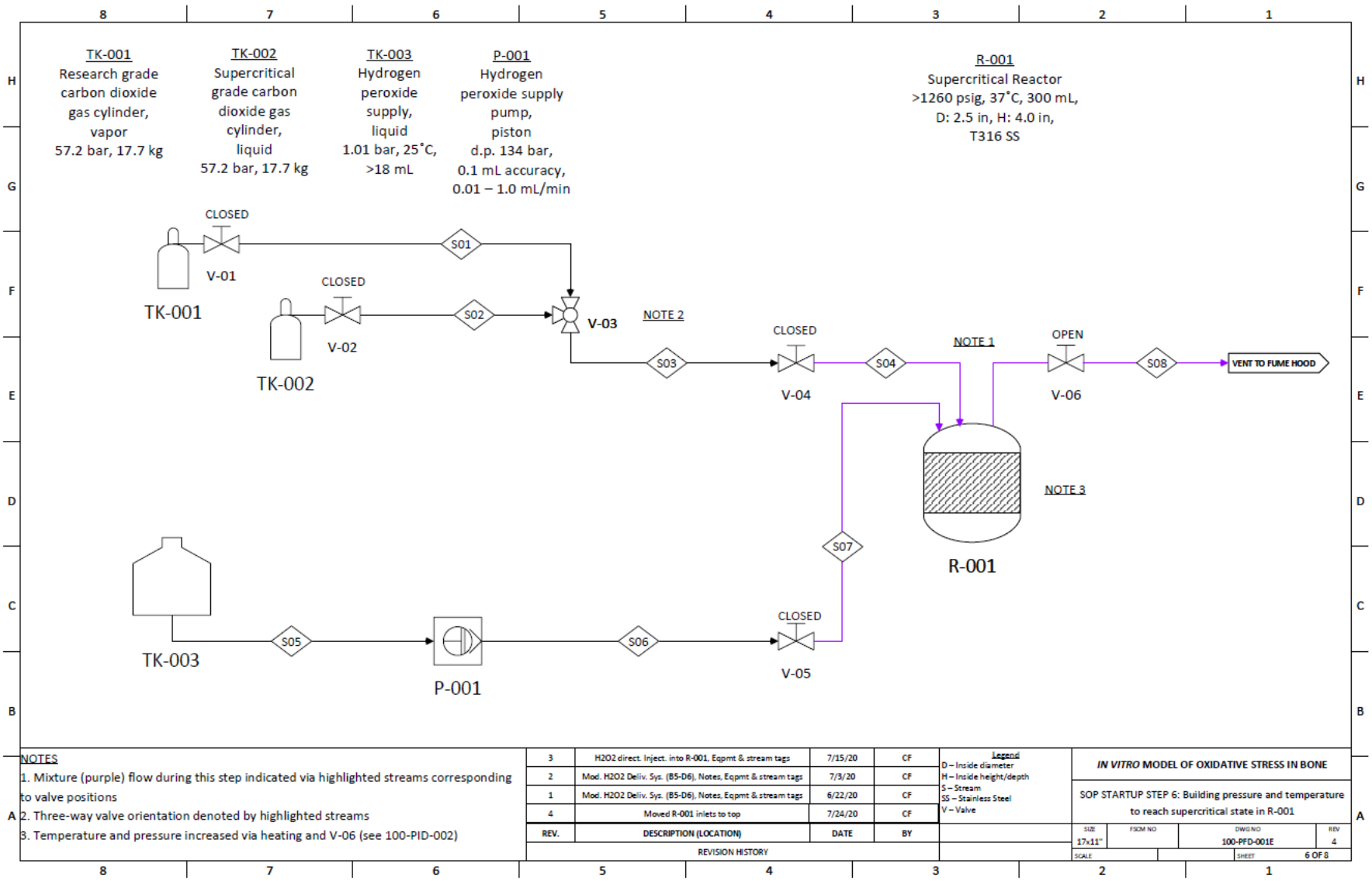

NOTES
1. Mixture (purple) flow during this step indicated via highlighted streams corresponding to valve positions
2. Three-way valve orientation denoted by highlighted streams
3. Temperature and pressure increased via heating and V-06 (see 100-PID-002)

REV.	DESCRIPTION (LOCATION)	DATE	BY
3	H_2O_2 direct. Inject. into R-001, Eqpmt & stream tags	7/15/20	CF
2	Mod. H_2O_2 Deliv. Sys. (B5-D6), Notes, Eqpmt & stream tags	7/3/20	CF
1	Mod. H_2O_2 Deliv. Sys. (B5-D6), Notes, Eqpmt & stream tags	6/22/20	CF
4	Moved R-001 inlets to top	7/24/20	CF

REVISION HISTORY

Legend
D – Inside diameter
H – Inside height/depth
S – Stream
SS – Stainless Steel
V – Valve

IN VITRO MODEL OF OXIDATIVE STRESS IN BONE

SOP STARTUP STEP 6: Building pressure and temperature to reach supercritical state in R-001

SIZE	FSCM NO	DWG NO	REV
17x11"		100-PFD-001E	4

SCALE | SHEET 6 OF 8

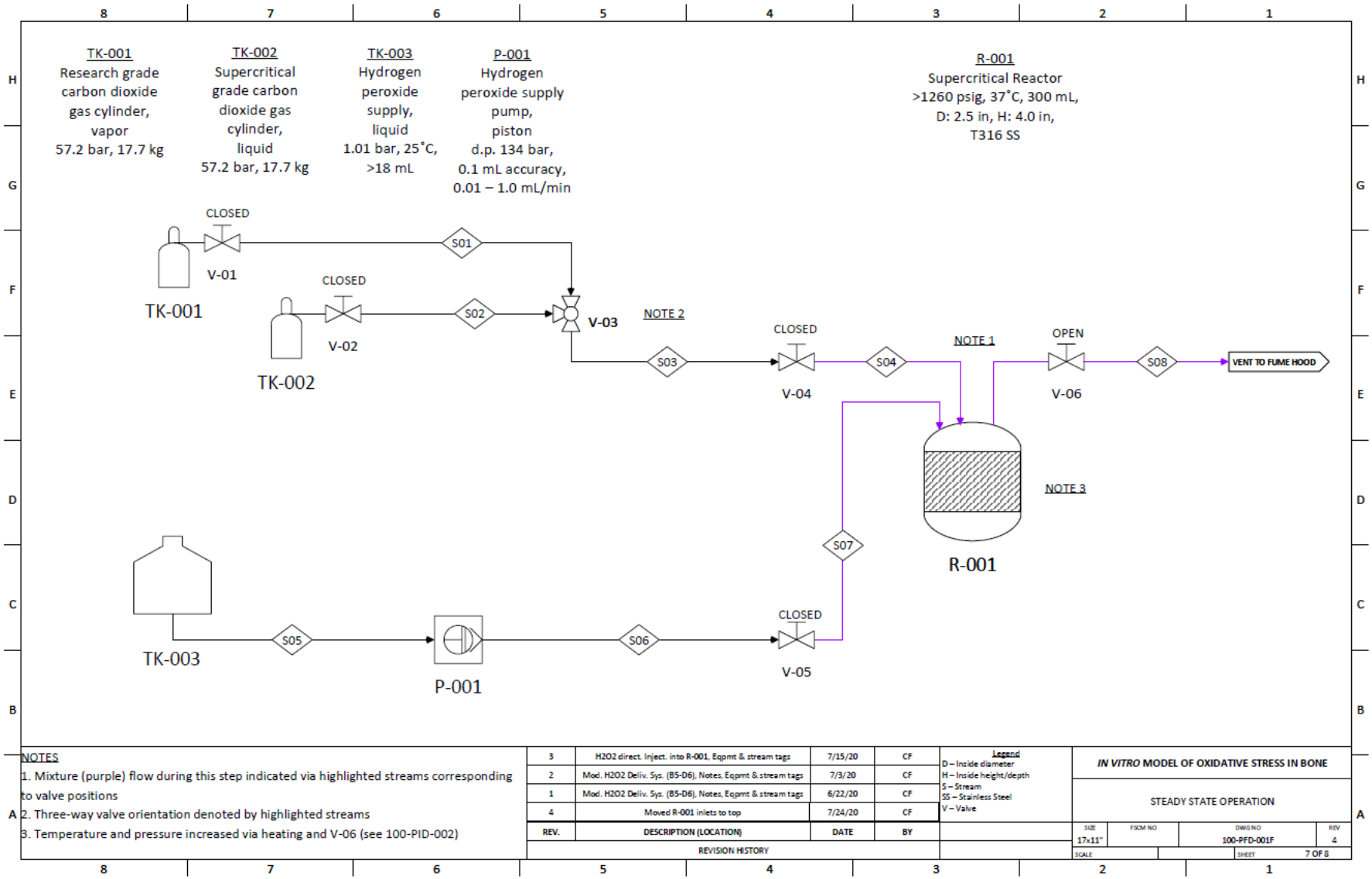

NOTES
1. Mixture (purple) flow during this step indicated via highlighted streams corresponding to valve positions
2. Three-way valve orientation denoted by highlighted streams
3. Temperature and pressure increased via heating and V-06 (see 100-PID-002)

REV.	DESCRIPTION (LOCATION)	DATE	BY
3	H2O2 direct. Inject. into R-001, Eqpmt & stream tags	7/15/20	CF
2	Mod. H2O2 Deliv. Sys. (B5-D6), Notes, Eqpmt & stream tags	7/3/20	CF
1	Mod. H2O2 Deliv. Sys. (B5-D6), Notes, Eqpmt & stream tags	6/22/20	CF
4	Moved R-001 inlets to top	7/24/20	CF

REVISION HISTORY

Legend
D – Inside diameter
H – Inside height/depth
S – Stream
SS – Stainless Steel
V – Valve

IN VITRO MODEL OF OXIDATIVE STRESS IN BONE

STEADY STATE OPERATION

SIZE	FSCM NO	DWG NO	REV
17x11"		100-PFD-001F	4

SCALE | SHEET 7 OF 8

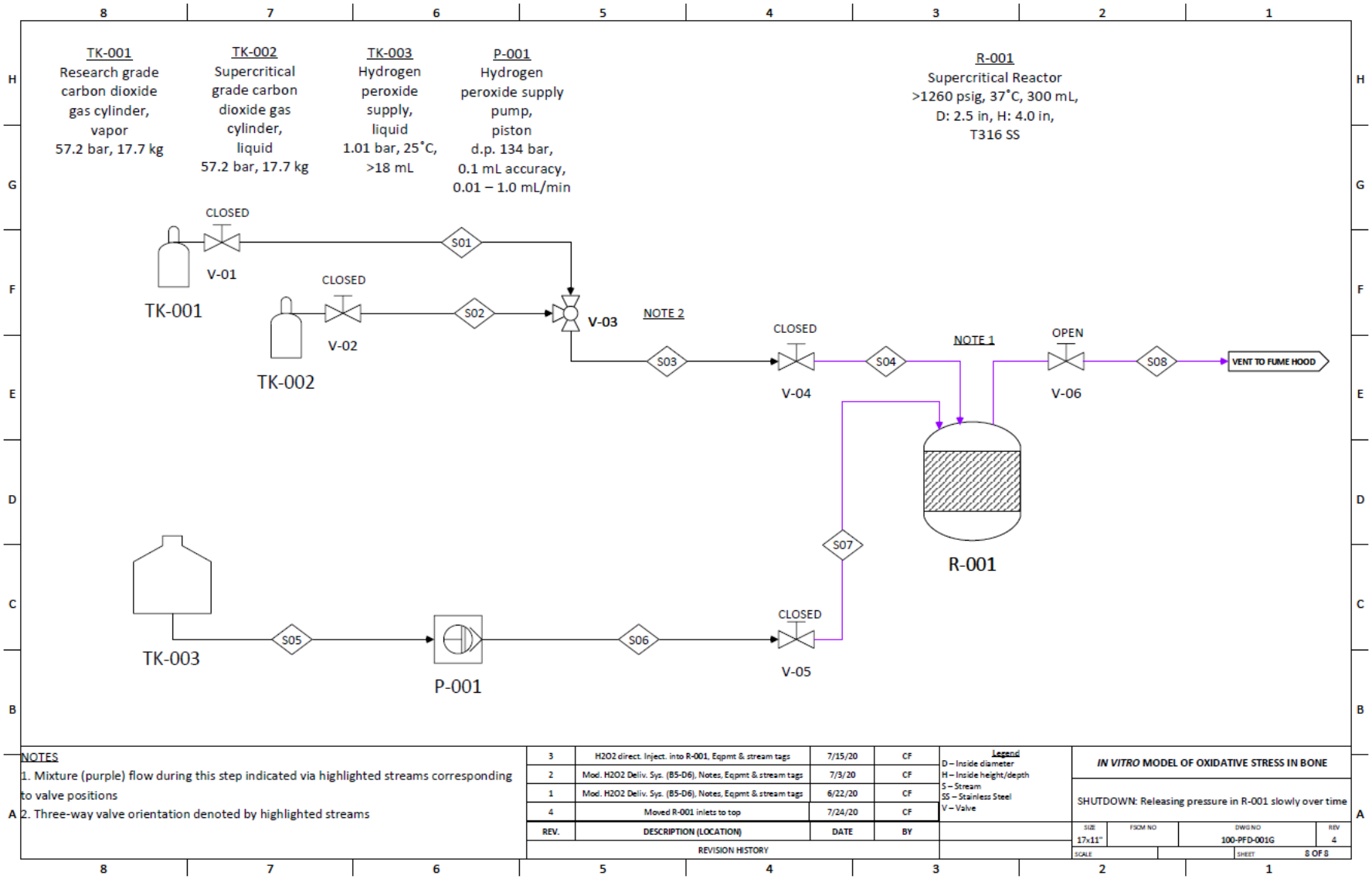

NOTES

1. Mixture (purple) flow during this step indicated via highlighted streams corresponding to valve positions
2. Three-way valve orientation denoted by highlighted streams

REV.	DESCRIPTION (LOCATION)	DATE	BY
3	H_2O_2 direct. Inject. into R-001, Eqpmt & stream tags	7/15/20	CF
2	Mod. H_2O_2 Deliv. Sys. (B5-D6), Notes, Eqpmt & stream tags	7/3/20	CF
1	Mod. H_2O_2 Deliv. Sys. (B5-D6), Notes, Eqpmt & stream tags	6/22/20	CF
4	Moved R-001 inlets to top	7/24/20	CF

REVISION HISTORY

Legend
D – Inside diameter
H – Inside height/depth
S – Stream
SS – Stainless Steel
V – Valve

IN VITRO MODEL OF OXIDATIVE STRESS IN BONE

SHUTDOWN: Releasing pressure in R-001 slowly over time

SIZE	FSCM NO	DWG NO	REV
17x11"		100-PFD-001G	4

SCALE | SHEET 8 OF 8

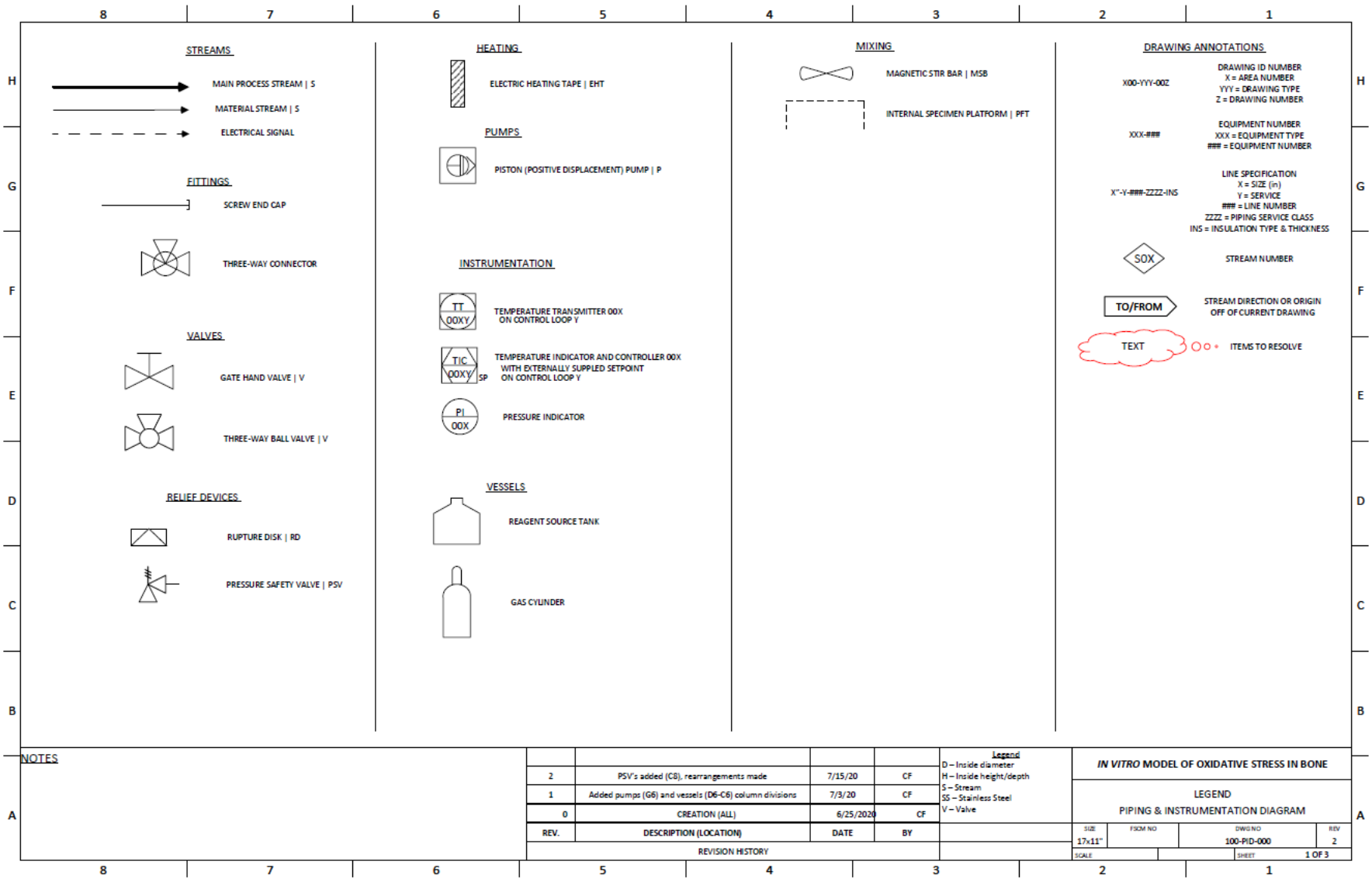
STREAMS
MAIN PROCESS STREAM | S
MATERIAL STREAM | S
ELECTRICAL SIGNAL
FITTINGS
SCREW END CAP
THREE-WAY CONNECTOR
VALVES
GATE HAND VALVE | V
THREE-WAY BALL VALVE | V
RELIEF DEVICES
RUPTURE DISK | RD
PRESSURE SAFETY VALVE | PSV
HEATING
ELECTRIC HEATING TAPE | EHT
PUMPS
PISTON (POSITIVE DISPLACEMENT) PUMP | P
INSTRUMENTATION
TT 00XY
TEMPERATURE TRANSMITTER 00X ON CONTROL LOOP Y
TIC 00XY SP
TEMPERATURE INDICATOR AND CONTROLLER 00X WITH EXTERNALLY SUPPLIED SETPOINT ON CONTROL LOOP Y
PI 00X
PRESSURE INDICATOR
VESSELS
REAGENT SOURCE TANK
GAS CYLINDER
MIXING
MAGNETIC STIR BAR | MSB
INTERNAL SPECIMEN PLATFORM | PFT
DRAWING ANNOTATIONS
X00-YYY-00Z
DRAWING ID NUMBER
X = AREA NUMBER
YYY = DRAWING TYPE
Z = DRAWING NUMBER
XXX-###
EQUIPMENT NUMBER
XXX = EQUIPMENT TYPE
= EQUIPMENT NUMBER
X"-Y-###-ZZZZ-INS
LINE SPECIFICATION
X = SIZE (in)
Y = SERVICE
= LINE NUMBER
ZZZZ = PIPING SERVICE CLASS
INS = INSULATION TYPE & THICKNESS
SOX
STREAM NUMBER
TO/FROM
STREAM DIRECTION OR ORIGIN OFF OF CURRENT DRAWING
TEXT
ITEMS TO RESOLVE
NOTES
REV. | DESCRIPTION (LOCATION) | DATE | BY
2 | PSV's added (C8), rearrangements made | 7/15/20 | CF
1 | Added pumps (G6) and vessels (D6-C6) column divisions | 7/3/20 | CF
0 | CREATION (ALL) | 6/25/2020 | CF
REVISION HISTORY
Legend
D – Inside diameter
H – Inside height/depth
S – Stream
SS – Stainless Steel
V – Valve
IN VITRO MODEL OF OXIDATIVE STRESS IN BONE
LEGEND
PIPING & INSTRUMENTATION DIAGRAM
SIZE 17x11"
FSCM NO
DWG NO 100-PID-000
REV 2
SCALE
SHEET 1 OF 3

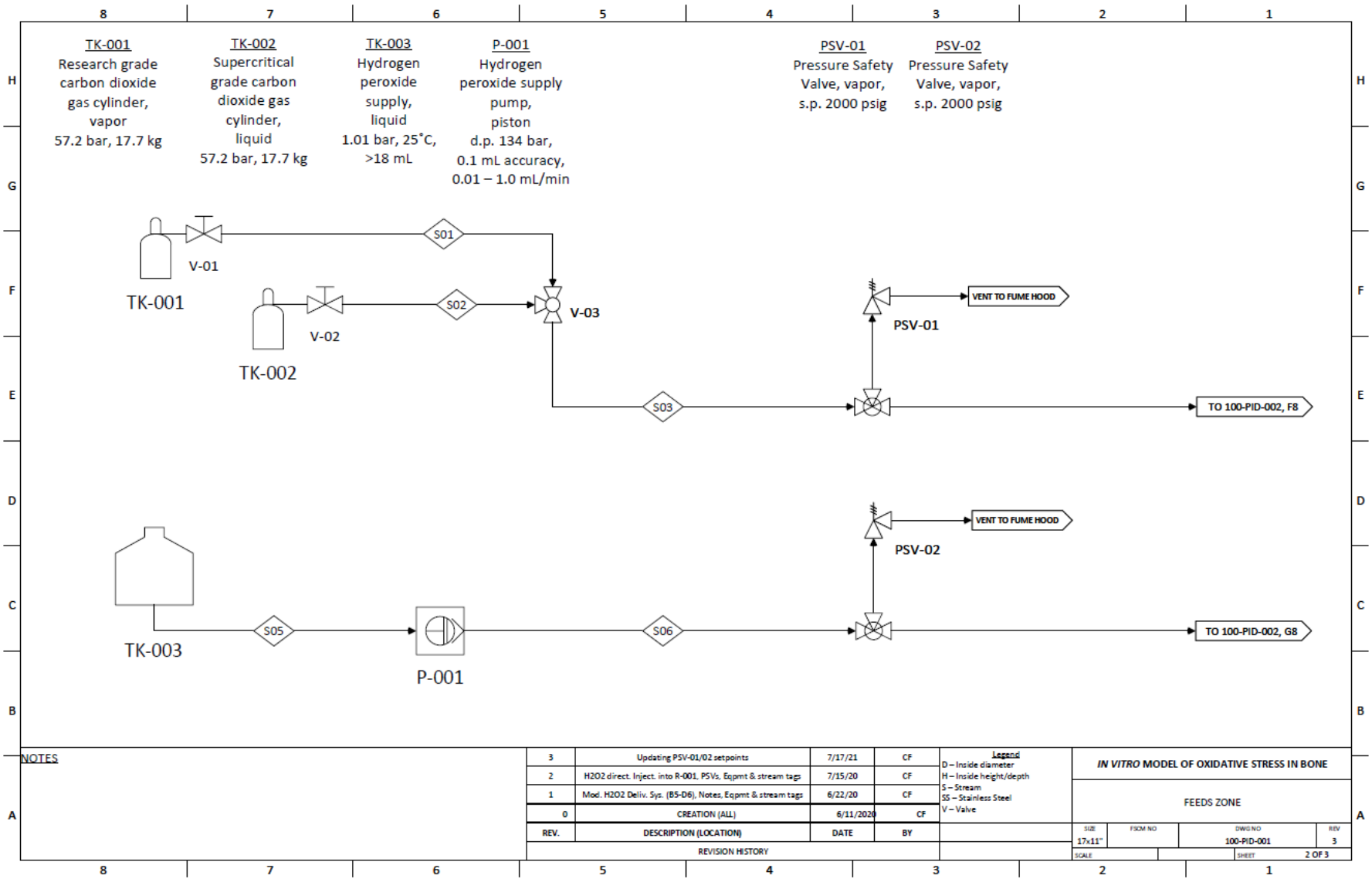
TK-001
Research grade carbon dioxide gas cylinder, vapor
57.2 bar, 17.7 kg
TK-002
Supercritical grade carbon dioxide gas cylinder, liquid
57.2 bar, 17.7 kg
TK-003
Hydrogen peroxide supply, liquid
1.01 bar, 25˚C, >18 mL
P-001
Hydrogen peroxide supply pump, piston
d.p. 134 bar, 0.1 mL accuracy, 0.01 – 1.0 mL/min
PSV-01
Pressure Safety Valve, vapor, s.p. 2000 psig
PSV-02
Pressure Safety Valve, vapor, s.p. 2000 psig
V-01
V-02
V-03
S01
S02
S03
S05
S06
VENT TO FUME HOOD
VENT TO FUME HOOD
TO 100-PID-002, F8
TO 100-PID-002, G8
NOTES
REV. | DESCRIPTION (LOCATION) | DATE | BY
3 | Updating PSV-01/02 setpoints | 7/17/21 | CF
2 | H2O2 direct. Inject. into R-001, PSVs, Eqpmt & stream tags | 7/15/20 | CF
1 | Mod. H2O2 Deliv. Sys. (B5-D6), Notes, Eqpmt & stream tags | 6/22/20 | CF
0 | CREATION (ALL) | 6/11/2020 | CF
REVISION HISTORY
Legend
D – Inside diameter
H – Inside height/depth
S – Stream
SS – Stainless Steel
V – Valve
IN VITRO MODEL OF OXIDATIVE STRESS IN BONE
FEEDS ZONE
SIZE 17x11"
FSCM NO
DWG NO 100-PID-001
REV 3
SCALE
SHEET 2 OF 3

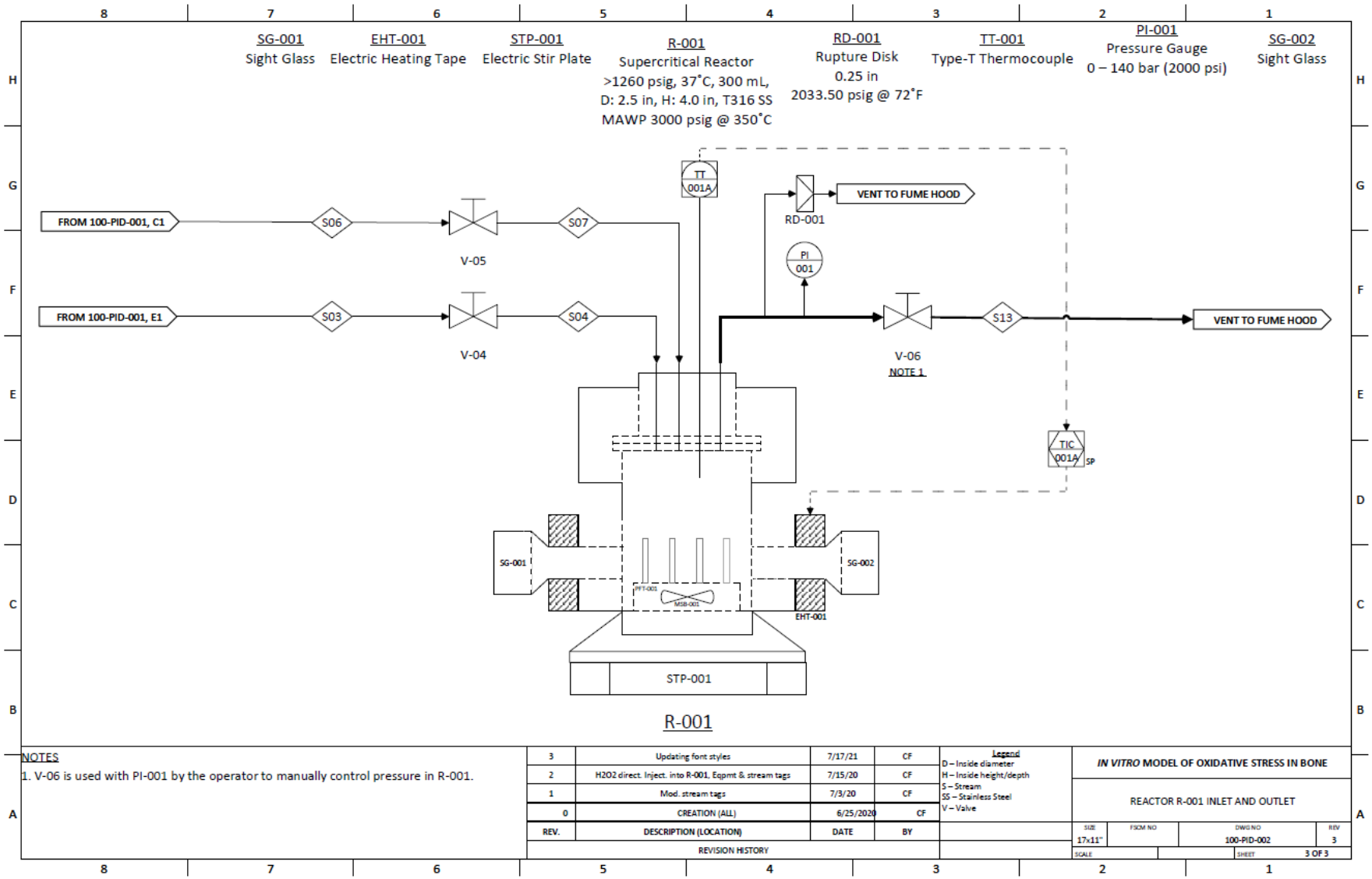

NOTES

1. V-06 is used with PI-001 by the operator to manually control pressure in R-001.

REV.	DESCRIPTION (LOCATION)	DATE	BY
3	Updating font styles	7/17/21	CF
2	H2O2 direct. Inject. into R-001, Eqpmt & stream tags	7/15/20	CF
1	Mod. stream tags	7/3/20	CF
0	CREATION (ALL)	6/25/2020	CF

REVISION HISTORY

Legend
D – Inside diameter
H – Inside height/depth
S – Stream
SS – Stainless Steel
V – Valve

IN VITRO MODEL OF OXIDATIVE STRESS IN BONE

REACTOR R-001 INLET AND OUTLET

SIZE	FSCM NO	DWG NO	REV
17x11"		100-PID-002	3

SCALE | SHEET 3 OF 3

Table 4 – Bill of Materials for the designed in-house supercritical carbon dioxide process.

Equipment Type	Equipment Details	PID Tag	PFD Tag	Specifications	Design Pressure Rating (KPa)	Design Temperature Rating (degC)	Purchase Required?	Quantity	Selected Equipment	Manufacturer	Vendor	Unit Price (CAD)	Cost (CAD, 2021)
Compressed gas cylinder	Research grade CO2, purity = 99.998%, cylinder = K	TK-001	TK-001	Part: CD 4.8RS; Cylinder: K, AS; O2: 2; N2: 10; H2O: 3; CO: 0.5; Halocarbons (as CCl4): -; THC (as CH4): 4; THC (C7-C26) (as Dodecane): -; H2: -; Cylinder specs: K: style: high pressure steel, size in (cm): 51 x 9 (129.5 x 22.9), connection CGA/DISS: 320/716, volume lb (kg): 60 (27.2), gross weight lb (kg): 193 (88)	830 psig (57.2 bar)	N/A	Yes	1	CD 4.8RS-K	Praxair	Praxair	$260.97	$260.97
Compressed gas cylinder	Supercritical grade CO2, purity = 99.999%, cylinder = AS	TK-002	TK-002	Part: CD 5.0SE; Cylinder: AS; O2: 2; N2: 5; H2O: 0.5; CO2: 0.1; Halocarbons (as CCl4): 100 ppb; THC (as CH4): 2, THC (C7-C26) (as Dodecane): 10 ppb; H2: 0.1; Cylinder Specs: AS, Style: aluminum high pressure, size in (cm): 48 x 8 (121.9 x 20.3), connection CGA/DISS: 320/716, Volume lb (kg): 39 (17.7), Gross weight lb (kg): 89 (40), headspace pressure high enough for liquid flow, however advised to use booster pump	830 psig (57.2 bar)	N/A	Yes	1	CD 5.0SE-AS	Praxair	Praxair	$888.59	$888.59
Liquid holding vessel	H2O2 feed vessel to P-001	TK-003	TK-003	Glass container with a volume of at least 500 mL, stopper	0 psig	25 degC	No	1	N/A	N/A	N/A	$0.00	$0.00
High pressure pump	HPLC piston pump for use with hydrogen peroxide	P-001	P-001	Discharge pressure 134 bar, 0.1 mL accuracy, 0.010 - 1.0 mL/min	2000 psig	100 degC	No	1	N/A	N/A	N/A	$0.00	$0.00

Valve	TK-001 outlet. Brass gas cylinder regulator, CO2 service	V-01	V-01	Tank regulator. Tank can be shutoff via the tank valve. Regulator controls delivery pressure. CGA 320 connection.	4000 psig	-40, 60 degC	No	1	N/A	Linde Union Carbide	N/A	$0.00	$0.00
Valve	TK-002 outlet. Brass gas cylinder regulator, CO2 service	V-02	V-02	Tank regulator. Tank can be shutoff via the tank valve. Regulator controls delivery pressure. CGA 320 connection.	3000 psig	-40, 60 degC	No	0	PRS1009751232 0	Prostar	Praxair	$473.13	$0.00
Three-way valve	Three-way valve, stainless steel ball, CO2 service, avoid elastomeric seal components (ie. Viton), include Swagelok fittings	V-03	V-03	SS 1-Piece 40 Series 3-Way Ball Valve 0.15 Cv 1/8 in. Swagelok Tube Fitting	2500 psig @ 100°F /172 bar @ 37°C	-53 degC	Yes	1	SS-41GXS2	Swagelok	Swagelok	$126.89	$126.89
Pressure safety release valve	CO2 reactor inlet stream, Swagelok fittings	PSV-01	-	SS High-Pressure Proportional Relief Valve 1/4 in outlet. Swagelok Tube Fitting Neoprene O-rings Special Order Item Non Returnable or Cancellable after order placed	See relief valve springs	-23 deg C	Yes	1	SS-4R3A-NE	Swagelok	Swagelok	$285.58	$285.58
Pressure safety release valve	H2O2 reactor inlet stream, Swagelok fittings	PSV-02	-	"SS High-Pressure Proportional Relief Valve,1/4 in outlet. Swagelok Tube Fitting, PTFE O-rings. This relief valve does NOT come with a spring installed,,spring sold separately." Special Order Item Non Returnable or Cancellable after order placed	6000 psig @ 100°F /413 bar @ 37°C	-268, 327 degC	Yes	1	SS-4R3A	Swagelok	Swagelok	$212.70	$212.70
Relief valve springs	Springs for relief valves to give them their set pressure	For PSV-01 /02	-	Purple Spring Kit for R3A Series Proportional Relief Valves 750 to 1500 psig (51.7 to 103 bar) Special Order Item Non Returnable or Cancellable after order placed	750 - 1500 psig	N/A	Yes	2	177-R3A-K1-C	Swagelok	Swagelok	$9.05	$18.10

T-connector	Connect PSV-01/02 to 1/8" tubing	-	-	SS Swagelok Tube Fitting Union Tee 1/8 in. (all three ports) Tube OD	8,500 psig (586 bar)	Up to 537 degC but pressure rating reduces beyond 93 degC	Yes	2	SS-200-3	Swagelok	Swagelok	$33.19	$66.38
Reducer port connector	to connect PSV-01/02 (1/4 in.) to T-connectors (1/8 in.)	-	-	SS Swagelok Tube Fitting Reducing Port Connector 1/4 in. x 1/8 in. Tube OD Special Order Item Non Returnable or Cancellable after order placed	8,500 psig (586 bar)	Up to 537 degC but pressure rating reduces beyond 93 degC	Yes	2	SS-401-PC-2	Swagelok	Swagelok	$17.36	$34.72
Tubing	regular service, stainless steel,, OD = 1/8 in, thickness = 0.028 in clean w/o mill oil	-	-	L = 40 ft total (2x 20 ft bundles), 316L stainless steel	8,500 psig (586 bar)	Up to 537 degC but pressure rating reduces beyond 93 degC	Yes	40	SS-T2-S-028-20	Swagelok	Swagelok	$6.70	$268.00
Tubing (R-001 outlet)	Vents (reactor outlet, PSV outlets, RD outlet), stainless steel, OD = 1/4 in, thickness = 0.035 in, clean w/o mill oil	-	-	L = 20 ft total, 316L stainless steel	5,100 psig (351 bar)	Up to 537 degC but pressure rating reduces beyond 93 degC	Yes	20	SS-T4-S-035-20	Swagelok	Swagelok	$3.70	$74.00
Backpressure regulator	Backpressure regulator valve on R-001 outlet, stainless steel	???	-	KPB Series Medium- to High-Pressure Piston-Sensing Back-Pressure Regulator 316 SS body material 0 to 2000 psig (0 to 137 bar) pressure control range 1/4 in. female NPT ports (inlet, outlet - 2 ports total) PEEK seat and seal material 0.06 Cv 316 SS piston sensing mechanism Green knob handle	0 - 2000 psig control range	Check PEEK seat in catalog	Yes	1	KPB1N0A422P20000	Swagelok	Swagelok	$760.61	$760.61

Reactor	SCCO2 high pressure reactor	R-001	R-001	Supercritical reactor, diameter: 2.5 in., height 4.0 in., T316 Stainless steel, MAWP 3000 PSI @ 350 degC	MAWP 3000 psig	350 degC	No	1 N/A	Parr Instruments	Parr Instruments	$0.00	$0.00
Valve	Stainless steel needle or globe, H2O2, CO2 service, avoid elastomeric seal components (ie. Viton), include Swagelok fittings, R-001 CO2 inlet valve	V-04	V-04	PFA packing, SS Integral Bonnet Needle Valve 0.09 Cv 1/8 in. Swagelok Tube Fitting Regulating Stem	5000 psi @ 37 degC	-53 degC	Yes	1 SS-ORS2	Swagelok	Swagelok	$100.46	$100.46
Valve	Stainless steel needle or globe, H2O2, CO2 service, avoid elastomeric seal components (ie. Viton), include Swagelok fittings, R-001 CO2 inlet valve	V-05	V-05	PFA packing, SS Integral Bonnet Needle Valve 0.09 Cv 1/8 in. Swagelok Tube Fitting Regulating Stem	5000 psi @ 37 degC	-53 degC	Yes	1 SS-ORS2	Swagelok	Swagelok	$100.46	$100.46
Valve	Stainless steel needle or globe, H2O2, CO2 service, avoid elastomeric seal components (ie. Viton), include Swagelok fittings, R-001 outlet vent valve	V-06	V-06	Stainless steel, valve already installed on R-001 outlet, 1/4 in. inlet and outlet. Swagelok valve included in bill of materials as backup	5000 psi @ 37 degC	-53 degC	No	0 SS-1RS4	Swagelok	Swagelok	$93.84	$0.00
Pressure gauge	R-001 pressure gauge	PI-001	-	0 - 140 bar	140 bar	N/A	No	1 Duralife	Ashcroft	N/A	$0.00	$0.00
Rupture disk	R-001 rupture disk	RD-001	-	0.25 in. diameter, type: P ST FS, material: INC	2033.50 psig @ 72 degF	N/A	No	1	Fike Metal Products	N/A	$0.00	$0.00

Magnetic stir bar	In R-001 to ensure supercritical mixture is well mixed	MSB-001	-	1 in. length, 3/8 in. diameter, magnetic	N/A	N/A	No	1	RK-04770-40	Mono-Mold	Cole-Parmer	$0.00	$0.00
Specimen holder	Must hold specimens (4x4x50 mm^3) suspended in supercritical mixture	PFT-001	-	NovaPouch3x5, NovaSterilis process pouches 3"x5", set of 100 pouches	N/A	N/A	Yes	1	NovaPouch3x5	NovaSterilis	NovaSterilis	$90.00	$90.00
Sight Glass	Mounted on R-001	SG-001/2	-	Quartz crystal, MAWP 3000 PSI @ 350 degC	MAWP 3000 psig	350 degC	No	2	N/A	Parr Instruments	Parr Instruments	$0.00	$0.00
Fitting	1/8" NPTM for R-001 inlet (see labelled photo)	-	-	Stainless Steel Swagelok Tube Fitting, Male Connector, 1/8 in. Tube OD x 1/8 in. Male NPT	8,500 psig (586 bar)	Up to 537 degC but pressure rating reduces beyond 93 degC	Yes	1	SS-200-1-2	Swagelok	Swagelok	$10.24	$10.24
Fitting	Gas cylinder connection - 1/4 in.	-	-	SS Swagelok Tube Fitting Male Connector 1/8 in. Tube OD x 1/4 in. Male NPT	8,500 psig (586 bar)	Up to 537 degC but pressure rating reduces beyond 93 degC	Yes	2	SS-200-1-4	Swagelok	Swagelok	$11.41	$22.82
Fitting	Elbow for clearance on R-001 inlet	-	-	Stainless Steel Swagelok Tube Fitting, Male Elbow, 1/8 in. Tube OD x 1/8 in. Male NPT	8,500 psig (586 bar)	Up to 537 degC but pressure rating reduces beyond 93 degC	Yes	2	SS-200-2-2	Swagelok	Swagelok	$16.50	$33.00
Fitting	Parr to Swagelok connector	-	-	Parr fitting req'd with adapter end (ie. 1/8" NPTF or 1/8" Swagelok) on R-001 inlet	8,500 psig (586 bar)	537 degC	No	1	N/A	Parr Instruments	Parr Instruments	$0.00	$0.00

Fitting	R-001 outlet replace 1/4" NPTF fitting	-	-	Stainless Steel Swagelok Tube Fitting, Female Connector, 1/4 in. Tube OD x 1/4 in. Female NPT	8,500 psig (586 bar)	Up to 537 degC but pressure rating reduces beyond 93 degC	Yes	1	SS-400-7-4	Swagelok	Swagelok	$15.81	$15.81
Fitting	PTFE Sealing tape for Swagelok fitting threads	-	-	Swagelok terms and conditions require that PTFE sealing tape is used. PTFE is compatible with CO2 and H2O2 (30%)	N/A	N/A	No	1	N/A	N/A	N/A	$0.00	$0.00

Grand Total (CAD)
$5,556.55